Spatial constraints and the organization of the cytoskeleton

Ioana Cristina Gârlea

Thesis committee

Promotor
Prof. Dr Bela M. Mulder
Professor of Theoretical Cell Physics
Wageningen University
Group leader Theory of Biomolecular Matter
FOM Institute AMOLF, Amsterdam

Other members
Prof. Dr Jasper van der Gucht, Wageningen University
Prof. Dr René van Roij, Utrecht University
Dr François Nédélec, EMBL Heidelberg, Germany
Prof. Dr Paul P.A.M. van der Schoot, University of Technology, Eindhoven

This research was conducted under the auspices of the Graduate School of Experimental Plant Sciences.

Spatial constraints and the organization of the cytoskeleton

Ioana Cristina Gârlea

Thesis
submitted in fulfilment of the requirements for the degree of doctor
at Wageningen University
by the authority of the Rector Magnificus
Prof. Dr M.J. Kropff,
in the presence of the
Thesis Committee appointed by the Academic Board
to be defended in public
on Friday 16 January 2015
at 11 a.m. in the Aula.

Ioana Cristina Gârlea
Spatial constraints and the organization of the cytoskeleton
184 pages.

PhD thesis, Wageningen University, Wageningen, NL (2015)
With references, with summaries in Dutch and English

ISBN: 978-94-6257-212-6

To my parents

Contents

1

Introduction

In this chapter we introduce the cytoskeleton and present its role in the cell, as well as its interactions with other cell components. We discuss the advantage of using bio-mimetic systems as simplified experimental models for the cell. Inspired by these systems we also show how other bio-materials, such as viruses, can be used to reproduce patterns created by the cytoskeleton leading to new applications. Finally we give an overview of the models and techniques that will be used in this thesis.

1.1 The cytoskeleton in living cells

Cells contain a network of filamentous polymers localized in the cytoplasm, called the cytoskeleton [1]. This network plays a crucial role in in the cell as it acts as a scaffold, giving the cell mechanical support, and acts as tracks for transport of components throughout the cell [2, 3]. The shape of the cell is controlled by reorganization of the cytoskeletal filaments, enabling the cell, for example, to migrate [4]. The cytoskeleton is also a key player in cell division, where both the separation of the genetic material and the separation of the mother cell into daughter cells depend on these filaments.

The structure of the cytoskeleton may differ between various organisms. In plant and animal cells and, in general, in all cells with a membrane-bound nucleus, called eukaryots, we find three distinct classes of cytoskeletal filaments, namely, actin filaments, microtubules, and intermediate filaments. Prokaryotic cells such as bacteria have homologues of these filaments that perform similar functions to the their eukaryotic counterparts [5].

1.1.1 Components of the cytoskeleton

The classification of cytoskeletal polymers in eukaryotes is based on the mechanical properties and structure of these filaments. One of the relevant quantities to characterize the mechanical properties of these filaments is the persistence length l_p. This characterizes how stiff a polymer is. More formally it is defined as the length L over which the tangent-tangent correlations decay exponentially due to thermal fluctuations [6]. mathematically this can be expressed as:

$$\langle \hat{\mathbf{t}}(L) \cdot \hat{\mathbf{t}}(0) \rangle = e^{-L/l_p}, \tag{1.1}$$

where $\hat{\mathbf{t}}$ is the unit vector tangent to the polymer chain. The persistence length is proportional to the bending stiffness κ_B, the proportionality factor being k_BT ($\kappa_B = k_BTl_p$) where k_B is the Boltzmann constant and T the temperature [7]. At a more intuitive level a polymer that is shorter than its persistence length will behave as a rigid rod. If it is much longer than the persistence length, it will be fully elastic. In the intermediate regime, when the two lengths are comparable, the behavior of the polymer is best described by an elastic rod.

Microtubules are the stiffest of the cytoskeletal polymers. Their persistence length is of the order of millimeters [8] and has been observed to increase with the length of the microtubule [9]. Considering that a typical animal cell diameter is in the order of 10s of microns, the microtubules are often only several microns long. At this length scale microtubules behave as rigid rods.

The basic structural units of microtubules are two globular proteins from the tubulin family: $\alpha-$ and $\beta-$ tubulin [10], which assemble to form dimers. These dimers are organized longitudinally in straight protofilaments. A number of 13 protofilaments are arranged side by side creating the hollow tube-like structure of the microtubules (see figure 1.1 (b)). The outer diameter of this structure is $\sim 25\ nm$. The polymerization of microtubules is a highly dynamical process: after an initial nucleation phase, tubulin dimers are rapidly added to one of the ends, called the plus end, of the microtubule [11, 12]. Fast depolymerization also happens at the same end, phases of grow and shrinkage alternating in time. It is possible to prevent the depolymerization by using drugs such as taxol that stabilize the structure of microtubules [13].

Actin filaments, also called F-actin, are much more flexible than microtubules, having a persistence length of $\sim 17\mu m$ [14]. They are also thinner than microtubules, with a diameter of $\sim 8\ nm$ [15]. Actin filaments are constituted of a protein called globular actin (or G-actin) that assembles in a double helical structure (see figure 1.1 (a)). The polymerization of actin filaments happens at one its ends (called the barbed end) and the depolymerization at the other one (the pointed end). The polymerization and depolymerization rates depend on the concentration of G-actin around the filament. There is a regime in which these two rates become equal, the number of monomers added being the same as the number of monomers that disassemble from the filament, resulting in a constant filament length. This steady state regime is called treadmilling [16].

Intermediate filaments are a diverse class of cytoskeletal filaments [17]. Examples include nuclear lamins, that are responsible for regulating the shape of the nucleus, or keratins, which are found in epithelial cells, nails or hair and have the role preventing the cell from deforming under mechanical stress. Intermediate filaments typically have a rope-like structure. As their

name implies, they have mechanical properties which are are in between the ones of the other two classes of cytoskeletal polymers [18]. They are stiffer than actin filaments but less rigid than microtubules. In this work will focus on the organization of microtubules and actin filaments. However, the models that we develop are general and thus could in principle also apply to to intermediate filaments.

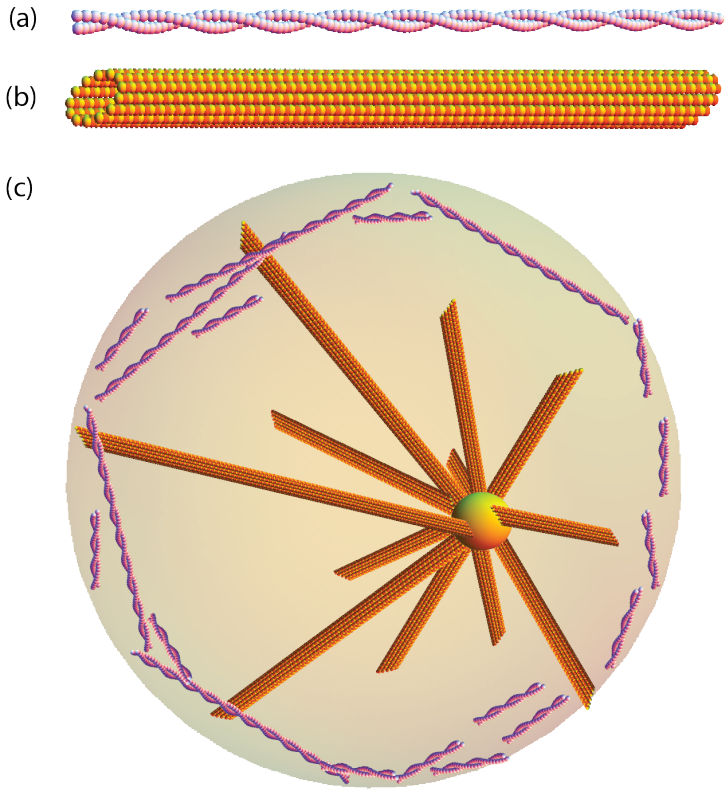

Figure 1.1: Schematic representation of actin filaments and microtubules: (a)structure of actin filaments- globular actin is represented by purple sphere, (b) structure of microtubules- $\alpha-$ and $\beta-$ dimers shown as yellow and orange spheres, (c) typical organization of these cytoskeletal polymers in animal cells: actin filaments located in the cortical region and microtubules aster with the centrosome at the core.

1.1.2 Functions of the cytoskeleton

In animal cells, the cytoskeleton fulfills many tasks. One of its main roles is to control the shape of the cell [19]. The actin cortex, which is a network of crosslinked actin filaments that are also attached to the membrane, makes the cell harder to deform under external stress. In blood platelets, both microtubules and actin form a ring in the equatorial zone of this discoidal cell fragment [20]. By disassembling the microtubule ring the platelet looses its discoidal shape becoming spherical [21]. Actin and microtubules are also very important in cell division. The segregation of the chromosomes is performed by a structure called a spindle that consist of two microtubule asters. These asters position themselves at opposite poles of the mother cell, capture the duplicated chromosomes and pull them apart, and transport them to their end of the cell [22]. When this process is finished a ring of actin filaments and myosin motors is assembled in the division plane [23]. This acto-myosin ring contracts and separates the cell in two. Actin is also key player in migration. The way cells such as fibroblasts move is by creating a lamlipodium in which actin filaments are polymerized against the membrane pushing it forward [24]. Pulling against the substratum on which they migrate is insured by transmembrane proteins connected to actin stress fibers. Both actin and microtubules are used as tracks to transport vesicles throughout the cell. This is achieved by motor proteins bound on the vesicle that move on the cytoskeletal polymers.

1.1.3 Interactions that shape the cytoskeleton

Both actin filaments and microtubules grow in the cytosol, which is the gel-like component of the cytoplasm, which is the whole content of the cell enclosed by the cellular envelope, except for the nucleus. However they are not the only cellular components that are present there, the cytoplasm being a rather crowded environment. The nucleus, or the vacuole in the case of plant cells, takes up a considerable amount of space of the cytoplasm, the cytosol filling only the space left by the other cell components. Actin filaments and microtubules are forced to grow around these components. Also, the density of cytoskeletal polymers in the cytosol can be quite high and they have to find a way of packing themselves efficiently, often inducing mutual alignment. As a result, the cytoskeleton permanently competes for space inside the cell. In addition to this, the cytoskeletal polymers are sub-

ject to confinement of the cell envelope. The cell envelope creates a physical barrier between the cytoplasm and the exterior of the cell, constraining the cytoskeleton to organize on the inside. As they grow, actin filaments and microtubules are often pushing against the envelope and are pushed by each other and by the other components against it. Therefore, confinement is a key factor that shapes the organization of the cytoskeleton.

The typical organization of the cytoskeleton is different between plant and animal cells. In plants the center of the cell is mostly filled with vacuoles, the cytosol being localized mainly in the cortical region, just beneath the cell wall. The wall is made out of cellulose and is too rigid to be deformed by the forces created in the cell. Both actin filaments and microtubules find themselves confined in this almost two dimensional region between the vacuoles and the wall [25]. Microtubules, which are much stiffer than actin filaments, are forced to follow the wall since they are physically connected to it through protein linkers [26]. The density of microtubules in this area is high therefore they align to each other. In animal cells the cytosol is more evenly distributed in the cell volume. Microtubules typically grow outwards from an organizing center called the centrosome located in center of the cell, close to the nucleus. The centrosome is a ball of proteins which is a few 100 nm in diameter. The microtubules grow radially from the centrosome towards the periphery of the cell, creating an aster (see figure 1.1 (c)). This aster is subject to confinement since the tips of the microtubules reach the cell membrane and push against it [27]. Unlike in the case of plants, animal cells have a flexible membrane that separates the cell volume from the extracellular matrix, microtubules can deform the membrane. However this membrane is under tension and will exert a force on the microtubules growing against it. This can bend the microtubules or limit the length that they can have by affecting their growth since, when a microtubule is growing against a physical barrier, rapid shrinkage occurs more often than in the bulk [28]. Actin filaments are found throughout the animal cell, but are more dense in the cortical region. There are regions in which these filaments are densely packed such as lamelipodia or filopodia. Lamelipodia are sheetlike membrane protrusion that the cell creates in order to move. Inside these protrusions actin confined in an almost flat space [29, 30, 31]. Filopodia are needle-like structures at the tip of a growing neuron cell in which actin filaments align longitudinally [32].

Besides excluded volume interactions among the cytoskeletal polymers,

their dynamics or volume constraints imposed by the wall or the other components that play a major role in the cytoskeleton organization, the patterns formed by actin filaments and microtubules adopt in the cell are also result of protein mediated iterations. Crosslinkers, molecular motors and membrane liking proteins help organize the cytoskeleton and also enable it to perform functions such as contraction [33]. Crosslikers are a class of proteins that attach to two cytoskeletal filaments at the same time creating a rigid bridge between them [34]. If crosslinked parallel filaments result is a bundle which is stiffer than just the uncrosslinked filaments packed next too each other. Examples of actin crosslinkers that form bundles are α-actinin found in stress fibers [35] or fimbrin which is present in filopodia [36]. Other crosslinkers such as filamin create networks by binding disorganized actin filaments [37]. This happens mainly in the cortical region of the cell. Molecular motors are proteins that can move along the filaments, having a preferential direction of movement. If a cluster of these motors attaches to two antiparallel filaments simultaneously this generates a traction force, since the motor move on the filaments in opposite directions pulling them together [38]. Myosin II on actin filaments or cytoplasmic dynein on microtubules perform these functions [39]. Membrane linkers can attach cytoskeletal polymers to the membrane [40]. One example is spectrin that attaches the actin cortex to the cell membrane [41].

1.2 Reconstructed systems

Cell are exquisitely complicated systems with a lot of processes happening at the same time. The organization of the cytoskeleton is the result of the combined action of confinement, polymerization dynamics, molecular motors, crosslinkers and membrane interactions. But the way in which each of these factors contributes is still not fully understood. Studying the organization of the cytoskeleton in living cell (*in vivo*) can be thus challenging, since it is hard to isolate these contributions. One way to address this problem is by using reconstructed systems. This bottom-up approach involves studying the factors that influence the cytoskeleton organization individually in a controlled environment (*in vitro*) and using the knowledge gained in this way to rebuild the complete system step by step. Understanding for example the effect of confinement on just plain actin filaments and microtubules permits a better understanding of crosslinked

bundles in confinement.

In cells, both actin filaments and microtubules are subject to confinement. The simplest system to study the effect of confinement on the organization cytoskeleton polymers is just by enclosing them in a container with rigid wall. To get meaningful results the size of the container should be at the cell length scale (10s of microns). To simplify the problem even further it is useful to look at quasi two dimensional geometries, making containers with one dimension much smaller than the other two. This geometry is relevant for the organization of lamelipodia which is essentially an almost flat protrusion where actin filaments are densely packed. The use of photolithographic techniques permits to fabricate containers at this length scale. The experiments of Soares *et al* [42] showed that actin enclosed in shallow chambers (which are 10s of microns in length but only a few micros deep) align to the wall of the confining container. Furthermore, if the density of actin filaments is high enough, the filaments self-organize, aligning along the longest distance available in the the container.

In animal cells the membrane is flexible, being essentially just a lipid bilayer. In this case, bio-mimetic systems such as giant unilamelar vesicles are a useful tool to study the cytoskeleton organization and the membrane-cytoskeleton interaction [43, 44]. There are a variety of techniques for creating giant unilamelar vesicles [45]. These unilamelar vesicles, also called liposomes, are composed of a droplet of buffer containing the proteins of interest (G-actin, tubulin or motors) enclosed by a bilayer of lipids (see figure 1.2 (b)). The cytoskeleton polymers grow inside the liposome, self-organizing. This allows to study the effect of confinement on the organization of actin filaments and cross-linked bundles of actin filaments. This system is also particularly useful to study the actin cortex behavior since actin-membrane proteins can be embedded in the lipid bilayer [46]. As compared to a supported bilayer, where the actin network is bound to a flat bilayer sitting on a surface, liopsomes offer more insight on the cytoskeleton organization since actin-membrane binding is sensitive to curvature [47].

Emulsion droplets are another example of bio-mimetic system [48]. Just as liposomes, they are composed of a droplet of buffer containing the proteins but here, the shell is made of a single layer of lipids. The droplets are immersed in an oil bath (see figure 1.2 (a)). The oil-lipid interface is much stiffer than the water-lipid interface making the droplet harder to deform by cytoskeleton growing inside. This makes it an interesting sys-

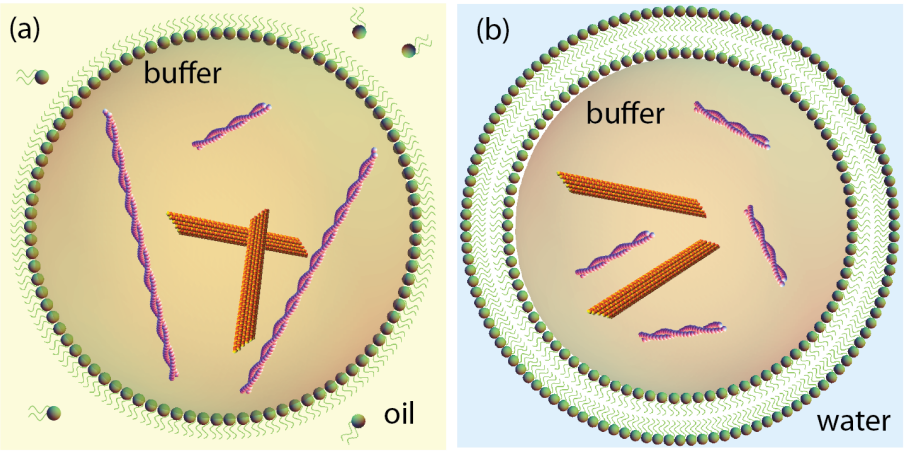

Figure 1.2: Bio-mimetic systems: (a) schematic representation of an emulsion droplet (b) and of a liposome.

tem for studying microtubules. Microtubules are stiff polymers and, when enclosed in a liposome, they create tube like protrusions [49, 50]. This is not the typical situation that we see in cells. There, we more often observe relatively small deformations of the membrane and also bending of the microtubules, which is not happening in vesicles since the resistance of the naked bilayer is too small to bend microtubules. In cells, the actin cortex and other proteins bound to the membrane reinforce the membrane. Therefore, emulsion droplets are ideal systems for studying both plain microtubules and microtubule asters in confinement.

1.3 Biological control and biomimetic applications

Understanding the organization of the cytoskeleton, and what the factors are that influence it, is not only a matter of scientific curiosity. Knowing the role of the various factors such as confinement, dynamics or motor proteins in the organization permits influencing this organization. Since the way the cytoskeletal filaments are organized enables them to fulfill their task in the cell, disrupting their organization prevents them from completing their function. This leads to being able to exert control over the

cell. For example microtubule dynamics is essential for cell division [51]. Stabilizing them with taxol prevents the cell to divide, this mechanism being used in cancer treatment where it stops cancer cells from multiplying [52]. Besides controlling the processes that naturally occur cell, changing cytoskeletal polymers can also be used for new functions. Addition of spermine induces a conformational change in microtubules, reorganizing them into inverted tubulin tubules [53]. This exposes binding sites, which are normally inaccessible since they are hidden inside the microtubule, offering new interaction possibilities.

From a physical point of view, the cytoskeletal filaments are just polymers. They can be several microns long and are thin having a diameter of only 9 nm for actin filaments and 25 nm for microtubules. They also have a relatively stiff, they persistence length being higher than their average length. Furthermore, actin and tubulin have been studied extensively and there is a lot of knowledge on the binding site of these proteins. Also lot of cross-linkers and membrane attaching proteins have been purified from cells. This makes them ideal building blocks. Actin filaments can be successfully used for coating the exterior of microbubbles, increasing the stiffness and elasticity of these structures and reducing gas permeation [54].

From a material science perspective the high persistence length makes actin filaments and microtubules interesting as liquid crystals. If these filaments are only few microns long they are basically stiff rods, but nevertheless have an aspect ratio in the order of 100. The typical liquid crystal mesogens have much smaller aspect ratio and are of maximum a few 100nm in length [55]. Since the effect of a wall extends into the bulk only over the length scale of the liquid crystal particles, studying the confinement effect in such liquid crystal is experimentally challenging. Cytoskeletal filaments can be confined into micron-sized containers making it a interesting system to study. Another bio-mesogen that has similar aspect ratio is the filamentous bacteriophage fd. This rod-like virus has a length of $0.88\mu m$ and a diameter of $6.6nm$ [56]. The persistence length of the wild type virus is $2.8\mu m$ which can be increased to $9.9\mu m$ by a one point mutation (fdY21M) in its coat-protein [57]. Furthermore, the fd virus has the advantage of being highly monodisperse [58] which is hard to achieve with cytoskeletal filaments. This makes it the perfect system to study confinement of liquid crystals leading to new applications.

1.4 Models for the cytoskeleton: from liquid crystals to polymers

Designing a universal model that would predict the organization of the cytoskeleton is unfortunately not possible since the interactions of these polymers among themselves and with the other cell components are too complex and also happen at quite different length scales. However, as is done experimentally with the reconstructed system, we can model a very simple system in order to understand what are the interactions that are relevant for one particular aspect of the organization of the cytoskeleton. Comparing the outcome of the model with experimental data validates the assumptions on which the model relies. This enables us to predict the organization for a wider range of parameters. Understanding simple systems and being able to predict their behavior enables us to build further, using the knowledge gained to understand more complex systems.

One of the first questions that arises is how the polymer-polymer interaction contributes to the the organization of the cytoskeleton. Since one of the important properties of the cytoskeletal filaments is that they are extended objects, occupying a volume, steric repulsion should play a role. Considering that the persistence length of both actin filaments and microtubules is higher than the contour length of these filament, they behave to a certain extent as rigid rods. From liquid crystal physics we know that a fluid composed of asymmetric particles such as rods will self-organize, the patterns formed depending on the density of the particles [59]. For low densities there will be no organization, the particles pointing in random directions, forming a so called isotropic phase. Above a critical value of the density, the system will self-organize in a nematic phase, that is characterized by the fact that all particles point, on average, in the same direction. For further increase of the density, one more degree of organization will arise: in addition to pointing in the same direction the particles also organize in layers. This type of organization is called a smectic phase. The transition density can be predicted, in the limit of thin long rods, by the Onsager model [60]. For shorter rods, Monte Carlo simulations proved useful [61]. Bulk experiments of actin filaments indeed show isotropic and nematic phases [62].

In confinement, the bulk organization of hard rods will be altered by the presence of the walls. In the vicinity of the wall the particles will tend to

align to it [63, 64]. At the same time, if density is high enough, the rod will align to each other. In a container all walls will create preferential directions of alignment which will compete. This mismatch can create a continuous distortion in the direction of alignment of the liquid crystal. There are three basic type of distortions: splay, twist, and bend [65]. Another possibility to accommodate different orientation in a nematic is by creating defects, also called disclinations. Defects are characterized by a singularity in the orientation field. The most common type of defects are the point ones. They are classified according to their topological charge (see figure 1.3). Disclination lines are bounded by two defect points with topological charge $+1/2$ and $-1/2$, whereas disclination walls are believed to be unstable.

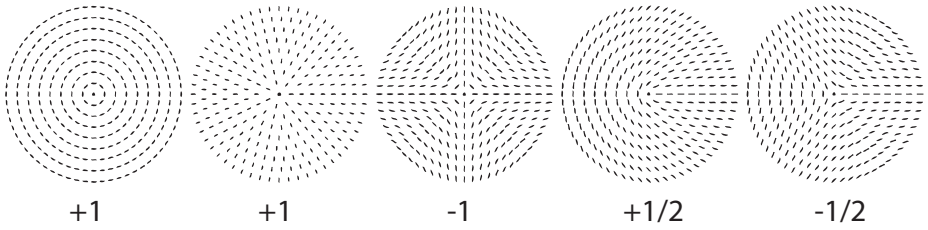

Figure 1.3: Particle orientations around the most common disclination point types and their respective topological charge.

To investigate the organization of stiff rods in confinement we use hard body Monte Carlo simulations [66]. This algorithm allows to start with a random configuration of the system and by small changes converges toward the equilibrium configuration. In the case of hard body Monte Carlo the steps are infinitesimal rotations and translations of the particles. The hard interaction between two object is characterized by in infinite energy when the two objects overlap and is zero otherwise, therefore, when moving particles, they are not allowed overlap with each other or with the walls. Since rigid rods are mathematically best described as spherocylinders, a tube caped with two hemispheres, and spherocylinders have the property that all points on their surface are at one radius distance from the center line of this object, deciding whether two such objects overlap is a matter of computing the distance in between their center lines [67]. The simplest geometry for the confining container is a shallow cuboidal box. This of-

fers an almost two dimensional confining volume with planar walls. We will look at hard rods confined in such geometry and how the mismatch different preferential directions of alignment created by the walls is solved by disclinations in Chapter 2. Using the same method, in Chapter 3, we study the organization of hard rods in a round container and the effect of introducing a volume inaccessible to particles inside this container.

To gain more insight on the effect of confinement in quasi two dimensional systems on the isotropic to nematic transition we also use a modified Onsager model. The bulk model of this microscopic theory is valid in the assumption that the rods are long ($L/D \gg 1$, where L is the length of the rod and D its diameter). The self-alignment of the rods is due to their excluded volume. The excluded volume of two extended objects described by their center of mass is the volume around the center of one of the objects that the center of the other particle cannot occupy. For two long rods the excluded volume a function of the angle between their orientations ($\gamma(\hat{\omega}, \hat{\omega'})$):

$$E\left(\hat{\omega}, \hat{\omega}'\right) = 2L^2 D \sin\gamma\left(\hat{\omega}, \hat{\omega}'\right)$$

The free energy in terms of the density ρ contains an ideal contribution and one due to excluded volume:

$$\beta F\left[\rho\right] = \int d\mathbf{r} d\hat{\omega} \rho\left(\mathbf{r}, \hat{\omega}\right) \left\{\log\left(\mathcal{V}\rho\left(\mathbf{r}, \hat{\omega}\right)\right) - 1\right\} + \frac{1}{2} \int d\mathbf{r} d\hat{\omega} \int d\mathbf{r}' d\hat{\omega}' \rho\left(\mathbf{r}, \hat{\omega}\right) \rho\left(\mathbf{r}', \hat{\omega}'\right) E\left(\hat{\omega}, \hat{\omega}'\right)$$

The ideal part is minimized by an isotropic distribution of the particles whereas the excluded volume contribution is lowest when particles are aligned. For low a density the first term will be dominant but as the density increases the second one will play the main role. In confinement, in addition to the two bulk terms, we add the contribution of the quasi 2D geometry and the confinement effect of the lateral walls. The solutions minimizing this modified free energy functional are presented in the second part of Chapter 2.

Another approach to look at the organization of confined liquid crystals is constructing a continuum mean-field model (Landau-de Gennes [55]). In Chapter 4, we design such a microscopic theory which has the same degrees of freedom as the macroscopic tensor order parameter. This order parameter contains information about both the average direction of alignment

of the particles as well as about how strongly ordered the system is. The confinement is introduced by including an wall anchoring term in the free energy functional.

Approximating cytoskeletal polymers with rigid rods holds in the limit in which the polymers are short compared to their persistence length as it is the case for example in lamelipodia. When cytoskeletal filaments extend from one end of the cell to the other they often bend under the force exerted by the membrane, their behavior is closer to an elastic rod. However, microtubules also exert forces on the membrane, deforming it. If the membrane is stiff enough these deformations are small, the membrane being ellipsoidal instead of spherical. In Chapter 5 we study the mechanical interplay between membrane deformation and the bending of the enclosed microtubules. The equilibrium configuration of this system is reached when the bending energy of both the microtubules and the membrane is minimized. We can tackle this problem in two steps: first we find the minimum energy configuration of the polymers as a function of the surface deformation and then, using the bending energy obtained in the first step and the membrane bending energy, we can find the minimum of the system. For the first step we use a Monte Carlo approach growing bond by bond of one semi-flexible polymer enclosed in a rigid shell. This technique allows us to generate an ensemble of polymers from which bending energy as a function of the shape of the enclosing surface can be extracted. This can then be used in a later stage together with the bending energy of the surface which is computed analytically.

Another situation in which the membrane is involved in organizing the cytoskeleton is the positioning of microtubules asters. As they grow, the microtubules which are growing from the centrosome push against the membrane before they start to buckle. Microtubules can also slide along the membrane and, if cortical motors are bound to the membrane they attach to the microtubules resulting in pulling forces. The combination of these three mechanisms center the aster [68]. Since, in cell division, a spindle that consists of two microtubule asters plays the main role, the exact positioning of two asters is crucial. We expect that two asters enclosed by a membrane, would both center, if there would be no interaction between them. However, during division, asters position themselves at opposite poles of the cell. This implies that there is also repulsion between them. To prove the hypothesis that this repulsion is due to steric effects, in Chapter 6, we look

at the excluded volume of two aster. Unfortunately it is not possible to compute analytically the excluded volume of two asters but, using again a Monte Carlo technique and assuming hard body interaction, we can compute the insertion probability as a function of the separation between the asters. The insertion probability can be directly related to the repulsion force. In steady state, the position of the aster is given by the balance between centering and repulsion.

2

Filaments in square confinement

In cells actin filaments are subject to confinement and, in regions such as lamellipodia, the confinement becomes extreme, densely packed filaments being squeezed in an almost 2 dimensional volume. The patterns emerging are the result of a competition between mutual alignment of the filaments and alignment to the confining walls. Since the size of the lamellipodia is several times smaller than the persistence length of actin filaments, they can to a certain approximation, be modeled as rigid rods. Thus, using Monte Carlo simulations we study rod-like lyotropic liquid crystals confined to a square slab-like geometry with lateral dimensions comparable to the length of the particles. We observe that this system develops linear defect structures upon entering the planar nematic phase. These defect structures flank a lens-shaped nematic region oriented along a diagonal of the square box. We interpret these structures as a compromise between the 2-fold order of the bulk nematic phase and the 4-fold order imposed by the lateral boundaries. A simple Onsager-type theory that effectively implements these competing tendencies is used to model the phase behavior in the center of the box, and shows that the free-energy cost of forming the defect structures strongly offsets the transition-inducing effects of both the transverse and lateral confinement.

2.1 Introduction

Cells are rather crowded environments and both actin filaments and microtubules are forced to organize in the available space, competing with the other cellular components [69]. Therefore confinement is one of the key players in cytoskeleton organization. In lamelipodia, actin filaments are enclosed in a sheet-like protrusion of the cellular membrane [30, 31]. Inside this almost $2D$ region the density of the filaments is high enough so the self-alignment influences the organization. The length of the filaments is comparable to the size of the lamellipodia confinement [29] and smaller than the persistence length. In this regime, actin filaments behave like a liquid crystal composed of rod-like particles.

Confinement in not only relevant for biological polymers with liquid crystalline behavior but also for other organic and inorganic mesogens. Most applications of liquid crystals require these materials to be confined to cells with boundaries specifically treated to orientationally "anchor" the mesogenic molecules, allowing the optical properties of the cell to be controlled [70]. In spite of the fact that the typical dimensions of these cells is continuously shrinking (current state-of-the-art displays employ $\sim 70\mu m$ pixels), commercially employed thermotropic mesogens typically have lengths $\leq 2nm$, so that a continuum description, in which the finite size of the particles is ignored, suffices to predict the relevant orientational patterns [71, 72]. Nature, however, provides us with lyotropic mesogens such as the cytoskeletal filaments F-actin and microtubules, which are generically confined to cellular (sub)volumes with dimensions comparable to that of the particles themselves [69, Chap. 16]. This opens up the possibility to address the fundamental question of liquid-crystalline behaviour in the regime where particle size is important: What is the interplay between boundary effects and mutual interactions when these share the same length scale? Recent experiments on F-actin in photolithographically created micrometer-sized slablike geometries show that intriguing ordering patterns can be observed, even at densities far below that of the bulk transition, that clearly reveal the tug-of-war between alignment with the lateral boundaries and mutual alignment [42]. Both these tendencies derive from the same source: the gain in translational entropy associated with reduction of excluded volume, either with the wall or between the particles, will, with increasing density, outweigh the decrease in orientational entropy due to ordering. However, F-actin has two main drawbacks: the in-situ polymerized

filaments, are likely to be widely polydisperse, and its persistence length of $\sim 16\mu m$ is itself of the order of both the filament length as well as the confinement dimensions, making it likely that enthalpic effects associated with bending also come into play.

Here, we therefore turn to computer simulations to address this question in a systematic manner in the simplest setting, focussing on the same finite planar geometry of the experiments described in [42]. We thus consider a system of length-monodisperse perfectly rigid hard rods in a cuboidal cell with a height significantly smaller than the length of the particles, and a square lateral cross-section, with side length comparable to the length of the particles. We find that in this geometry the system undergoes a transition at a density $\sim 25\%$ below that of the the $3D$ bulk isotropic-nematic transition. The ordered phase is characterized by a lens-shaped nematic region oriented along one of the diagonals with $+1/4$ disclination lines in the corners, and, strikingly, flanked by two disclination walls emerging from the two corners of the other diagonal. This latter phenomenon is a clear signal of the non-trivial impact of finite particle-size.

Although earlier simulation studies have been reported for hard rods in a slab-like geometry [64, 73], these studies employed periodic boundary conditions in the lateral direction, and hence lack the requisite wall-bulk competition effect. Intriguingly, the experiments on vibro-fluidized assemblies of metal rods in planar geometries [74] do consider the same geometry and with hindsight [74, Fig. 4a] also suggests the presence of the linear defect structures. However, these authors argued that the patterns they observed are consistent with continuum elasticity theory in the same geometry, where no defects other than the $+1/4$ point singularities in the corners of the diagonal ordering axis have been reported. Moreover, as a rigorous link between vibrated granular media to the statistical physics of thermally excited systems is lacking, we are at present unable to gauge how far these two systems are truly analogous. A very recent theoretical study by Chen [75], which considers the solution of the $2D$ Onsager theory for infinitely thin needles confined to a square, does not seem to reproduce the linear defect structures, but rather suggests that the particles are at least partially aligned to the cross-diagonal as well, for which we find no evidence.

2.2 Hard-particle simulations

2.2.1 Simulation method

To determine the organization of rigid rods confined into a quasi two-dimensional square container we use a hard-particle Monte Carlo technique. The rigid rods are geometrically described by spherocylindrical particles of diameter D and cylinder length L (see figure 2.1(a)). A convenient way to characterize the particles is using their aspect ratio L/D. The aspect ratios covered in the simulations was 10 - 38. For comparison, the typical aspect ratio of an actin filament is of the order of 100. We adopt the diameter of the particles as unit of length, all distances being expressed in terms of this unit length. The position of the center of mass for each particle is given by the vector $\mathbf{r}_i$. The unit vector $\mathbf{u}_i$ describes the orientation of the particle. Because of the geometry of the particles the system has the symmetry $\mathbf{u}_i \longleftrightarrow -\mathbf{u}_i$. The confining container is a cuboidal volume with rigid walls (see figure 2.1(b)). The length of the square base of the cuboidal simulation volume was fixed to $W = 73$ units, and the height H to either 3 or 6 units. We also consider the equivalent planar geometry by setting $H = 1$. In both cases for which $H \neq 1$, the length of the particles is higher than the height, precluding rotations out of plane, thus defining a quasi-2D geometry. We take the z-axis of our reference frame along the height, and align the remaining two axes with the side walls.

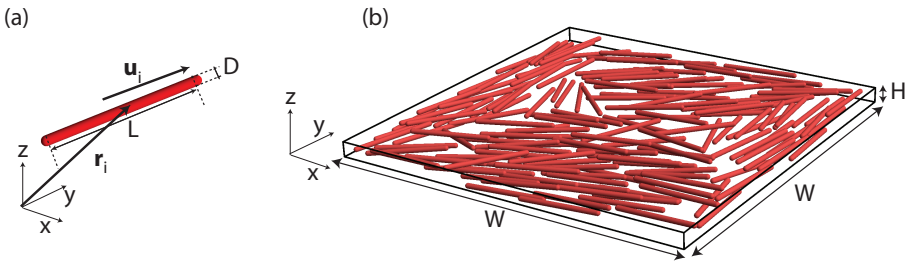

Figure 2.1: Geometrical parameters: (a) sketch of one particle showing the quantities used to describe its geometrical characteristics; (b) sketch of the simulation system.

The interactions between the particles are steric, being described by the potential:

$$U_{ij} = \begin{cases} \infty & \text{if particles i and j overlap} \\ 0 & \text{otherwise} \end{cases}, \tag{2.1}$$

which is fully specified by the purely geometrical condition of no overlap. Spherocylinders are have the property that all points of there surface are located at a distance $D/2$ from the symmetry axis of the cylinder. Therefore determining the overlap of two such objects amounts to determining the minimum distance between the two line segments that are the center lines. If the two this distance is lower than D the spherocylinders overlap. A complete algorithm can be found in [67]. The particle-wall is also steric. Determining the overlap between a particle and the walls of the box is much easier than determining the particle-particle overlap. Since spherocylinders are linear objects it is enough to check that both ends of the center line of the cylinder are located inside the container at a distance larger than the radius from the wall.

The simulation method is a standard Metropolis Monte Carlo scheme [66]. At each step particles are allowed to translate and to rotate. For convenience, the particles are initially arranged in a regular pattern. We checked that the initial configuration has no effect on the final pattern, the result being the same as for a random starting configuration. The most computationally demanding step in our algorithm is the inter-particle overlap check. In order to speed up the simulation we use a Verlet list scheme [76]. This allows us to decrease the number of overlap checks per step, since only particles located in the vicinity of the particle that we attempt to move are considered, and not all the particles in the container. After the equilibration of the system (less than 10% of the total simulation time), we sample configurations that are independent. The distance, in Monte Carlo "time", between two independent configurations is chosen to be the mean diffusion time of particles over half the container size. We typically use 1000 configurations per simulation from which we extract the parameters of interest, averaging over these parameters to obtain the final results.

2.2.2 Tensor order parameter

Apart from the standard second rank tensor order parameter $\mathbf{Q}$ [77]

$$\mathbf{Q} = \frac{1}{N}\left\langle \sum_i \left(\frac{3}{2}\hat{\mathbf{u}}_i \otimes \hat{\mathbf{u}}_i - \frac{1}{2}\mathbf{1}_3 \right) \right\rangle, \tag{2.2}$$

which provides a global measure of the order in our system and is used to monitor the equilibration of the system, we also employ a spatially resolved version, providing local information on the orientational order, defined as

$$\mathbf{Q}^k = \frac{1}{\sum_i l_i^k}\left\langle \sum_i l_i^k \left(\frac{3}{2}\hat{\mathbf{u}}_i \otimes \hat{\mathbf{u}}_i - \frac{1}{2}\mathbf{1}_3 \right) \right\rangle, \tag{2.3}$$

where k labels a specific subvolume, i enumerates the particles in the system, each with its orientation specified by the unit vector $\hat{\mathbf{u}}_i$, l_i^k is the length of particle i inside the subvolume k, $\mathbf{1}_3$ is the 3D unit tensor, and the angular brackets denote equilibrium averaging. In practice, we found that height-spanning rectangular subvolumes of footprint 3.5×3.5 units, were an optimal compromise between resolution and computational effort. The use of the length l_i^k measured along the cylindrical part of the particles, instead of the more formally correct weighting by the volume fraction that particle i occupies in subvolume k, is a computationally convenient approximation, whose error is expected to be small for the highly elongated particles we consider. A frame-independent measure of the local degree of alignment is obtained by considering the largest positive eigenvalue λ_+^k of $\mathbf{Q}^k$, which ranges from 0 for a 3D fully disordered isotropic system, to 1 for a fully aligned system. The corresponding eigenvector $\hat{\mathbf{n}}_+^k$ of $\mathbf{Q}^k$, commonly called the director and defined up to its sign, points along the average direction of the preferred alignment.

2.2.3 Results

Changing the volume fraction of the particles — $\eta = \rho V_{part}$, with ρ the number density and $V_{part} = 1/4\pi D^2 L + 1/6\pi D^2$ — we generically observe three types of orientational patterns within the simulation volume. All of them are in-plane structures, characterized by a smallest eigenvalue of $\mathbf{Q}$ of $\lambda_- \simeq -1/2$. For small volume fractions, we observe local alignment of

the rods along the four side walls (fig 2.2 (a), (d), and (g)). Moving to the middle of the volume the degree of order rapidly falls off, with the center essentially fully isotropic in-plane corresponding to $\lambda_+ \simeq 1/4$. In this regime, the wall induced ordering appears dominant.

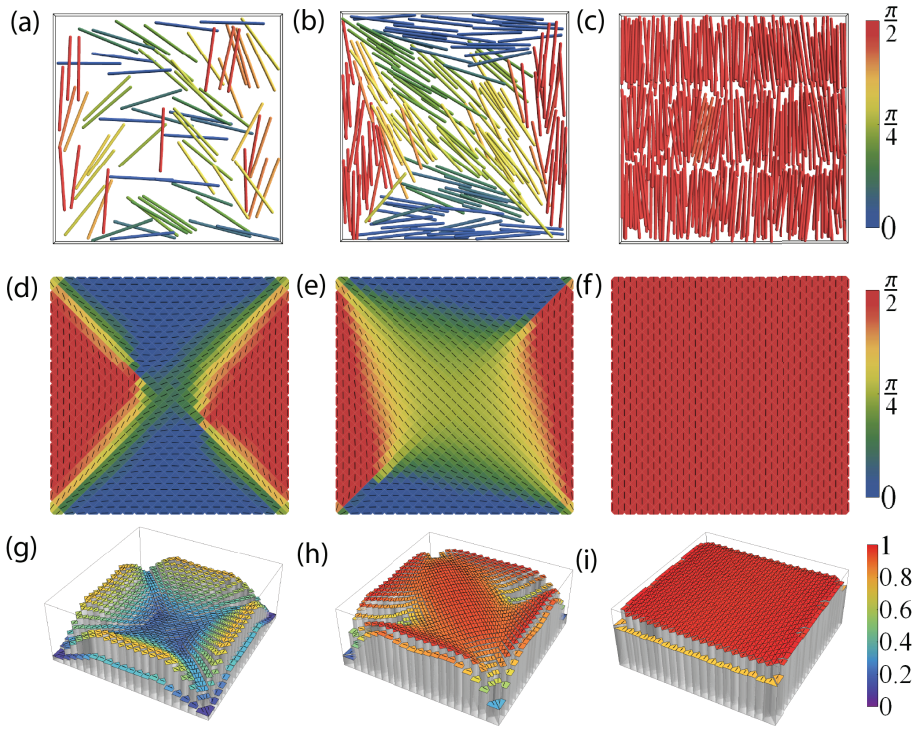

Figure 2.2: Distinct states of the system: isotropic with wall alignment (a,d,g), lens-shaped nematic (b,e,h), and smectic(c,f,i). (a-c) Snapshots of typical configurations (top view). Color code corresponds to the minimum angle between the long axis of the rod and the $\boldsymbol{x}$ axis (scale bar on the right hand side). (d-e) Local orientation of the particles; Color code corresponds to the minimum angle between the local director $\hat{\mathbf{n}}_+^k$ and the $\boldsymbol{x}$ axis (scale bar on the right hand side).(g-i) Local degree of order of the system λ_+^k. All results presented in this figure are obtained for $H = 3$ and $L/D = 20$. Volume fractions are $\eta = 0.075$ for (a), (d), and (e), $\eta = 0.175$ for (b), (e), and (h), and $\eta = 0.3$ for (c), (f), and (i).

At higher volume fractions, the system becomes smectic (see fig 2.2 (c), (f), and (i)), with the number of smectic layers dependent on the aspect ratio of the particles. For the particle lengths considered we observed from 2 up to 4 smectic layers (see fig 2.3). The distance separating the layers also depends on the ratio between the particle length and the box size. Here the excluded-volume driven mutual alignment mechanism is able to overcome the barrier caused by disaligning the particles at the two side walls along the smectic director.

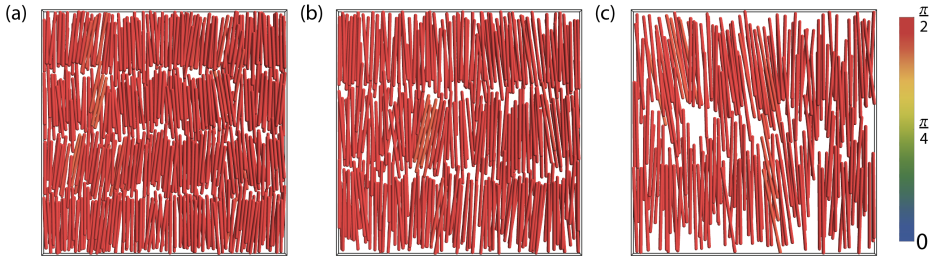

Figure 2.3: Number of smectic layers confined in a box with $H = 3$ *and* $W = 73$ *for different particle length: (a) 4 layers for* $L/D = 15$ *at* $\eta = 0.35$*, (b) 3 layers for* $L/D = 20$ *at* $\eta = 0.3$ *and (c) 2 layers for* $L/D = 25$ *at* $\eta = 0.24$*.*

At intermediate values of the volume fraction, the competition between the globally incompatible 4-fold ordering induced by the side walls and 2-fold nematic order due to mutual alignment leads to a compromise structure. We observe a lens-shaped nematic domain along one of the diagonals (see fig 2.2 (b)). This domain is flanked by two wall defect structures emanating from the corners of the other diagonal. As we approach these corners, the degree of order drastically decreases (see fig 2.2 (h)). Crossing the defect wall, the preferred direction of the particles makes a finite jump (see fig 2.2 (e)). The results in figure 2.2 (d-i) are obtained by averaging over the local orientation of the particles and the local degree of order of independent configurations from the same simulations. We observed that these patterns are very stable and with statistical errors typically two orders of magnitude smaller than the quantity being measured in each subvolume, except for the subvolumes that contain the disclinations, where the fluctuations are much more prominent.

2.2.4 Disclination walls

A disclination (as defined by de Gennes and Prost [55], pg 166) is a discontinuity in the orientation of the nematic director filed. The discontinuity can be located at a single point (point disclination), on a line (line disclination), or a surface (sheet or wall disclination). For a point disclination, the topological charge is given by the angular variation (divided by 2π) of the nematic director along a closed curve around this point. A line disclination can be constructed out of a line of point disclinations, and by extension this has the same strength as the points. The same definition can be extended to walls, in case the angular variation is limited in one direction. The pattern characterized by the lens-shaped nematic stabilized by defect structures is an in-plane phase which is indicated by $\lambda_- \simeq -0.5$. The three dimensional arrangement of the particles is essentially the repetition of this planar pattern on the z-axis, the planar line defects creating a wall. We therefore look at the variation of the nematic director in neighboring subvolumes on our square mesh. To properly characterize these disclination walls, we define an angular deficit parameter δ on the lattice dual to our square mesh of subvolumes. If $\hat{\mathbf{n}}^1, \hat{\mathbf{n}}^2, \hat{\mathbf{n}}^3$ and $\hat{\mathbf{n}}^4$ are the four directors of the subvolumes that surround a point on the dual lattice in a fixed either clockwise- or anticlockwise order (see figure 2.4 (b)), then the angular deficit is defined as

$$\delta = min\angle\left(\hat{\mathbf{n}}^1, \hat{\mathbf{n}}^2\right) + min\angle\left(\hat{\mathbf{n}}^3, \hat{\mathbf{n}}^4\right), \tag{2.4}$$

where the angle chosen is the minimal one obtained when the otherwise arbitrary signs of the director are varied. For a homogeneous nematic state this parameter vanishes. For the case of a gradual distortion, say a bend deformation, the parameter should vary smoothly. At any kind of singularity, however, the parameter provides a localized signal. As figure 2.4 (b) shows, the parameter is high along the disclination walls, with a maximum in the corners, corresponding to the almost $\pi/2$ difference in angle caused by the wall induced ordering. As one moves along the diagonal, the particles on either side gradually splay away from the alignment at the wall, causing δ to decrease to a minimum, when the edge of the lens-shaped nematic domain is reached. Note that δ also picks up a signal at the $+1/4$ strength disclinations in the corners of the nematic domain, but this effect does not penetrate very far into the bulk.

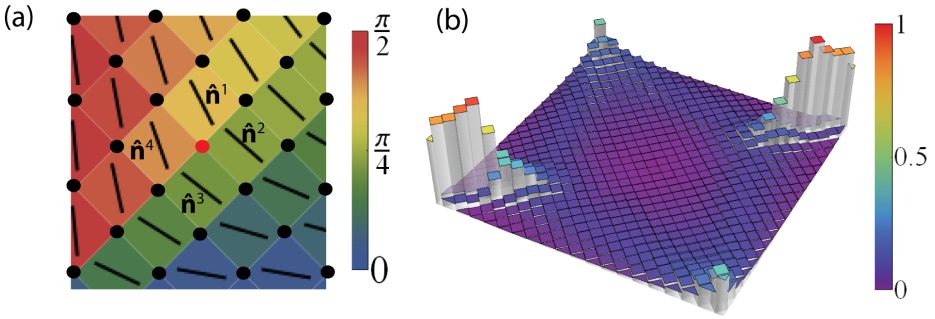

Figure 2.4: (a) Representation of the quantities used to compute the angular deficit parameter. The color of the square subvolumes codes the angle of the directors (shown as back lines) with the Ox-axis, according to the scale bar on the right. The dots represent points on the dual lattice, the red dot corresponding to the labeled directors. (b) Disclination parameter δ scaled by its maximum value π (color code given by the scale bar on the right). System parameters: $H = 3$, $L/D = 20$ and volume fraction $\eta = 0.175$.

2.2.5 Isotropic-nematic transition

The tensor order parameter defined in equation (2.2) characterizes the system as a whole, its highest eigenvalues giving the overall degree of order and the corresponding eigenvector ($\hat{\mathbf{n}}$) showing the average orientation direction. In the confined isotropic phase we see that $\hat{\mathbf{n}}$ covers all angles in the plane from $-\pi/2$ to $\pi/2$, being homogeneously distributed (see figure 2.5, left panels). The same behavior characterizes the bulk system, the confinement effect being unnoticeable in this parameter. This behavior is due to the the 4-fold symmetry of the system, the particles aligning to one wall being "canceled out" by the one aligned to the perpendicular wall. As the density increases the system spends more time in a given configuration, the switching between configurations occurring less often (see figure 2.5, central panels). When the lens-shaped nematic is formed the the average orienetaion of the systems foms an angle of $-\pi/4$ or $\pi/4$ with the x-axis, depending on which diagonal the system chooses (see figure 2.5, right panels).

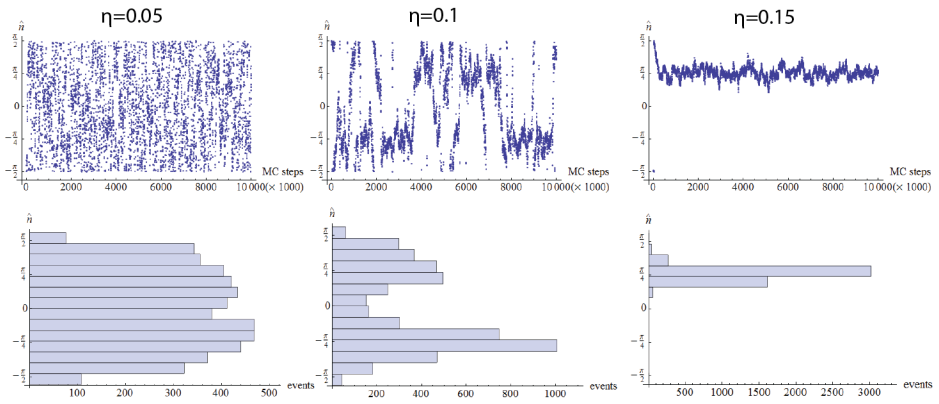

Figure 2.5: Average direction of alignment during the course of a simulation (upper panels) and histogram of angles between the orientation and the x-axis (lower panels) for different densities. All data in this figure is obtained for $L/D = 20$, $H = 3$ and, $W = 73$).

To gain more insight on the nature of the transition from the isotropic to the nematic state it is useful to look at the local degree of alignment (λ_+^k). In the confined isotropic organization only the middle of the slab is actually in an almost planar isotropic phase, as next to the wall the particles are always aligned (see figure 2.6 (a)-(c)). As the density increases the degree of order both in the middle of the container and along the wall increases. However the wall alignment increases faster with density than the alignment in the middle. Both diagonals are symmetric, the degree of order being low along them. When the lens shape nematic is formed along one of the diagonals, the symmetry is broken, one of the diagonals being highly ordered (see figure 2.6 (e),(f)).

To quantify the density dependence of development of order in our system, we study the value of the order parameter λ_+^{mid} of the subvolume exactly in the middle of the slab, i.e. the point farthest removed from the strong boundary-induced ordering at the side walls, which is high irrespective of the density. We tracked λ_+^{mid} for particles of aspect ratio $L/D = 15$, 20 and 25, for a range of volume fractions, spanning the isotropic, nematic and smectic regimes. In order to optimally isolate the influence of confinement and remove the known dependence of the mutual interactions on particle length, we scale all volume fractions by the value of the packing

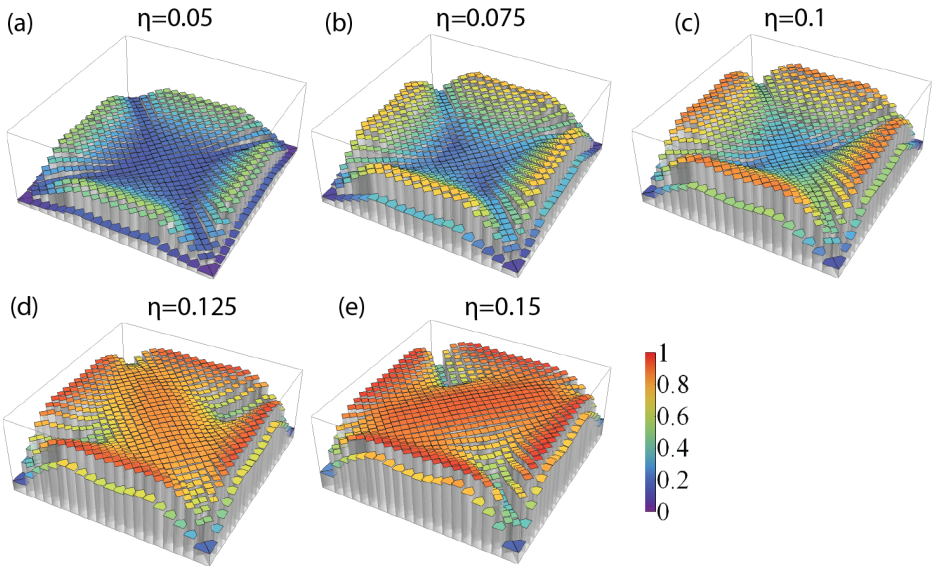

Figure 2.6: Local degree of alignment (λ_+^k) for densities (η) increasing from (a) to (e). (a), (b) and, (c) correspond to phases characterized by an isotropic organization in the middle of the slab and wall alignment; (d) and (e) show lens-shaped nematic along one of the diagonals and defect walls along the other diagonal ($L/D = 20$, $H = 3$ and, $W = 73$).

fraction at the bulk isotropic-nematic, which we obtain from the simulations of Bolhuis and Frenkel [78], which defines the reduced volume fraction $\bar{\eta} = \eta/\eta_c\,(3D)$. Under this scaling the three curves indeed collapse reasonably well onto a single master curve (see figure 2.7).

At low volume fractions we expect the system to have an isotropic in-plane distribution, corresponding to $\lambda_+^{mid} \simeq 1/4$. The fact that the simulation data only reproduce this expected value at slightly higher volume fractions is due to the unavoidable undersampling of contributing configurations at low volume fractions. At a reduced volume fraction $\bar{\eta}_c \simeq 0.75$ we observe a strong first-order jump to a value $\lambda_+^{mid} \simeq 0.8$. Beyond this point, λ_+^{mid} increases, gradually saturating towards its maximal value $\lambda_+^{mid} \lesssim 1$, with only a small dip observed at reduced volume fraction $\bar{\eta}_s \simeq 1.5$, which marks the transition to the smectic state, in which the particles have to rotate from the box diagonal to either of the two shorter symmetry axes.

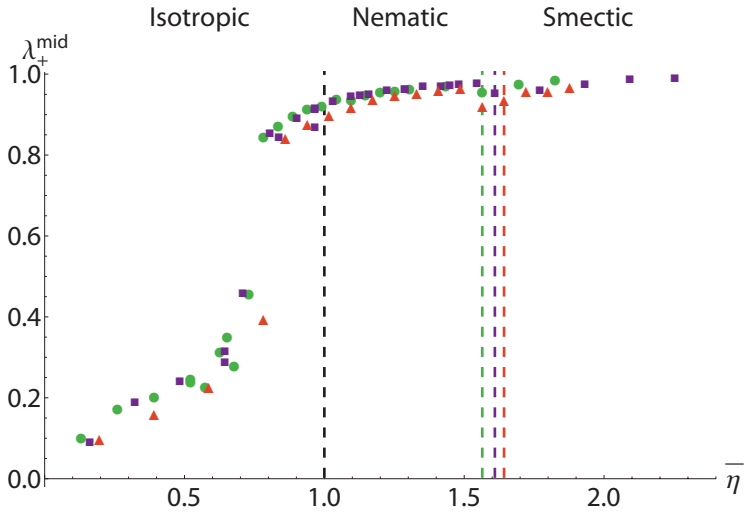

Figure 2.7: Local degree of order λ_+^{mid} in the middle of the slab as a function of the density scaled by the bulk isotropic-to-nematic transition density. Simulation results at $H = 3$ for $L/D = 15$ (green circles), $L/D = 20$ (purple squares) and $L/D = 25$ (red triangles). The green, purple and red dashed vertical lines located between $\bar{\eta} = 1.5$ and 1.7 correspond to the nematic to smectic transition observed in the simulation in confinement for rods with $L/D = 15$, 20 and 25 respectively (from left to right). The black dashed line at $\bar{\eta} = 1.0$ marks the bulk isotropic-nematic transition.

2.2.6 Results for $2D$ system ($H = 1$)

In order to check whether the effects reported above survive in the limit of a true $2D$ system, we also performed simulations by setting $H = 1$. In this system in which the particles are fully confined to the plane we again observe the same three distinct states: an isotropic phase with wall alignment in the vicinity of the boundary, a lens-shaped nematic and a layers arrangement. The density dependence of these states and the behavior of the order in the middle of the slab is very similar to the quasi-$2D$ case (see figure 2.2.6 (a)). Most importantly, the lens-shaped nematic is again is stabilized by linear defects, which in this geometry are now pure line defects.

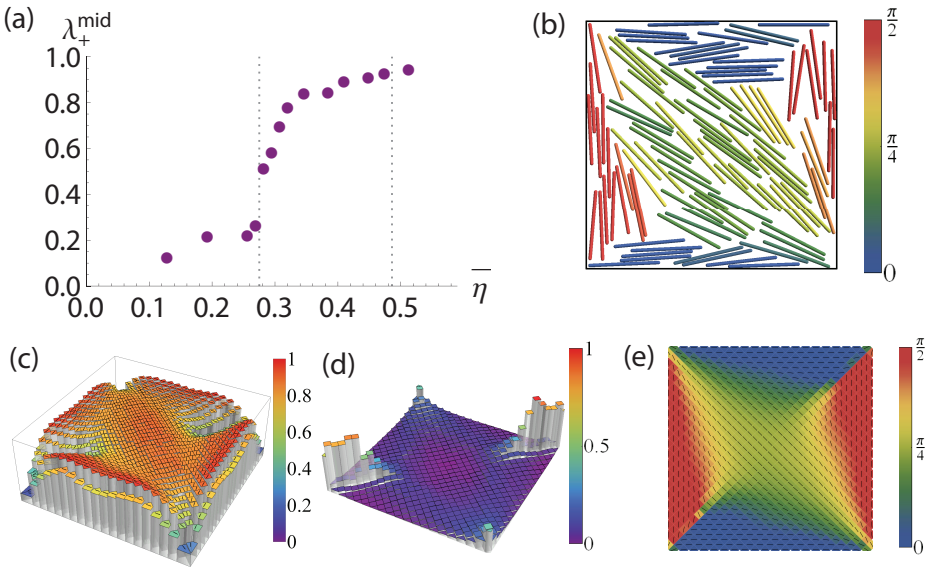

Figure 2.8: Results for 2D system (box-height $H = 1$ and $L/D = 20$): (a) λ_+^{mid} versus 2D packing fraction $\eta \equiv \frac{ND(\pi D/4 + L)}{W^2}$ (where N is the number of particles), showing the location of the I-N transition (left-hand dotted vertical line) and the 2D smectic transition (right-hand dotted vertical line). (b) snapshot at $\eta = 0.41$ (c) local order parameter (d) defect parameter (e) orientation pattern.

2.3 Onsager-type microscopic toy model

A notable result of our simulations is that the isotropic-nematic ordering transition takes place at a value of the density relatively close to that of the homogeneous bulk. The results of Cosentino et al. [73] suggest that the transverse slab-like confinement strongly induces the in-plane ordering transition, which in their case happens at a reduced volume fraction $\bar{\eta}_c \simeq 0.25$, this value being fairly insensitive to the height of the slab, only increasing slightly when true $2D$ confinement is approached, where the nature of the transition changes to one driven by the condensation of bulk topological defects. Moreover, one also expects that by itself the pre-alignment effect caused by the interactions with the side walls would also facilitate

the transition. Our results, however, indicate that, in the strong lateral confinement limit, nematic in-plane order is inevitably accompanied by the appearance of extended defect structures. These defects obviously carry a free-energy penalty, which potentially offsets the order-promoting effect of the transverse and lateral confinement.

To illustrate the effect of these competing mechanism, we designed an Onsager-type [60] microscopic toy model that implement all the relevant effects, albeit in an effective manner. We thus consider a monodisperse system of highly elongated hard rods of length $L \gg D$. In addition to the ideal term, the free energy should include four other contributions. The first contribution comes from the excluded volume effect, the packing of rods being more efficient, at high densities, as the rods align to each other. The mutual excluded volume at fixed relative orientations in this limit given by $E(\hat{\omega}, \hat{\omega}') = 2L^2 D \sin\gamma(\hat{\omega}, \hat{\omega}')$, where $\gamma(\hat{\omega}, \hat{\omega}')$ is the angle between two rods with orientations $\hat{\omega}$ and $\hat{\omega}'$. The second contribution is due to the confinement of the particles in a quasi- 2D geometry: the particles have a limited out-of plane rotation set by the depth of the confining container. To mimic the confinement due to the finite height of the system, we impose a potential $\beta W_{\parallel}(\hat{\omega}) = \xi_{\parallel} P_2(\hat{\mathbf{z}} \cdot \hat{\omega})$, with P_2 the second-rank Legendre polynomial, and the prefactor is chosen to be $\xi_{\parallel} = \left(L^2/H^2\right)$, which matches the width of the Boltzmann weight of this potential to the maximal out-of-plane angle the rods can adopt, and any other non-dimensional factors are absorbed into the inverse temperature scale β. The third contribution comes from the confinement imposed by the lateral walls, which forces the particles aligning to each of them. By symmetry, the effect of the side walls should be 4-fold symmetric in terms of the in-plane azimuthal angle φ. We implement this by adding the potential $\beta W_{\perp}(\hat{\omega}) = -\xi_{\perp} R_4^4(\hat{\omega}) \propto \cos(4\varphi)$, where $R_l^m(\hat{\omega})$ is a real spherical harmonic (see Appendix 2.5.1 for details) and $\xi_{\perp}$ is a free parameter. Finally, the forth contribution we include is a penalty associated with the defect structures, which we take to be proportional to the magnitude of in-plane order measured by the standard biaxial order parameter $T = \sqrt{\left\langle R_2^2 \right\rangle^2 + \left\langle R_2^{-2} \right\rangle^2}$, and whose strength is set by the free parameter ξ_d. This leads to the following free energy functional in terms of a normalized orientational distribution function $\psi(\hat{\omega})$:

$$\frac{\beta F[\psi]}{N} \equiv \Phi[\psi] = \int d\hat{\omega}\psi(\hat{\omega})\{\log\psi(\hat{\omega}) - 1\} + \rho L^2 D \int d\hat{\omega} \int d\hat{\omega}'\psi(\hat{\omega})\psi(\hat{\omega}')\sin\gamma(\hat{\omega},\hat{\omega}') + \xi_{\parallel}\int d\hat{\omega}\psi(\hat{\omega})R_2^0(\hat{\omega}) - \xi_{\perp}\int d\hat{\omega}\psi(\hat{\omega})R_4^4(\hat{\omega}) + \xi_d\left\{\left(\int d\hat{\omega}\psi(\hat{\omega})R_2^2(\hat{\omega})\right)^2 + \left(\int d\hat{\omega}\psi(\hat{\omega})R_2^{-2}(\hat{\omega})\right)^2\right\}^{\frac{1}{2}},$$

where ρ is the number density.

To obtain the orientational distribution function (further abbreviated as ODF) that minimizes the above free energy, we consider the stationarity equation

$$\frac{\delta}{\delta\psi(\hat{\omega})}\Phi[\psi] = \beta\mu, \tag{2.5}$$

where the chemical potential μ serves as a Lagrange multiplier enforcing the normalization of the ODF. Explicitly the stationarity equation becomes

$$\log\psi(\hat{\omega}) + \eta\int d\hat{\omega}'\sin\gamma(\hat{\omega},\hat{\omega}')\psi(\hat{\omega}') + \xi_{\parallel}R_2^0(\hat{\omega}) - \xi_{\perp}R_4^4(\hat{\omega}) + \xi_d\left\{\frac{\langle R_2^2\rangle}{\sqrt{\langle R_2^2\rangle^2 + \langle R_2^{-2}\rangle^2}}R_2^2(\hat{\omega}) + \frac{\langle R_2^{-2}\rangle}{\sqrt{\langle R_2^2\rangle^2 + \langle R_2^{-2}\rangle^2}}R_2^{-2}(\hat{\omega})\right\} = \beta\mu. \tag{2.6}$$

We now note that the excluded volume interaction term is symmetric under the inversion of the direction of the particles, as well as all the additional terms, so in the expansion of the ODF

$$\psi(\hat{\omega}) = \sum_{l=0}^{\infty}\sum_{m=-l}^{l}\psi_{lm}R_l^m(\hat{\omega}) \tag{2.7}$$

we can ignore terms with l odd. Moreover, because of its global rotational invariance the excluded volume term is agnostic about the value of m, and the additional terms only couple to even values of m so without loss of generality we can also restrict ourselves to m even. For numerical purposes, rather than working with the expansion Eq. (2.7), it is more convenient to work with a cumulant representation

$$\psi\left(\hat{\omega}\right) = \exp\left(\sum_{l=0}^{l_*}{}' \sum_{m=-l}^{l}{}' c_{lm} R_l^m\left(\hat{\omega}\right)\right) = \frac{1}{Z\left[c_{lm}\right]} \exp\left(\sum_{l=2}^{l_*}{}' \sum_{m=-l}^{l}{}' c_{lm} R_l^m\left(\hat{\omega}\right)\right), \quad (2.8)$$

where l_* is a cut-off and the primes denote restriction to even values in the summations and the normalization is simply

$$Z\left[c_{lm}\right] = \int d\hat{\omega} \exp\left(\sum_{l=2}^{l_*}{}' \sum_{m=-l}^{l}{}' c_{lm} R_l^m\left(\hat{\omega}\right)\right). \quad (2.9)$$

Note that this representation guarantees positivity of the ODF, and requires far fewer terms to describe strongly peaked distributions. Inserting into the stationarity equation Eq. (2.6) and projecting out the coefficient using the orthogonality relations Eq. (2.19), we find

$$\begin{aligned}\frac{4\pi}{2l+1} c_{lm} + \eta \int d\hat{\omega} R_l^m\left(\hat{\omega}\right) \int d\hat{\omega}' \sin\gamma\left(\hat{\omega}, \hat{\omega}'\right) \psi\left(\hat{\omega}'\right) + \\ \frac{4\pi}{2l+1} \xi_{\parallel} \delta_{l,2} \delta_{m,0} + \frac{4\pi}{2l+1} \xi_{\perp} \delta_{l,4} \delta_{m,4} + \\ \frac{4\pi}{2l+1} \xi_d \delta_{l,2} \delta_{m,2} \frac{\left\langle R_2^2 \right\rangle}{\sqrt{\left\langle R_2^2 \right\rangle^2 + \left\langle R_2^{-2} \right\rangle^2}} + \\ \frac{4\pi}{2l+1} \xi_d \delta_{l,2} \delta_{m,-2} \frac{\left\langle R_2^{-2} \right\rangle}{\sqrt{\left\langle R_2^2 \right\rangle^2 + \left\langle R_2^{-2} \right\rangle^2}} = 0. \quad (2.10)\end{aligned}$$

We can expand

$$\sin\gamma\left(\hat{\omega}, \hat{\omega}'\right) = \sum_{l=0}^{\infty}{}' s_l R_l^0\left(\hat{\omega}, \hat{\omega}'\right), \quad (2.11)$$

where following Kayser and Raveche [79] (see also [80], entry 7.132)

$$\begin{aligned}\frac{4\pi}{(4n+1)}s_{2n} &= \int d\hat{\omega}\sin\gamma\left(\hat{\omega},\hat{\omega}'\right)P_{2n}\left(\hat{\omega}\cdot\hat{\omega}'\right)\\ &= 2\pi\int_{-1}^{1}dx\,\sqrt{1-x^2}P_{2n}\left(x\right)\\ &= -2\pi\frac{\pi}{4}4^{1-2n}\frac{1}{n}\left(\begin{array}{c}2n-2\\ n-1\end{array}\right)\frac{1}{n+1}\left(\begin{array}{c}2n\\ n\end{array}\right),\end{aligned} \tag{2.12}$$

so that

$$s_{2n} = -2\pi\frac{4n+1}{n\left(n+1\right)}4^{-(2n+1)}\left(\begin{array}{c}2n-2\\ n-1\end{array}\right)\left(\begin{array}{c}2n\\ n\end{array}\right). \tag{2.13}$$

We now note that (see Eq. (2.20))

$$\int d\hat{\omega}R_l^m\left(\hat{\omega}\right)R_{l'}^0\left(\hat{\omega},\hat{\omega}'\right) = \frac{4\pi}{2l+1}\delta_{l,l'}R_l^m\left(\hat{\omega}'\right), \tag{2.14}$$

so that for l even

$$\begin{aligned}&\int d\hat{\omega}R_l^m\left(\hat{\omega}\right)\int d\hat{\omega}'\sin\gamma\left(\hat{\omega},\hat{\omega}'\right)\psi\left(\hat{\omega}'\right) =\\ &\sum_{l'\text{ even}}s_l\int d\hat{\omega}'\int d\hat{\omega}R_l^m\left(\hat{\omega}\right)R_{l'}^0\left(\hat{\omega},\hat{\omega}'\right)\psi\left(\hat{\omega}'\right) =\\ &\qquad\frac{4\pi}{2l+1}s_l\int d\hat{\omega}'R_l^m\left(\hat{\omega}'\right)\psi\left(\hat{\omega}'\right) \equiv \frac{4\pi}{2l+1}s_l\left\langle R_l^m\right\rangle\end{aligned} \tag{2.15}$$

so that for $l \geq 2$

$$\begin{aligned}&c_{lm} + \eta s_l\left\langle R_l^m\right\rangle + \xi_{\parallel}\delta_{l,2}\delta_{m,0} - \xi_{\perp}\delta_{l,4}\delta_{m,4}\\ &+\xi_d\left\{\delta_{l,2}\delta_{m,2}\frac{\left\langle R_2^2\right\rangle}{\sqrt{\left\langle R_2^2\right\rangle^2+\left\langle R_2^{-2}\right\rangle^2}} + \delta_{l,2}\delta_{m,-2}\frac{\left\langle R_2^{-2}\right\rangle}{\sqrt{\left\langle R_2^2\right\rangle^2+\left\langle R_2^{-2}\right\rangle^2}}\right\} = 0.\end{aligned} \tag{2.16}$$

We can determine fairly accurate solutions to this functional equation by making a cumulant expansion of $\psi\left(\hat{\omega}\right)$ in terms of real spherical harmonics up to rank $l = 4$. The resulting set of coupled equations for the expansion parameters is then solved by a relaxation procedure (for details please consult the appendix 2.5.1). In figure 2.9 we demonstrate that the

simulation results are readily fitted using a Least Mean Square fit by the parameters $\xi_\perp = 0.07$ for $L/D = 15, 25$ and $\xi_\perp = 0.08$ for $L/D = 20$, and $\xi_d = 0.01$. We also note that the term representing the transverse confinement, either by itself, or in conjunction with the one describing the coupling to the lateral walls, lowers the transition density to $\lesssim 50\%$ of the bulk value. The system, however, is very sensitive to the defect term, which, although small in amplitude, raises the transition density to the observed value.

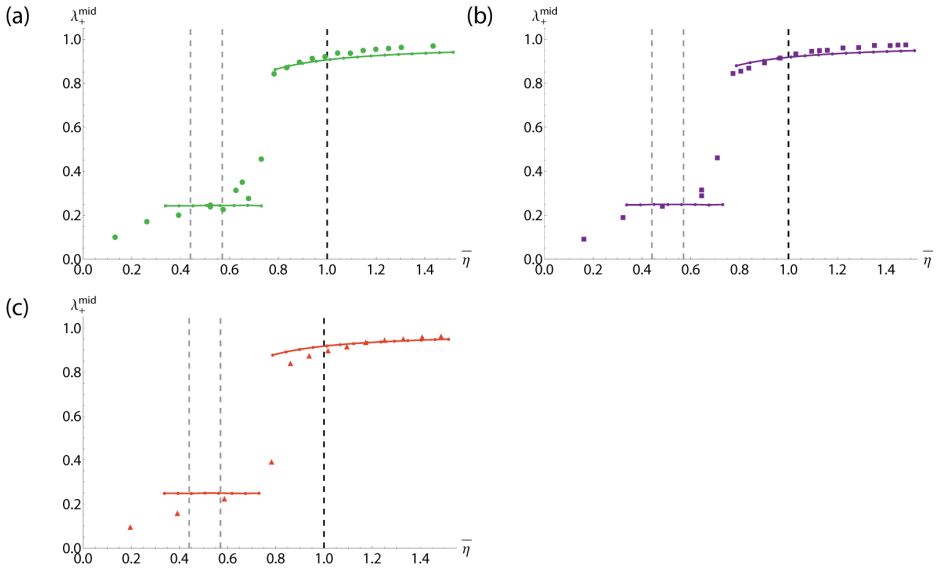

Figure 2.9: Local degree of order λ_+^{mid} in the middle of the slab as a function of the density scaled by the bulk isotropic-to-nematic transition density. Simulation results at $H = 3$ for $L/D = 15$ (green circles) (a), $L/D = 20$ (purple squares) (b) and, $L/D = 25$ (red triangles) (c) and model fit curve in the same color as simulation data. The black dotted line at $\bar{\eta} = 1.0$ marks the bulk isotropic-nematic transition. The gray vertical lines correspond, from left to right, to the location of the transitions in the model for $\xi_d = 0$, $\xi_d = \xi_\perp = 0$, and the bulk isotropic-nematic transition.

2.4 Conclusion

Our results complement a number of studies that have appeared of hard rods confined to $2D$ circular disks — simulations with homeotropic boundary conditions [81], density functional theory [82] and very recently simulations with both homeotropic and planar boundary conditions [83] — or a $3D$ spherical volume [84] with planar degenerate boundary conditions. We note that in all these cases one expects to find stable configurations either a single (homeotropic b.c.) or a polarly opposite pair of disclination points (planar b.c). These defects structures, however, are purely topological in origin, and well-described by continuum theory in limit of strong anchoring and weak elastic effects (see e.g. [85]), and hence are not dependent on the finite size of the particles. The same holds for more complex situations, such as rods on the surface of a sphere [81, 86] and liquid crystals between concentric spherical shells [87, 88].

This highlights the non-trivial nature of the stable linear defect structures we have observed. Experimental validation of these results clearly raises the challenge of producing sufficiently rigid monodisperse colloidal rods of the right dimensions and the ability to resolve orientational patterns at submicron resolutions. Also, from a theory perspective the proper approach is, as yet, probably lacking, as the results of [75] suggest that we are dealing with a phenomenon that requires a beyond-second-virial-coefficient-level density functional theory. Finally, it is interesting to see what the implications of these findings are for other confinement geometries.

2.5 Appendix:

2.5.1 Modified real spherical harmonics

To obtain a suitable basis set for expanding real orientational distributions in our mean field model, we start from the definition of the complex spherical harmonics using the Condon-Shortley normalization [89]

$$C_l^m(\hat{\omega}) = \sqrt{\frac{4\pi}{2l+1}} Y_l^m(\hat{\omega}). \tag{2.17}$$

Real versions of these functions are then defined through

$$R_l^m(\hat{\omega}) = \begin{cases} C_l^0(\hat{\omega}) & m = 0 \\ \frac{1}{2}\sqrt{2}\left\{C_l^m(\hat{\omega}) + C_l^m(\hat{\omega})^*\right\} & m > 0 \\ \frac{1}{2i}\sqrt{2}\left\{C_l^{|m|}(\hat{\omega}) - C_l^{|m|}(\hat{\omega})^*\right\} & m < 0 \end{cases} \tag{2.18}$$

The orthogonality relations for these functions are simply

$$\int d\hat{\omega} R_l^m(\hat{\omega}) R_{l'}^{m'}(\hat{\omega}) = \frac{4\pi}{2l+1}\delta_{l,l'}\delta_{m,m'}. \tag{2.19}$$

and the harmonic addition theorem becomes

$$R_l^0\left(\hat{\omega}\cdot\hat{\omega}'\right) = \sum_{m=-l}^{l} R_l^m(\hat{\omega}) R_l^m\left(\hat{\omega}'\right) \tag{2.20}$$

Parametrizing the unit sphere with the standard spherical angles, $\hat{\omega} = (\sin\theta\cos\varphi, \sin\theta\sin\varphi, \cos\theta)$, we list these functions for l, m even, up to $l = 4$

$$R_0^0(\hat{\omega}) = 1 \tag{2.21}$$

$$R_2^{-2}(\hat{\omega}) = \frac{1}{2}\sqrt{3}\sin^2\theta\sin 2\varphi \tag{2.22}$$

$$R_2^0(\hat{\omega}) = \frac{1}{2}\left(3\cos^2\theta - 1\right) \tag{2.23}$$

$$R_2^2(\hat{\omega}) = \frac{1}{2}\sqrt{3}\sin^2\theta\cos 2\varphi \tag{2.24}$$

$$R_4^{-4}(\hat{\omega}) = \frac{1}{8}\sqrt{35}\sin^4\theta\sin 4\varphi \tag{2.25}$$

$$R_4^{-2}(\hat{\omega}) = -\frac{1}{4}\sqrt{5}(7\cos^4\theta - 8\cos^2\theta + 1)\sin 2\varphi \tag{2.26}$$

$$R_4^0(\hat{\omega}) = \frac{1}{8}(35\cos^4\theta - 30\cos^2\theta + 3) \tag{2.27}$$

$$R_4^2(\hat{\omega}) = -\frac{1}{4}\sqrt{5}(7\cos^4\theta - 8\cos^2\theta + 1)\cos 2\varphi \tag{2.28}$$

$$R_4^4(\hat{\omega}) = \frac{1}{8}\sqrt{35}\sin^4\theta\cos 4\varphi \tag{2.29}$$

The standard second rank order parameter tensor $\mathbf{Q}$ can then be ex-

pressed in terms of the functions as

$$\mathbf{Q} = \left\langle \frac{1}{2}\left(3\hat{\omega}\otimes\hat{\omega} - \mathbb{I}\right)\right\rangle = \begin{pmatrix} -\frac{1}{2}\left\langle R_2^0\right\rangle + \frac{1}{2}\sqrt{3}\left\langle R_2^2\right\rangle & \frac{1}{2}\sqrt{3}\left\langle R_2^{-2}\right\rangle & -\frac{1}{2}\sqrt{3}\left\langle R_2^1\right\rangle \\ \frac{1}{2}\sqrt{3}\left\langle R_2^{-2}\right\rangle & -\frac{1}{2}\left\langle R_2^0\right\rangle - \frac{1}{2}\sqrt{3}\left\langle R_2^2\right\rangle & -\frac{1}{2}\sqrt{3}\left\langle R_2^{-1}\right\rangle \\ -\frac{1}{2}\sqrt{3}\left\langle R_2^1\right\rangle & -\frac{1}{2}\sqrt{3}\left\langle R_2^{-1}\right\rangle & \left\langle R_2^0\right\rangle \end{pmatrix} \tag{2.30}$$

We first try to find the $f_{j'}^{m'}$ considering that the expansion goes only up to order 4 ($j' \leq 4$).

For $j' = 0$ and $m' = 0$ we have

$$f_{00} - 2\sqrt{\pi} log(Z) + 2n\lambda^2 \int d\hat{\omega}' \frac{e^{\sum_{j=0}^{\infty}\sum_{m=-j}^{m=j} f_{jm}Y_{jm}(\hat{\omega}')}}{Z} c_0\sqrt{4\pi} = \frac{\beta\mu}{N} 2\sqrt{\pi},$$

which, upon using the normalization condition, reduces to:

$$f_{00} - log(Z) + 2n\lambda^2 c_0 = \frac{\beta\mu}{N}$$

for $j' = 2$:

$$f_{2m'} + 2n\lambda^2 \int d\hat{\omega}' \frac{e^{\sum_{j=0}^{\infty}\sum_{m=-j}^{m=j} f_{jm}Y_{jm}(\hat{\omega}')}}{Z} c_2 \frac{4\pi}{5} Y_{2m'}(\hat{\omega}') + \lambda^2 2\sqrt{\frac{\pi}{5}}\delta_{m'0} = 0$$

and for $j' = 4$:

$$f_{4m'} + 2n\lambda^2 \int d\hat{\omega}' \frac{e^{\sum_{j=0}^{\infty}\sum_{m=-j}^{m=j} f_{jm}Y_{jm}(\hat{\omega}')}}{Z} c_4 \frac{4\pi}{9} Y_{4m'}(\hat{\omega}') - \frac{\alpha^2\lambda^2}{2}\delta_{m'4}\sqrt{\frac{7\pi}{5}} = 0.$$

3

Circular confinement

We study the effect of closed curved walls on the organization of rigid rods by enclosing them in a cylindrical container with height much smaller than the length of the particles. Particles adopt a planar bipolar organization with the location of the pair of antipodal disclination points varying with density and aspect ratio of the particles. Upon changing the topology of the container by introducing a hole in the middle, the system switches from a bipolar structure to one stabilized by domain walls, the number of domains depending on the diameter of inner hole. Our results are in good agreement with experimental data of fd-viruses confined to micron-sized chambers.

3.1 Introduction

The typical shape of a cell is often rounded, creating a confining volume with non-planar walls [69]. The cytoskeletal filaments that are in the vicinity of the wall are forced to organize following its curvature. In the limit that the filaments are short compared to their persistence length, they behave like a rigid rod. For microtubules this is usually the case at the length scale of the cell, since their persistence length is of the order of millimeters [8] and the cell is only 10's of microns in diameter. For actin filaments, which have a persistence length of $\sim 17\mu m$ [14], the rigid rod approximation is only strictly valid when they are enclosed in a sub-cellular volume. An example of such a volume are cellular blebs. These spherical membrane protrusions of the order of microns in diameter enclose actin cortex [90]. Inside the blebs the actin filaments, even if they are crosslinked, do not seem to bend but are forced to arrange following the surface. Aligning of the cytoskeletal filaments to a curved surface is also relevant in the cytoplasm when these filaments have to grow around other cellular components like the nucleus, which is usually spherical, or the more complex shaped vacuoles. These components disrupt the bulk organization of the filaments creating a sort of defect.

Cytoskeletal filaments in the cytoplasm can be thought of as a fluid composed of rigid elongated particles, and their behavior is similar to a certain extent to a liquid crystal. To understand their organization when confined by curved walls it is useful to turn to liquid crystal physics. Liquid crystals confined to various curved geometries have been studied due to their many optical applications [91]. The best know example is the polymer-dispersed liquid crystal (PDLC) where spherical droplets containing nematic liquid crystals are dispersed in a rigid polymer matrix [92]. The organization of a nematic with planar anchoring in a droplet exhibits a bipolar structure with two disclination points of topological charge +1 at the surface [93]. For details about topological defects see section 1.4. In a PDLC the axes defined by the two disclination points in each droplet are overall isotropically distributed making the material opaque. If the polymer matrix and the nematic droplet have matching refractive indexes the material is then turned transparent upon applying an electric field which orients all the nematic droplets with their symmetry axis along the field. This phenomenon is now commercially used for electrically controllable light scattering windows [94]. The organization of a liquid crystal on the surface of a sphere is

characterized by four disclination points of charge $+1/2$ [95]. On a spherical shell, when the liquid crystal is confined in between two concentric spherical surfaces, the organization is characterized by two pairs of point disclinations of topological charge $+1$ located on the inner and outer surface, four $1/2$ defects on the outer surface or two $1/2$ and a $+1$ defect, the number of pairs varying with the thickness of the cortex [87, 96, 97]. Cylindrical confinement can be achieved by using membranes having cylindrical pores or carbon nanotube cavities and, for planar anchoring, a planar bipolar configuration and an escaped-twisted structure are found [98, 99]. The planar bipolar structure, which is characterized by two $+1/2$ defects, appears in 3D as a line of defects running parallel to the capillary wall. There are no experiments or theoretical work in the literature which deal with a liquid crystal confined in a tube-like geometry (between two cylindrical surfaces). This would be the uniaxial analogue of the spherical shell and we expect that interesting defect structures arise.

All the results mentioned above however are obtained in the regime that the mesogens are much smaller than the size of the confining volume. In this regime the details of individual particles are irrelevant, and the behavior of the liquid crystal is well described by a continuous field. When the particle size is only a few times smaller than the radius of cavity in which it is enclosed, we expect finite size effects to play a role leading to the emergence of new structures. Simulation of rigid rods confined in a disk have showed that, in addition to the expected bipolar structure, a metastable configuration with 3 disclination points of topological charge $+1/2$ on the surface and one of charge $-1/2$ in the center appears [82]. The development of photolithographic techniques allows fabrication of shallow disk-like boxes which can be as small as a few microns in diameter [42] and the use of fd-viruses, which are spherocylindrical and almost a micron in length, as mesogens[56] opens a new avenue for experimental investigation of ultraconfined liquid crystals in curved geometries. Here we use computer simulations to address the organization of anisotropic liquid crystalline particles with planar anchoring confined in container with dimensions only a few times larger than the length of the particles. First, we focus on a cylindrical geometry of the confining container, with the height of the container much smaller then the length of the particles. We look at how the two dimensional bipolar structure behaves if the system becomes three dimensional and also how this pattern is influenced by the density and the

asymmetry of the particles. By introducing an excluded area in the center of the container we look at how the system deals with a change in topology, by first considering an annulus-shaped planar system and then by adding a third dimension. We show that in this strong confinement regime novel equilibrium structures become accessible, which are the direct result of the finite size of the particles.

3.2 Simulation method

To investigate the organization of liquid crystalline particles confined to curved geometries we use a standard hard body Monte Carlo technique. The particle are represented by spherocylinders, with diameter D and length L, the diameter being used as unit length. We considered particles having an aspect ratio, L/D, of 15, 20 and 25. Each particle is characterized by the position of its center of mass $\mathbf{r}_i$ and its unit orientation vector $\mathbf{u}_i$. We confine the particles in a cylindrical box with the height of the cylinder L_z, smaller than its radius R and then the length of the particle (see figure 3.1(a)). For all our simulations we fixed $R = 40$ and choose $L_z = 1$, 3 or 6, the case $L_z = 1$ corresponding to the pure 2D system. For $L_z = 3$ and $L_z = 6$ the particle cannot fully rotate out of plane. The z-axis of the reference frame is taken along the symmetry axis of the cylinder. We change the topology of the system by inserting in the middle of our cylindrical container another cylinder with the same hight L_z as the initial one but with radius $R_{in} < R$, the symmetry axis of the two cylinders coinciding (see figure 3.1(b)). Particles are then not allowed to occupy the volume inside this inner cylinder. This insertion corresponds to creating a hole in the middle of the initial container, the base of the container now being a annulus. We performed simulations for various R_{in} ranging from 1 to 20, which corresponds to half the radius of the outer cylinder.

The Monte Carlo technique we use, also described in the previous chapter, involves trial rotations and translations of the particles. Since the interaction between particles and between a particle and the walls of the container are hard, such move is allowed if particles do not overlap with each other and they do not cross the wall. The overlap criteria between the wall and a shperocylindrical particle are presented in the Appendix 3.6 for both the simple cylindrical container and the annulus-based one.

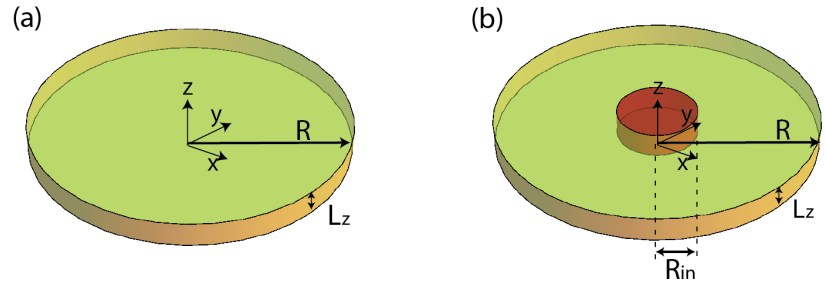

Figure 3.1: Sketch of the confining containers: (a) disk geometry and (b) annular geometry

To characterize the system we use a standard second rank tensor order parameter. This provides information on the equilibration of the system, but in order to study the patterns of the confined liquid crystal we need a spatially resolved version of the tensor order parameter. To construct this local version, we divide the container in small cuboid sub-volumes which have a square base located on the base of the confining container and the same height as the container (see figure 3.2 (a)). We define the local version of the tensor order parameter as:

$$\mathbf{Q}^k = \frac{1}{\sum_i l_i^k} \left\langle \sum_i l_i^k \left(\frac{3}{2} \hat{\mathbf{u}}_i \otimes \hat{\mathbf{u}}_i - \frac{1}{2} \mathbf{1}_3 \right) \right\rangle , \tag{3.1}$$

where the index i counts the particles and k the subvolumes. It often happens that the particles are shared between more subvolumes, crossing the separation walls, therefore in this averaging we need to account for the length l_i^k of particle that is actually enclosed in each subvolume (see figure 3.2(b)). The highest eigenvalue of the tensor order parameter gives the degree of order, ranging between 0 and 1, and the corresponding eigenvector the average direction of alignment $\hat{\mathbf{n}}$.

To characterize the defects we use an angular defect parameter δ, measuring the variation in the direction of alignment around a point. This parameter is defined as:

$$\delta = min\angle \left(\hat{\mathbf{n}}^1, \hat{\mathbf{n}}^2 \right) + min\angle \left(\hat{\mathbf{n}}^3, \hat{\mathbf{n}}^4 \right) , \tag{3.2}$$

where $\hat{\mathbf{n}}^j$ are orientations of neighboring sub volumes (for more details see previous chapter, section 2.2.4).

In the square confinement, the preferential directions of alignment are imposed by the geometry of the confining container. Due to the high symmetry in the circular geometry, there is no such preferential direction a priori. For example, in the case of a cylindrical box, all bipolar configurations are equivalent, regardless of the angle that the line defined by the two defects makes with the x-axis. In the course of a simulation the pattern therefore rotates around the symmetry axis of the confining box. We compute the degree of order and the average orientation not on the basis of a single configuration but as an average of independent configurations sampled throughout the simulation time. If we average over these configurations without accounting for the location of the defects, the patterns will be washed out. Averaging, for example, over bipolar configurations with the pair of antipodal defects homogeneously distributed around the box results in an overall isotropic-like configuration. To prevent this problem we come up with a strategy for locating the defects and then rotate the configurations in such way that the defects are located always at the same spot. Due to the rotational symmetry of the confining container, in both the disk and the annular geometry, along its center line, we expect the defect structures, if any, to be located radially. Therefore it is convenient to divide the container into into circular sectors (see figure 3.2 (c)). In each of these sectors we compute the average orientation of the particles $\mathbf{n}$. The minimum angle between the average orientation and the radial unit vector to the center of the circular sector $\mathbf{r}$ will run from 0 to $\pi/2$, with 0 corresponding to particles arranged radially and $\pi/2$ to particles aligned to the wall. A sharp drop in this minimum angle with respect to the polar angle of the confining container indicates the presence of a defect structure. As a example, for the 3-fold structure that we see by eye in the configuration shown in figure 3.2 (a) and (c), we observe, in panel (d) of the same figure, 3 sharp minima corresponding to the angles where the nematic-like domains meet. Extracting these local minima for each configuration, which correspond to the location of the defects, allow us to monitor the location of these defects over the course of the simulation (see figure 3.2 (e)). The three defect structures seem to move synchronously, the pattern rotating as a whole, in both directions, around the symmetry axis of the container. By taking the a single configuration as reference (for example the first one

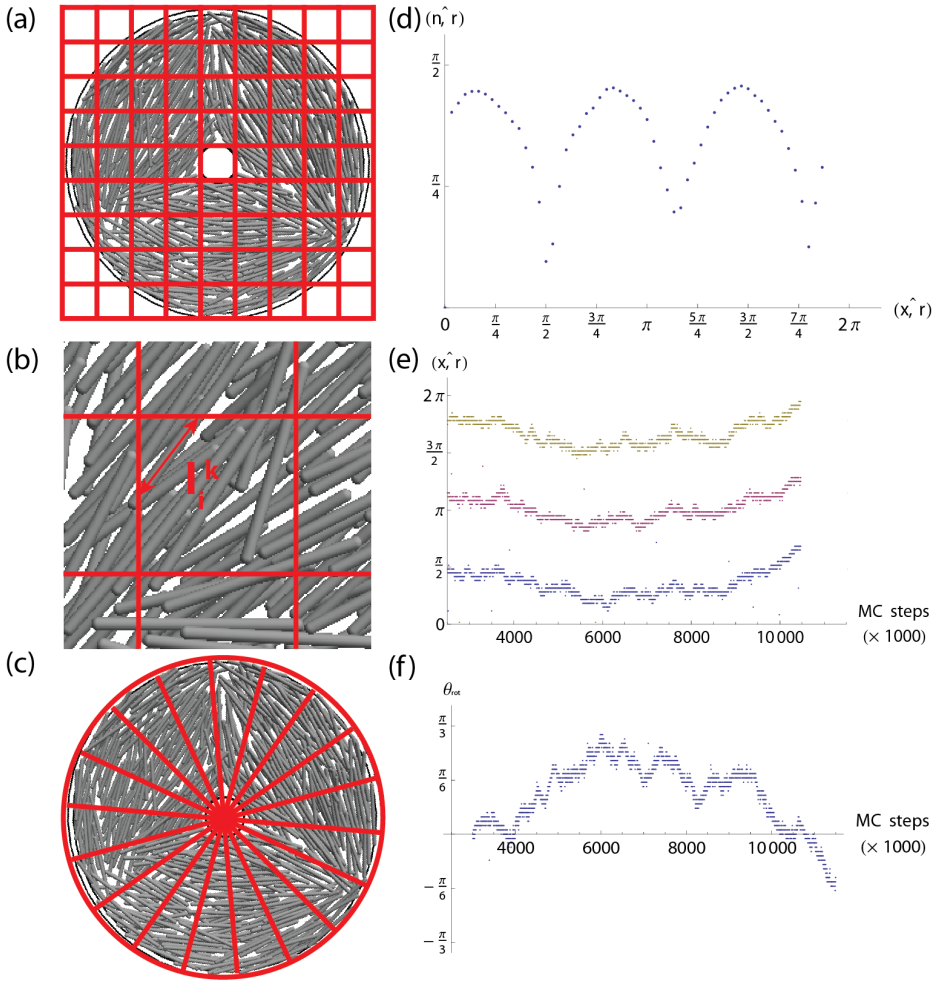

Figure 3.2: (a) Top view of the confining container divided into cuboid subvolumes (b) Top view of a subvolume (c)Top view of the confining container divided into circular sectors (d) Minimum angle between average orientation angle of the particles and the radial direction versus the polar angle of the confining container (e) Location of the defects, expressed in terms of the polar angle of the container, over the course of the simulation, from the equilibration point on (f) Rotation angle for each configuration

after we consider that the system has equilibrated) we compute the angle θ_m by which we need to rotate the other configurations we use in the averaging in order to obtain equivalent configurations, with the defects overlapping. This rotation angle is plotted in figure 3.2 (f) as function of the simulation time (expressed in Monte Carlo steps). After rotating the configurations we perform the averaging by using the division into cuboid subvolumes. We do not compute the tensor order parameter in the circular sector based subvolumes, but prefer the cuboid one, because, in the circular sectors we have no way of differentiating a point defect from a disinclination wall.

3.3 Disk geometry

In the disk geometry we observe four type of planar orientational patterns depending on packing fraction of the particles in the container (defined as $\eta = \rho V_{part}$, where $V_{part} = \pi D^2(1/4L + 1/6D)$ is the volume of the spherocylidrical particles and $\rho = N/V_{cont} = N/(\pi R^2 L_z)$ is the number density) and on their aspect ratio. We see a two types of bipolar structures: one where the two poles are located at a certain distance from the circular wall (B_I), the wall being coated with a nematic film, and one where the poles are situated at the wall (B_B). The two other patterns do not exhibit poles. The third pattern type (B_O) resembles a bipolar arrangement where the poles have been expelled from the container. The last type of pattern (B_∞) is characterized by a parallel arrangement of the particles, and can be considered the limit case when the defects have moved to infinity. Figure 3.3 illustrates the four types of patterns observed.

To characterize the patterns observed we perform averages over independent configurations sampled from the same simulation, extracting the local orientation and the degree of local order. We compute the disclination parameter from the angle between the local orientation and the x-axis of the reference frame, scaling it by π, which corresponds to its highest value. Results for the four representative types of organizations of spherocylindrical particles confined in cylindrical containers observed are presented in figure 3.4. We see that the pattern B_I, where the poles are located inside the container, exhibits a highly ordered region next to the wall where particles are arranged parallel to it. The order in the middle of the container is lower than next to the wall with two dips corresponding to the poles. The poles correspond to disclination points of topological charge $+1/2$, as

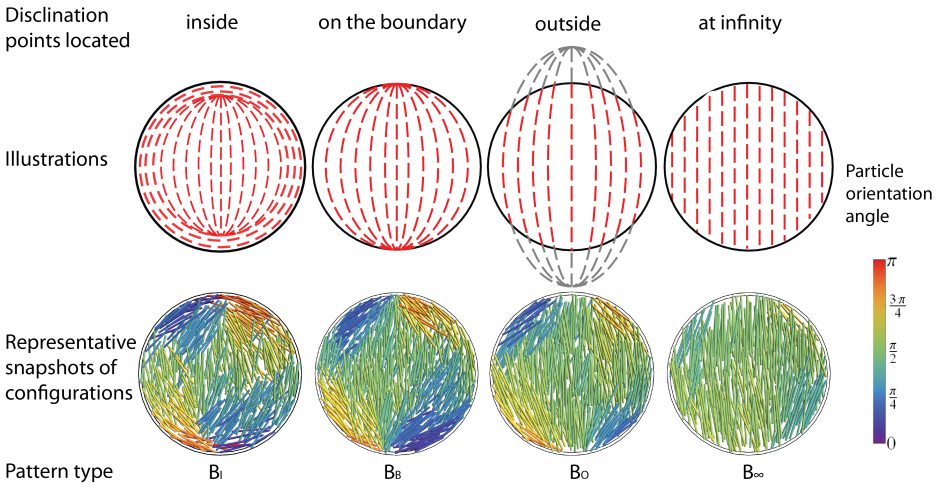

Figure 3.3: The four patterns observed in the disk geometry classified by the location of the disclination points (illustration-upper row and snapshot of representative configurations- lower row). For all the simulations shown in this figure the hight of the box was $L_z = 6$ and its radius $R = 40$. The packing fraction and the aspect ratio were (from left to right): (1) $L/D = 15$ and $\eta = 0.16$; (2) $L/D = 15$ and $\eta = 0.20$; (3) $L/D = 20$ and $\eta = 0.20$; (4) $L/D = 25$ and $\eta = 0.20$. The color of the particles is give by the angle between its orientation and the x-axis (scale bar on the right hand side).

can be seen from the disclination parameter which is almost 1. The pattern B_B, having poles located on the boundary, is highly ordered everywhere except at the poles. The orientation of the particles follows the bend lines connecting the pair of antipodal 1/2-disclination points. For the B_O type of organization the middle of the container contains a nematic phase, with particles highly aligned along a diameter of the container, acting as a symmetry axis. These virtual defects are the planar equivalent of the virtual boojums in the nematic droplets [85, 100]. Close to the wall we see a bend in the nematic director towards the symmetry axis. The organization looks similar to the pattern in the central region of the B_B type, therefore we can think of it as a bipolar structure with virtual poles located outside the container. The last pattern, B_∞, is a purely nematic arrangement entirely aligned along one diameter chosen randomly. For the last two types of or-

ganization the order decreases in the region where the nematic director is perpendicular to the wall. This effect is due to the particles occasionally being trapped between the wall and the nematic, which are aligned to the wall and hence perpendicular to the nematic.

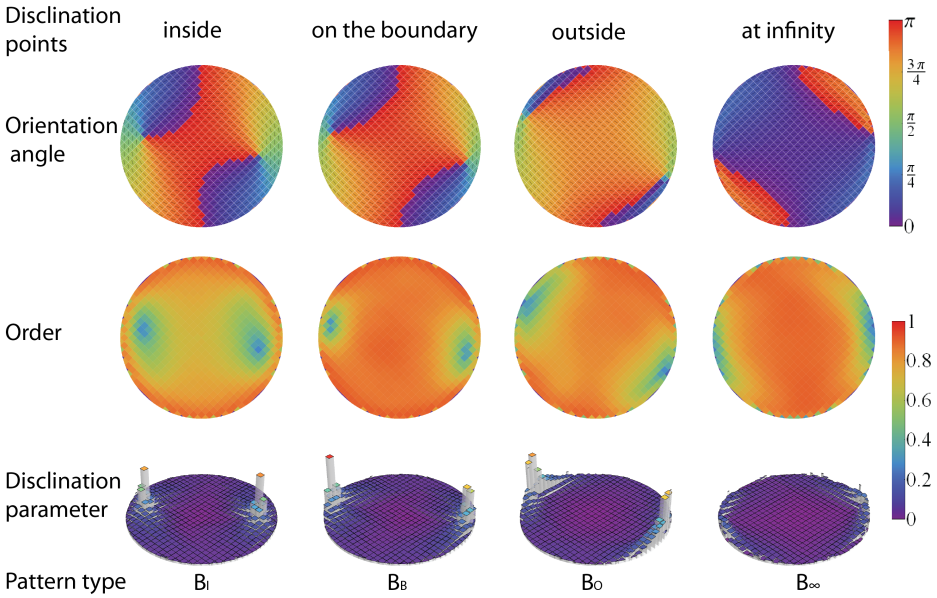

Figure 3.4: Local orientation of the particles (upper row), local order (middle row) and disclination parameter (lower row) corresponding to the four types of organization observed. The black lines show the orientation and the color corresponds to the angle between the orientation and the x-axis (scale bar on the right hand side). For both the order and the disinclination parameter, having values between 0 *an* 1*, the value is given by the color bar on the right hand side. The simulation parameters are the same as for the previous figure.*

The aspect ratio of the particles and the packing fraction influence the location of the defect points. By increasing the packing fraction, keeping all the other parameters constant, the location of the defects moves from inside the container to its boundary, then outside the container until the nematic director shows no sign of bending (see figure 3.5). The increase of particle aspect ratio also leads to movement to the defects outwards. The

thickness of the container does not seem to influence the location of the defects, the difference in patterns between containers with height $L_z = 3$ and $L_z = 6$ being present for only one set of parameters ($L/D = 20$ and $\eta = 0.16$) in the range considered. The packing fractions were chosen to be around the bulk isotropic-to-nematic transition, the values at coexistence being approximately $\eta_c = 0.22$ to $\eta_c = 0.25$ for $L/D = 15$, $\eta_c = 0.17$ to $\eta_c = 0.21$ for $L/D = 15$ and $\eta_c = 0.14$ to $\eta_c = 0.17$ for $L/D = 25$ [78]. We found that, in confinement, for the packing fractions for which in the bulk system would be in an isotropic phase, bipolar structures with defects inside as well as on the boundary of the container are already formed. The local degree of order in this phases is much higher than we expect for an isotopic phase, these patterns being highly aligned. Compared to the B_∞ pattern where we see no confinement effect on the liquid crystalline organization, the B_I and B_B patterns exhibit a distorted nematic phases. In the bulk coexistence region we see bipolar patterns with boundary disclination points and patterns characterized by virtual defects located outside the wall of the container. For all the values of the packing fraction that in bulk correspond to the nematic regime, we find parallel arrangement in confinement, the bulk liquid crystalline organization being unperturbed by the walls.

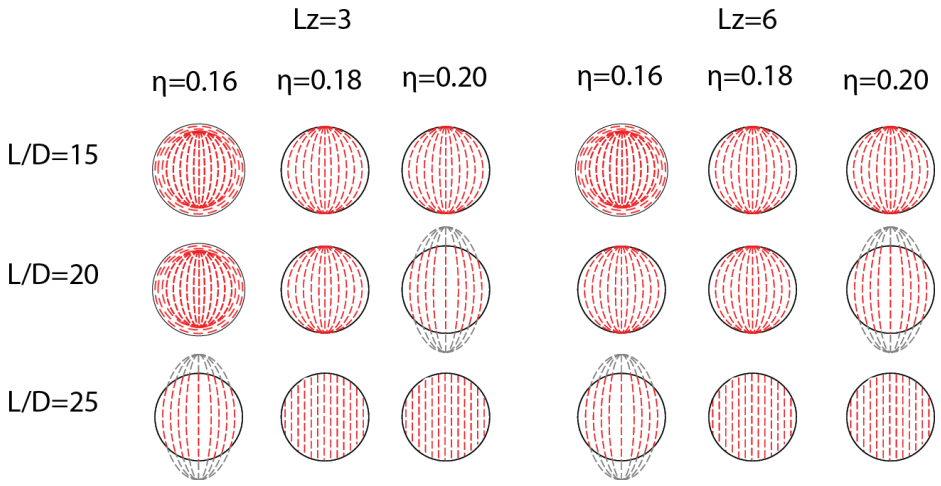

Figure 3.5: The organizational patters obtained as function of box hight (L_z), packing fraction (η) and aspect ratio (L/D) of the particles ($R = 40$).

The bipolar structure is the result of confinement and particle-particle interaction, of a competition between alignment to the wall and self-alignment of the particles. Next to a planar wall a liquid crystal with planar anchoring, even for packing fraction below the isotropic to nematic transition, aligns to it creating a nematic film of the order of one particle length in thickness coating the wall [64]. In our geometry, for lower packing fractions, a layer of particles is follows, with the wall the bipolar pattern being formed in the central region of the container. By increasing the packing fraction we strengthen the particle-particle alignment. This pushes the defects outwards until the particles are completely aligned to each other, a regime in which the confinement effect is unnoticeable. The movement of the defect points outwards with the increase in aspect ratio of the particles is due to the lowering of the bulk isotropic to nematic transition density with increasing aspect ratio. At the same packing fraction rods with higher aspect ratio have a higher tendency to align.

Similarly to the square slab-like geometry we presented in the previous chapter, the confinement lowers the packing fraction at which the isotropic to nematic transition occurs compared to the bulk. In figure 3.6 we show that the degree of local order in the center of the container is almost perfect at $\eta = 0.20$, whereas in the bulk at this packing fraction we still see an isotropic phase [78].

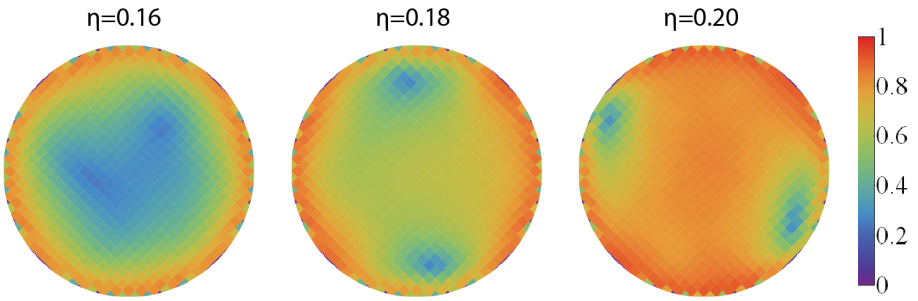

Figure 3.6: Evolution of the local order parameter as a function of packing fraction for $L_z = 3$, $R = 40$ and $L/D = 15$.

3.4 Annular geometry

The organization of a liquid crystal confined to a surface or enclosed in a cavity must follow the topological constrains of the confining geometry. The total topological charge of the defects in the liquid crystal should be equal to total topological charge of the surface of volume, since the topological charge of a vector field on a closed surface must be the same as the Euler characteristic of the surface (Poincare's theorem) [101, 102]. For a polyhedral surface, such as, for example a cube, the Euler characteristic χ can be calculated as:

$$\chi = V - E + F, \tag{3.3}$$

where, V is the number of vertexes, E the number of edges and F the number of facets. A cube has $\chi = 2$. The Euler characteristic of an arbitrary surface the can be found by polygonalizing the surface. A disk has Euler characteristic $\chi = 1$ and thus the total topological charge must be $+1$, which can be achieved, in the case of planar wall anchoring, by two $+1/2$ defects (bipolar structure) or a single $+1$ defect. This latter structure would correspond to particles arranged following concentric circles with the defect located in the center of the disk a particles, but is not observed experimentally due to the finite length of the mesogens. When we change the topology of the surface by opening a hole, we change its Euler characteristic and therefore the total topological charge. An annulus has Euler characteristic $\chi = 0$, which should correspond to a defect-free configuration. For planar wall anchoring, particles following concentric circles equally following the two boundary circles potentially offers a defect-free configuration. Another possibility to obtain a zero topological charge could be having pairs of plus and minus defects, but unless some other effects come in to play the number of defects is usually minimal, as they have a free-energy cost associated with them [103].

In order to study the effect of the change in topology of the confining container, we first turn to the two-dimensional case, by considering a container of $L_z = 1$. The packing fraction η is expressed in terms of the 3D container with unit height. This can be converted to the two dimensional equivalent area fraction using $\eta_{2D} = \eta\ (L + 2/3)/(1 + 4L/\pi)$. We start by opening a round hole in the middle of a disk, obtaining an annulus, taking the radius of the inner opening from $R_{in} = 1$ to $R_{in} = 20$, which represents up to half the outer radius of the container $R = 40$. Figure 3.7 presents the

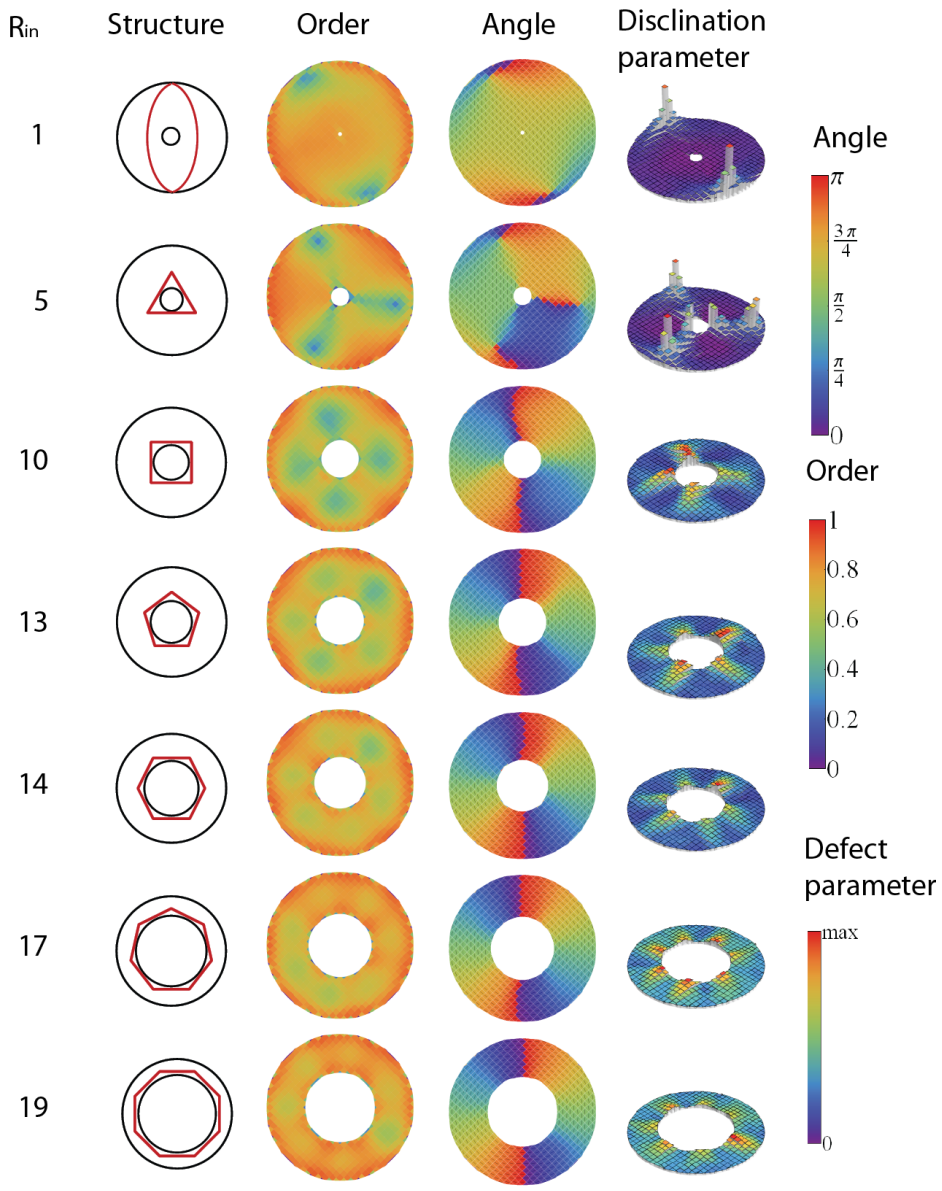

Figure 3.7: Representative organization in planar confinement ($L_z = 1$). For all the simulations particles had $L/D = 15$ and the packing fraction was $\eta = 0.40$.

representative patterns obtained. We observe that, for inner radius in the order of a few particle diameters, the bipolar structure characteristic to disk confinement is undisturbed. By increasing this radius further the system self-organizes in three equally-sized domains distributed around the inner hole. Inside the domains particles form a nematic phase. These domains are separated by a disclination line which is bordered by two point defects: a $+1/2$ located on the exterior wall on the container and a $-1/2$ positioned on the inner circular wall. The sum of the topological charges of the point disclination is zero, matching the Euler characteristic of the disk. Upon crossing the line separating the domains the orientation of the particles changes abruptly and the local order is low compared to the order in the middle of the domains. Increasing the inner radius even further leads to particle adopting a configuration characterized by four domains of equal sizes, forming a square around the hole. The separation between the domains is no longer a line both starting and ending in a disclination point as was the case of the three fold pattern but rather a the planar equivalent of a wall-like structure. This type of disclination is also characterized by a low local order and a variation in the particle orientation on either side separating structure. In the disclination parameter they appear as radial maxima, extending from the interior to the exterior wall. The four-fold symmetry changes to a five-fold, then to a six, seven and eight-fold pattern as a function of the radius of the inner opening. These higher symmetry organizations exhibit the same characteristics as the 4-fold one, the domains being separated similar structures.

By increasing the hight of the confining container to $L_z = 3$ and $L_z = 6$ we observe a similar behavior with the two dimensional system: as a function of inner radius increase we see the formation of planar structures equivalent to the ones in the annulus confinement ($L_z = 1$). For a small opening of up to $R_{in} = 2 - 3$, in a three dimensional case as well, the system seems unaffected by the presence of this defect, the pattern being the same as in the cylindrical confinement. For higher inner radii, a three-fold symmetrical pattern forms (see figure 3.8): three nematic domains separated by wall like structures. At the end of each separation wall there are disclination points with $-1/2$ (on the inner cylinder) and $+1/2$ (on the outer cylinder). The difference in particle orientation angle upon crossing the wall is $\approx \pi/3$. For higher inner radii of the inner cylinder the number of nematic domains increases. In figure 3.8 we show also example of a four

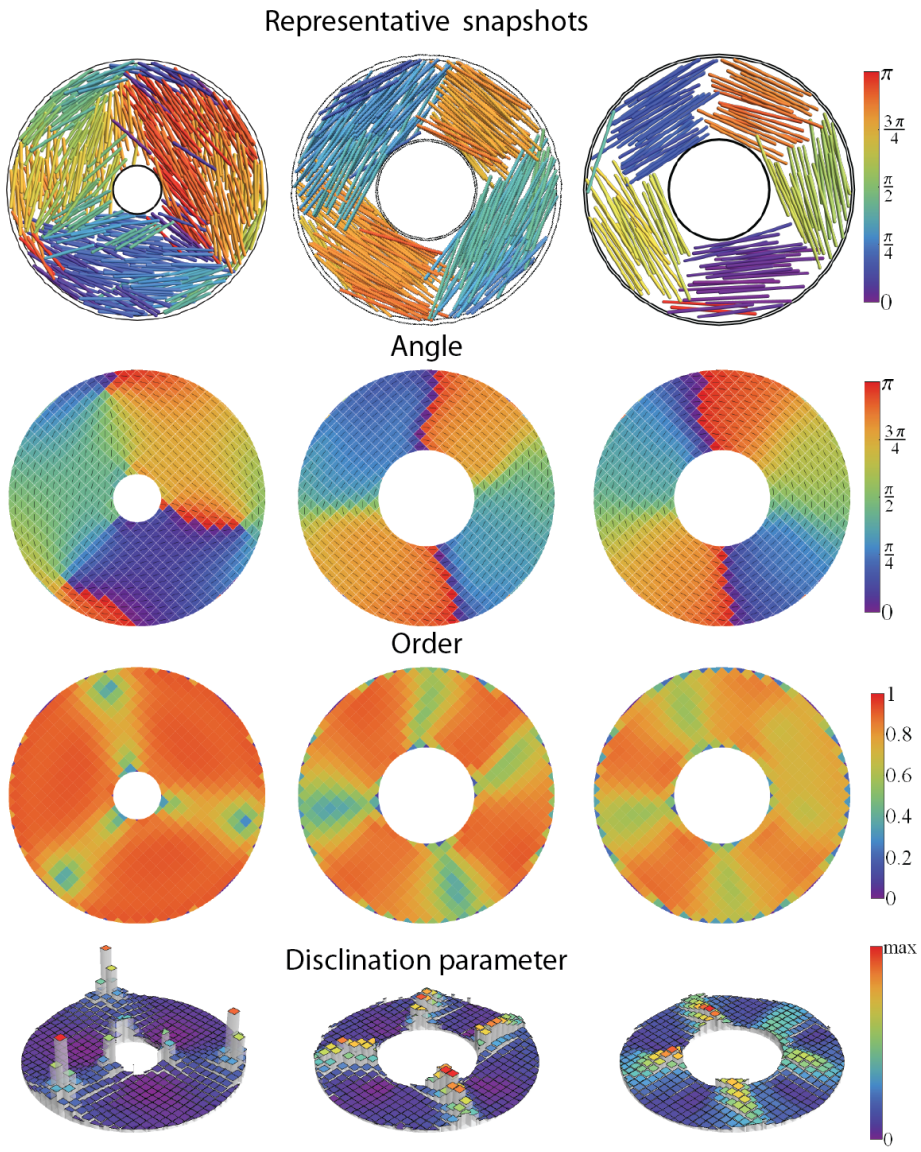

Figure 3.8: Representative types of organization in annular based containers characterized by 3-fold, 4-fold and 5-fold symmetry. Simulation parameters for each column (from left to right): (1) $L_z = 6$, $L/D = 15$, $\eta = 0.20$ and $R_{in} = 5$; (2) $L_z = 6$, $L/D = 25$, $\eta = 0.20$ and $R_{in} = 15$; (3) $L_z = 3$, $L/D = 25$, $\eta = 0.20$ and $R_{in} = 15$.

and five-fold symmetrical patterns. As in the two dimensional case, the domains are separated by disclination walls with no point defects at the ends. The angular variation of the orientation upon crossing the wall is $\approx \pi/4$ for the pattern exhibiting four domains and $\approx \pi/5$ for the one with for domains. All the disclinations appear more pronounced in the three dimensional containers due to the increased number of particles in each subvolume that we use for computing the local orientation and order. The disclination points appearing at the at the end of the wall in the 3-fold pattern result from particles being able to fit radially in the container. As the inner cylinder's radius increases this is no longer possible and, therefore, we do not see them in the higher-fold patterns.

In the annular geometry the excluded area in the middle of the container leads to the formation of nematic domains stabilized by wall disclinations. The particles try to follow both circular walls but, due to the length of the particles being comparable to the container size, this becomes more of a discrete packing problem than a continuum one. The number of domains seems to be imposed by the radius of the inner cylinder which also has a higher curvature then the outer one. We can therefore construct a simple geometrical argument. For a given particle length L we can construct a triangle, a square, a pentagon or in general any n-gon with sides equal to the particle length. The radius of the circle inscribed in this n-gon is given by:

$$R_{in} = \frac{L}{2\tan(\pi/n)}. \tag{3.4}$$

The rod packing around this circle is optimal and outer rods could just follow the direction given by these central ones. We checked, for rods of aspect ratio $L/D = 15$ the correspondence of this geometrical relation (see figure 3.9). For the two dimensional case the correspondence is is almost perfect. For the three dimensional case ($L_z = 3$ *and* 6) the number of domains is lower than the value predicted by the above relation and becomes lower with increasing container height.

3.5 Conclusion

Using Monte Carlo simulations we investigated the organization of rigid rods confined in curved wall containers. In the disk geometry we observed

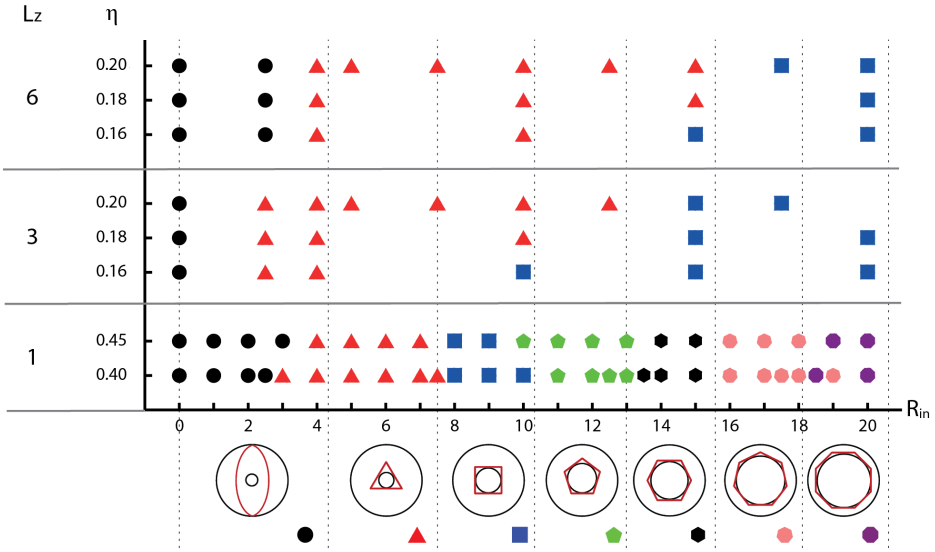

Figure 3.9: Number of domains observed as a function of inner radius R_{in} ($L/D = 15$ and $R = 40$). The vertical dotted delimit the R_{in} intervals in which we expect to find the number of domains shown in the illustrations bellow determined according to the relation 3.4. The symbols next to each illustration are used to show the number of domains observed in each simulation.

bipolar patterns with the disclination points moving from the interior to the exterior of the container with density increase. The location of the disclination points is imposed by the competition between wall alignment and particle mutual alignment. In the annular geometry we find that, above a critical diameter of the inner hole, the system switches from the bipolar organization featured in the disk geometry to a pattern characterized by three domains separated by disclination walls. By increasing the inner cylinder diameter we see an increase in the domain numbers up to eight. The patterns are a result of the finite size of the particles, and by a simple geometrical argument, we can relate the number of possible domains to the radius of the inner cylinder.

Our simulation results match preliminary results of experiments of fd-viruses confined in microchambers [104]. In the disk geometry bipolar patterns were with observed as well as undisturbed nematic (B_∞ pattern). In

the annular geometry, the bipolar and the 3-fold symmetric pattern appear. Additionally, an infinite symmetric pattern occurs predicted by mean field theory is observed in the in the limit that the annulus becomes very thin ($R_{in}/R \approx 0.7$). This results are in reasonable good agreement with our simulations considering the condition of the experiments are different: fd-virus have an aspect ration of ~ 130 and the confining containers had from 10 up to 100 particle length in diameter. We found no evidence, in neither the simulations nor in the experiments, of a 3-fold symmetric pattern in the disk geometry that [82] reports as metastable. The opening of the hole which changes the topology of the container is essential for the formation of disclination walls.

3.6 Appendix: Overlap criteria

3.6.1 Disk geometry

Let us consider a spherocylinder with length L and diameter $D = 2r$. The coordinates of its center of mass are given by $\mathbf{r} = (r_x, r_y, r_z)$ and its orientation by the unit vector $\mathbf{u} = (u_x, u_y, u_y)$. We want to determine if the spherocylinder is fully located inside the confining cylindrical container with radius R and hight L_z. The symmetry axis of the cylinder coincides with the z-axis and one of the disks that caps it is located in the xOy plane (see figure 3.10). Since a spherocylinder has the property that all the points on its surface are located at one radius distance from its center line the overlap criteria amount to determining whether this central line is located further than one radius from any wall. If the central line of the spherocylinder is closer than one radius from any wall then it overlaps with the container. the problem can be simplified even further: the container has a convex geometry therefore if the two ends of the spherocylinder are inside, the whole object will be inside.

It is convenient to decouple the problem in two components: one dealing with the overlap with the disk caps and one dealing with the circular wall. For a spherocylinder, the projection of one end of the cylinder's center line on our Cartesian coordinate system is:

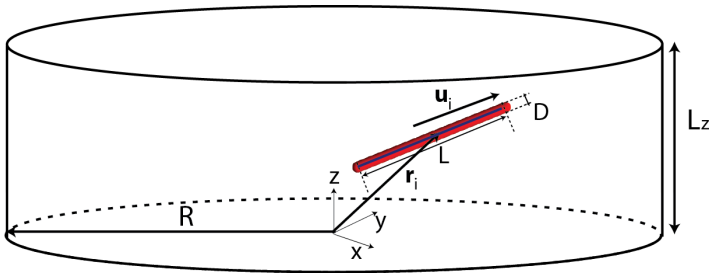

Figure 3.10: Illustration of a spherocylinder enclosed in a cylindrical container with the relevant geometrical parameters.

$$\begin{aligned} pr_{x1} &= r_x + \frac{L}{2}u_x, \\ pr_{y1} &= r_y + \frac{L}{2}u_y, \\ pr_{z1} &= r_z + \frac{L}{2}u_z, \end{aligned} \tag{3.5}$$

and for the other end we have:

$$\begin{aligned} pr_{x2} &= r_x - \frac{L}{2}u_x, \\ pr_{y2} &= r_y - \frac{L}{2}u_y, \\ pr_{z2} &= r_z - \frac{L}{2}u_z. \end{aligned} \tag{3.6}$$

The non-overlap condition with the end-disks is simply given by both z-projections of the two ends of the spherocylinder being further inside the cylinder than r from this two disks (which are located at $z = 0$ and $z = L_z$). For circular wall it is enough to check that,in the xOy plane, the two ends of the spherocylinder are inside a circle with radius $R - r$ (see figure 3.11).

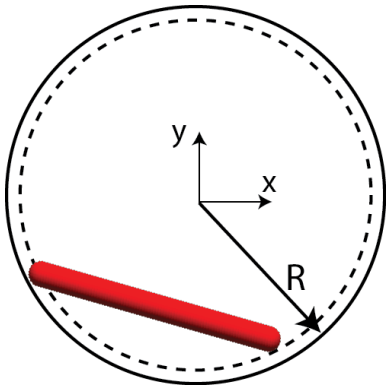

Figure 3.11: Top view of the cylindrical box. The dashed circle has radius $R - r$ and encloses the area in the xOy plane that the end-points of the center line of the spherocylinder are allow to occupy in order not to overlap with the container.

Mathematically, the above conditions can be written as follows:

$$\begin{aligned} r < pr_{z1} < L_z - r, \\ r < pr_{z2} < L_z - r, \\ pr_{x1}^2 + pr_{y1}^2 < (R - r)^2, \\ pr_{x2}^2 + pr_{y2}^2 < (R - r)^2. \end{aligned} \tag{3.7}$$

Thus, a spherocylinder will be inside our cylindrical container if all these inequalities are satisfied.

3.6.2 Annular geometry

If inside the cylindrical container we insert another cylindrical object with the same high L_z and the same symmetry axis as the initial cylinder, we obtain a tube-like volume having an annulus as base. The inner cylinder has radius R_{in} (see figure 3.12). Particles are not allowed to overlap with this inner cylinder.

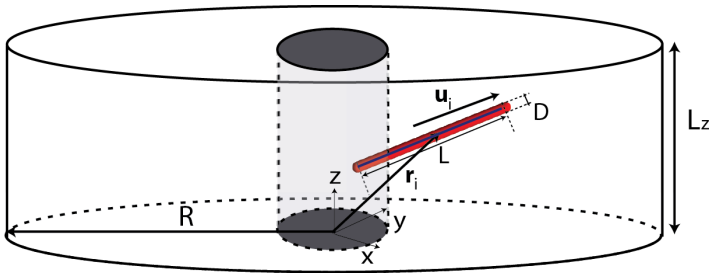

Figure 3.12: Illustration of a spherocylinder enclosed in a container with annular geometry.

In order to determine if a spherocylinder is enclosed in such container, without overlapping with any of the wall, the set of inequalities (3.7) for the overlap with the outer walls must be obeyed. Additionally, the central line of the spherocylinder must be outside the inner cylinder at at least one radius r distance from it. The area in the xOy plane that the two ends of the central line of the spherocylinder are now allowed to occupy is bounder by two circles: one of radius $R - r$ and one of radius $R_{in} + r$ (see figure 3.13). The two end of the central line of the spherocylinder are outside the inner cylinder if the following inequalities are satisfied:

$$\begin{aligned} pr_{x1}^2 + pr_{y1}^2 &> (R_{in} + r)^2 \\ pr_{x2}^2 + pr_{y2}^2 &> (R_{in} + r)^2. \end{aligned} \tag{3.8}$$

These conditions are necessary, but not sufficient, to determine the overlap. The two ends can be outside the inner cylinder but the body of the spherocylinder can still go through the walls. Therefore we need to check if the distance between the center line and the inner wall is higher than one radius r. This problem is equivalent with determining if the support line of the central line is further than $R_{in} + r$ from the center of the container.

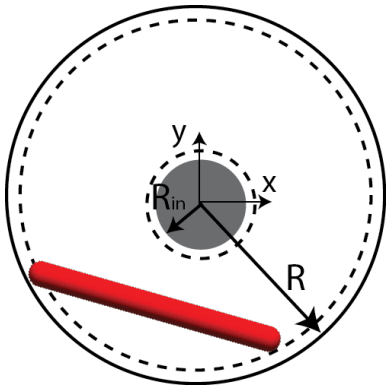

Figure 3.13: Top view of the annular container. The area between the dashed circles (of radius $R_{in}+r$- the inner one and $R-r$-the outer one) can be occupied by the end of the central line of the spherocylinder.

This distance is given by:

$$d = \frac{|r_y u_x - r_x u_y|}{\sqrt{u_x^2 + u_y^2}}, \tag{3.9}$$

and if $d^2 > (R_{in}+r)^2$ there is no overlap. When $d^2 < (R_1+r)^2$ we may have an overlap. This overlap only happens when the particle has both ends in the box and but it completely crosses the inner cylinder. If a particle is, for example, radially arranged in the box with both ends inside the container, the distance $d = 0$ but there is no overlap. Therefore we need to check if the intersection point of the perpendicular from the center of the container to the support central line of the the spherocylinder is actually part of line segment or only of the central line. This intersection point reads:

$$(x_D, y_D) = \left(\frac{u_y(r_x u_y - r_y u_x)}{u_x^2 + u_y^2} \, , \, \frac{u_x(r_y u_x - r_x u_y)}{u_x^2 + u_y^2} \right). \tag{3.10}$$

and the the parametric equation of the segment of the central line as:

$$(x, y) = \left(r_x + \frac{L}{2} u_x - t l u_x, r_y + \frac{L}{2} u_y - t l u_y \right). \tag{3.11}$$

where $t \in [0, 1]$. Equating the above two relations we obtain:

$$t = \frac{r_x u_x + r_y u_y}{L(u_x^2 + u_y^2)} + \frac{1}{2} \tag{3.12}$$

If $0 < t < 1$ than a part of the particle is inside the cylinder in the center of the box, this being not allowed.

4

Rectangular confinement: a mean-field theory approach

When mesogens are much smaller then the distance over which the nematic field strength is expected to vary, liquid crystals are well described by continuum theories. We design a novel microscopic mean-field theory in terms of both the scalar order parameter and the nematic director, which combines the virtues of the classical Oseen-Frank elastic theory with the ability of allowing the magnitude of the local order to vary of the Landau-de Gennes theory. By including a wall coupling term, we apply this theory to a nematic enclosed in a 2D rectangular container, with a tunable interaction with walls. In the regime where wall alignment competes with the mutual alignment of the particles, smooth patterns, displaying only continuous splay- and bend-type distortions of the nematic field are preferred, but structures exhibiting one or two disclination points are also observable, but have significantly higher free energy than the defect-free state.

4.1 Introduction

The size of the liquid crystalline particles relative to the length over which their preferred orientation varies plays an important role in deciding which approach is more suited to model the system. In confinement, the size of the container imposes the length scale at which variation in particle orientation occurs. In the previous two chapters we studied the regime where the length of the particles was only a few times smaller than the size the confining container. Each container wall imposes a preferential direction of alignment, and the enclosed nematic liquid crystal is forced to organize accommodating these orientations imposed by the wall. The mismatch between the competing directions of alignment makes particles change orientation over small distances, the nematic director varying drastically over a few particle lengths. At this length scale the details of the individual particles are important, and the disclinations observed are clearly a finite size effect. In this regime hard body Monte Carlo simulations are an effective tool to address the confined nematic organization.

Although cytoskeletal polymers in cells can grow to a length comparable to the cellular diameter [69], they are subject to dynamical polymerization processes, involving among others de novo nucleation, growth and shrinkage, and even severing. For microtubules these dynamical processes result in an exponential steady-state length distribution in bulk [105], with a maximum length imposed by the cell boundary in confinement [106]. For actin filaments, the length distribution, measured *in vitro*, is exponential as well [107]. Hence the majority of these polymers are relatively short, only a small fraction of them reaching lengths comparable to the cell size. Thus, understanding confinement at a scale where particles are much smaller then the confining volume is also a relevant problem. E.g. it has been suggested that in assays involving strongly length-polydisperse actin filaments confined to microchambers, the short filaments could act as depletion agents with respect to the longer ones, possibly leading to the observed bundling of the longer filaments [42].

However, in the case where the mesogens are much smaller than the container in which they are enclosed, the Monte Carlo simulation technique becomes time-inefficient due to the large number of particles involved. For this regime we expect that the nematic director will change orientation over distances much larger than the particle size, and the behavior a the nematic liquid crystal is then well captured by continuum theories[55], in which the

system is described by the average orientation of the particles and the local amount of order.

The simplest continuum theory is due to Oseen [108] and Frank[109].This elastic theory is formulated in therm of the nematic director $\mathbf{n}$. The nematic organization is given by global minima of the elastic free energy, $E[\mathbf{n}]$, which takes the form:

$$\begin{aligned} E[\mathbf{n}] &= \frac{1}{2}\int\int\int_V (K_1(\nabla\cdot\mathbf{n})^2 + K_2(\mathbf{n}\cdot\nabla\times\mathbf{n})^2 r \\ &\quad + K_3(\mathbf{n}\times\nabla\times\mathbf{n})^2)\, dV, \end{aligned} \tag{4.1}$$

where $K1$, $K2$ and, $K3$ correspond to so-called splay, twist and bend distortions respectively. This free energy is subject to boundary conditions, e.g. for a confined liquid crystal with planar anchoring to the wall the nematic director is fixed to be tangent to the wall.

However, this elegant formalism has a few shortcomings. The theory itself is formulated only in terms of the nematic director and thus consider the scalar order parameter to be constant. This excludes e.g. the presence of disclinations, and the only kind of changes in the nematic field that it can account for are continuous distortions such as bends or splays. Furthermore, it considers only strong anchoring to the wall. One also expects that for a weaker coupling to the wall, the system could trade off anchoring energy in order to relax elastic distortions in the bulk.

Another well-known continuum theory is the phenomenological Landau-De Gennes theory of liquid-crystalline phase transitions. This theory is based on the generic Landau theory [110] of phase transitions. The Landau theory is written in terms of an parameter η which characterizes the symmetry of phase order the system. In the less ordered phase $\eta = 0$, this typically occurring at a high temperature T. As the system cools down the order parameter increases, the system being more ordered. Near the transition from the disordered to the ordered state, the orderparameter η is small, making it possible to express the thermodynamic potentials as a low-order expansion in the order parameter as:

$$G(T,\eta) = G(T,0) + \alpha\eta + \frac{1}{2}A\eta^2 + \frac{1}{3}B\eta^3 + \frac{1}{4}C\eta^4 + ..., \tag{4.2}$$

where α, A, B and C are functions of temperature. P.G. de Gennes showed that the free energy density of an uniaxial nematic can be written as as a

expansion up to 4-th order in components of second-rank tensorial order parameter **Q** as:

$$f = f_i + AQ_{\alpha\beta}Q_{\beta\alpha} - \frac{1}{3}BQ_{\alpha\beta}Q_{\beta\gamma}Q_{\gamma\alpha} + \frac{1}{4}C(Q_{\alpha\beta}Q_{\beta\alpha})^2 \qquad (4.3)$$

where f_i is the free energy density of the isotropic phase and A, B and C are temperature dependent [111]. The order parameter tensor **Q**, which is fully charcterized by being real, symmetric and traceless, contains information about both the degree of order and the direction of alignment. While this theory now explicitly allows for singularities, where the magnitude of the ordering vanishes, it still suffers from the defect that the magnitude of the ordering is not strictly bounded from above, as it does not correctly account for the non-linearities beyond the vicinitity of the phase transition.

Therefore, we set out to formulate a *microscopic* mean-field theory which nevertheless is specified completely in terms of the *macroscopic* tensor order parameter. The new theory should keep the virtues of the Landau-De Gennes formalism, allowing for both the nematic director and the order parameter to vary, and thus making possible the emergence of disclinations. However, since it is derived it from microscopic theory, our theory is consistent for all values of the order parameter. The theory is constructed in arbitrary dimensions and is later particularized to 2D systems, since we apply it to a nematic confined to a shallow rectangular well. If the depth of the well is smaller then the particle length, precluding out of plane rotation, we expect that the the organization of the nematic it encloses is also planar. Considering the system to be homogeneous over the depth of the well, leads us to explore the equivalent planar problem. The wall coupling is introduced by adding an wall anchoring term to the free energy. We find that the minimum energy configurations, for the regime where the anchoring energy competes with the elastic contributions, are the same as the ones predicted by the Oseen-Frank theory, but patterns with one or two disclination points are also stable. Patterns exhibiting disclination points have been observed in experiments on fd-viruses confined in shallow rectangular wells. When the elastic contribution dominates the anchoring effects the nematic aligns along the longest wall, which has also been observed experimentally.

4.2 Definition

The goal is to create a *microscopic* theory for a nematic liquid crystal that has as its its fundamental degrees of freedom a quantity directly identifiable as the *macroscopic* order parameter $\mathbf{Q}$. We introduce a mean-field density-functional

$$\beta F[\rho^{(1)}] = \int d\mathbf{r} d\hat{\omega} \rho^{(1)}(\mathbf{r},\hat{\omega}) \left\{ \log \mathcal{V}_T \rho^{(1)}(\mathbf{r},\hat{\omega}) - 1 \right\} + \frac{1}{2} \int d\mathbf{r}_1 d\hat{\omega}_1 \int d\mathbf{r}_2 d\hat{\omega}_2 \rho^{(1)}(\mathbf{r}_1,\hat{\omega}_1)\rho^{(1)}(\mathbf{r}_2,\hat{\omega}_2) W(\mathbf{r}_1,\hat{\omega}_1;\mathbf{r}_2,\hat{\omega}_2) \quad (4.4)$$

We choose the interparticle interaction (which is expressed in units of $k_B T$), to be the simplest one expressible as a quadratic in terms of the microscopic "anistropic polarizability" tensor. In three dimensions this tensor has the form:

$$\mathbf{q}(\hat{\omega}) = \frac{1}{2}(3\hat{\omega} \otimes \hat{\omega} - \mathbb{I}), \quad (4.5)$$

with $\hat{\omega} = (\cos\theta \sin\phi, \sin\theta \sin\phi, \cos\phi)$, whereas in 2D it reads:

$$\mathbf{q}(\hat{\omega}) = (2\hat{\omega} \otimes \hat{\omega} - \mathbb{I}), \quad (4.6)$$

with $\hat{\omega} = (\cos\theta, \sin\theta)$. Hree θ denotes the polar angle, ϕ the azimuthal one and $\mathbb{I}$ the unit matrix of size 3 or 2 respectively. This leads to

$$W(\mathbf{r}_1,\hat{\omega}_1;\mathbf{r}_2,\hat{\omega}_2) = \mathbf{W^{(0)}}(\mathbf{r}_1 - \mathbf{r}_2) + \mathbf{q}(\hat{\omega}_1) : \mathbf{W^{(2)}}(\mathbf{r}_1 - \mathbf{r}_2) + \mathbf{W^{(2)}}(\mathbf{r}_1 - \mathbf{r}_2) : \mathbf{q}(\hat{\omega}_2) + \mathbf{q}(\hat{\omega}_1) : \mathbf{W^{(4)}}(\mathbf{r}_1 - \mathbf{r}_2) : \mathbf{q}(\hat{\omega}_2) \quad (4.7)$$

where the general form of the tensors $\mathbf{W}^{(k)}$ is given by

$$\begin{aligned} W^{(0)}(\mathbf{s}) &= w^{(0)}(s) \quad (4.8)\\ W^{(2)}_{\mu\nu}(\mathbf{s}) &= w^{(2)}(s)\hat{\mathbf{s}}_\mu \hat{\mathbf{s}}_\nu \\ W^{(4)}_{\mu\nu\sigma\tau}(\mathbf{s}) &= w^{(4)}_0(s)(\delta_{\mu\sigma}\delta_{\nu\tau} + \delta_{\mu\tau}\delta_{\nu\sigma}) + \\ &\quad w^{(4)}_2(s)(\hat{\mathbf{s}}_\mu\delta_{\nu\sigma}\hat{\mathbf{s}}_\tau + \hat{\mathbf{s}}_\nu\delta_{\mu\sigma}\hat{\mathbf{s}}_\tau + \hat{\mathbf{s}}_\mu\delta_{\nu\tau}\hat{\mathbf{s}}_\sigma + \hat{\mathbf{s}}_\nu\delta_{\mu\tau}\hat{\mathbf{s}}_\sigma) + \\ &\quad w^{(4)}_4(s)\hat{\mathbf{s}}_\mu\hat{\mathbf{s}}_\nu\hat{\mathbf{s}}_\sigma\hat{\mathbf{s}}_\tau \end{aligned}$$

where we have used the shorthand notation notation $\mathbf{s} = s\hat{\mathbf{s}} = \mathbf{r} - \mathbf{r}'$ for the interparticle separation vector. The derivation of this effective interaction is discussed in the Appendix 4.10.1 of this chapter.

4.3 The reduced functional

We will confine ourselves to phases with a spatially homogeneous density distribution. We therefore introduce the local orientational distribution function $\psi(\mathbf{r}, \hat{\omega})$, which we will further abbreviate as ODF, through

$$\rho^{(1)}(\mathbf{r}, \hat{\omega}) = \rho\psi(\mathbf{r}, \hat{\omega}), \tag{4.9}$$

with the constant number density $\rho = N/V$, where N is the number of particles and V the volume of the system. The free energy as a functional of the ODF then reads

$$\begin{aligned}\beta F[\psi] = N \log \nu_T \rho + \frac{1}{2}\Omega_d N \rho \overline{w^{(0)}} + \rho \int d\mathbf{r} d\hat{\omega} \psi(\mathbf{r}, \hat{\omega}) \log \psi(\mathbf{r}, \hat{\omega}) \\ + \frac{1}{2}\rho^2 \int d\mathbf{r} d\mathbf{r}' \mathbf{Q}(\mathbf{r}) : \mathbf{W}^{(4)}(\mathbf{r} - \mathbf{r}') : \mathbf{Q}(\mathbf{r}')\end{aligned} \tag{4.10}$$

where Ω_d is the area of the unit ball of dimension d, and the overbar denotes radial averaging, i.e.

$$\overline{f} = \int_0^\infty dr\ r^{d-1} f(r). \tag{4.11}$$

The local order parameter tensor is defined as

$$\mathbf{Q}(\mathbf{r}) = \int d\hat{\omega} \mathbf{q}(\hat{\omega}) \psi(\mathbf{r}, \hat{\omega}). \tag{4.12}$$

Note that in the case of phases with a spatially homogeneous density distribution the coupling of the individual particle orientations to the interparticle separation vector, as described by the $\mathbf{W}^{(2)}$ terms in the interaction, does not play a role.

To obtain the free energy as a functional of the local order parameter tensor only, we perform a constrained minimization keeping the value of the local order parameter fixed through a lagarange multiplier field that can also be interpreted as an external field. The idea is that the intrinsic free energy of system in an equilibrium with an external field that causes a certain deviation from the field-free equilibrium ODF can be interpreted as the non-equlibrium free energy of the distorted state. This procedure which has been reinvented in the literature under various names and guises,

is an expression of the central tenet of density functional theory viz. the one-to-one correspondence between external field and equilibrium densities. As the average energy in our toy model already depends only on $\mathbf{Q}$ we can simply maximize the entropy, i.e. we consider the following stationarity condition

$$\frac{\delta}{\delta\psi(\mathbf{r},\hat{\omega})}\left\{\rho\int d\mathbf{r}d\hat{\omega}\psi(\mathbf{r},\hat{\omega})\log\psi(\mathbf{r},\hat{\omega})+\int d\mathbf{r}\mu(\mathbf{r})\left\{1-\int d\hat{\omega}\psi(\mathbf{r},\hat{\omega})\right\}-\rho\int d\mathbf{r}\mathbf{\Lambda}(\mathbf{r}):\left\{\mathbf{Q}(\mathbf{r})-\int d\hat{\omega}\mathbf{q}(\hat{\omega})\psi(\mathbf{r},\hat{\omega})\right\}\right\}=0 \quad (4.13)$$

Performing the variation and eliminating the field $\mu(\mathbf{r})$ which takes of the normalization of the ODF we get

$$\psi(\mathbf{r},\hat{\omega})=\frac{\exp\{-\mathbf{\Lambda}(\mathbf{r}):\mathbf{q}(\hat{\omega})\}}{\zeta(\mathbf{r})} \quad (4.14)$$

where the normalization factor is given by

$$\zeta(\mathbf{r})=\int d\hat{\omega}\exp\{-\mathbf{\Lambda}(\mathbf{r}):\mathbf{q}(\hat{\omega})\} \quad (4.15)$$

The field $\mathbf{\Lambda}(\mathbf{r})$ now has to be chosen such that the constraint

$$\mathbf{Q}(\mathbf{r})=\int d\hat{\omega}\mathbf{q}(\hat{\omega})\frac{\exp\{-\mathbf{\Lambda}(\mathbf{r}):\mathbf{q}(\hat{\omega})\}}{\zeta(\mathbf{r})} \quad (4.16)$$

is satisfied. Let us denote the solution to this problem by $\mathbf{\Lambda}_{\mathbf{Q}}(\mathbf{r})$. The constrained free energy is then given by

$$\beta F[\mathbf{Q}]=-\rho\int d\mathbf{r}\log\zeta_{\mathbf{Q}}(\mathbf{r})-\rho\int d\mathbf{r}\mathbf{\Lambda}_{\mathbf{Q}}(\mathbf{r}):\mathbf{Q}(\mathbf{r})+\frac{1}{2}\int d\mathbf{r}d\mathbf{r}'\mathbf{Q}(\mathbf{r}):\mathbf{W}^{(4)}(\mathbf{r}-\mathbf{r}'):\mathbf{Q}(\mathbf{r}')+\beta F_0, \quad (4.17)$$

where $\beta F_0=N\log\nu_T\rho+\frac{1}{2}\Omega_d N\rho\overline{w^{(0)}}$. The non-constant terms of the above expression of the free energy do not depend on explicitly on dimensionality, taking the same form for both two and three dimensions. It is now easy to verify that varying this functional with respect to $\mathbf{Q}$ yields the usual

selfconsistency condition. Indeed,

$$\frac{\delta\beta F[\mathbf{Q}]}{\delta\mathbf{Q}(\mathbf{r})} = \rho\frac{\delta\mathbf{\Lambda}_{\mathbf{Q}}(\mathbf{r})}{\delta\mathbf{Q}(\mathbf{r})} : \left\{\int d\hat{\omega}\mathbf{q}(\hat{\omega})\frac{e^{-\mathbf{\Lambda}_{\mathbf{Q}}(\mathbf{r}):\mathbf{Q}(\mathbf{r})}}{\zeta_{\mathbf{Q}}(\mathbf{r})} - \mathbf{Q}(\mathbf{r})\right\} - \rho\left\{\mathbf{\Lambda}_{\mathbf{Q}}(\mathbf{r}) - \rho\int d\mathbf{r}'\mathbf{W}^{(4)}(\mathbf{r}-\mathbf{r}') : \mathbf{Q}(\mathbf{r}')\right\} = 0$$

The first term is zero due to the constraint condition, leaving the standard prescription for the equilibrium mean-field

$$\mathbf{\Lambda}_{\mathbf{Q}}(\mathbf{r}) = \rho\int d\mathbf{r}'\mathbf{W}^{(4)}(\mathbf{r}-\mathbf{r}') : \mathbf{Q}(\mathbf{r}') \tag{4.18}$$

which could also have been obtained by minimizing the finctional Eq. (4.10) directly with respect $\psi(\hat{\omega})$, showing that the constrained variation followed by a relaxation of the constraints yields the same result as expected.

4.4 Describing perturbations around the uniaxial equilibrium state

We are now going to look at the free energy cost of perturbations around the uniaxially aligned nematic equilibrium state. For simplicity we consider only perturbations that correspond to a local reorientation of the preferred frame. Thus

$$\mathbf{Q}(\mathbf{r}) = \Omega(\mathbf{r}) \cdot \mathbf{Q}^{(0)} \cdot \Omega^{-1}(\mathbf{r}) \tag{4.19}$$

where $\Omega(\mathbf{r})$ is a rotation matrix and $\mathbf{Q}^{(0)}$ the order parameter tensor for the homogeneous nematic state introduced in the previous section. We first note the first two terms in the free energy functional trivially remain

constant under such a local rotation. Consider

$$\begin{aligned}
\zeta(\mathbf{r}) &= \int d\hat{\omega} \exp\left\{-\mathbf{\Lambda}(\mathbf{r}) : \mathbf{q}(\hat{\omega})\right\} \\
&= \int d\hat{\omega} \exp\left\{-\Omega\left(\mathbf{r}\right) \cdot \mathbf{\Lambda}^{(0)} \cdot \Omega^{-1}\left(\mathbf{r}\right) : \mathbf{q}(\hat{\omega})\right\} \\
&= \int d\left\{\Omega^{-1}\left(\mathbf{r}\right) \cdot \hat{\omega}\right\} \exp\left\{-\Omega\left(\mathbf{r}\right) \cdot \mathbf{\Lambda}^{(0)} \cdot \Omega^{-1}\left(\mathbf{r}\right) : \Omega\left(\mathbf{r}\right) \cdot \mathbf{q}(\hat{\omega}) \cdot \Omega^{-1}\left(\mathbf{r}\right)\right\} \\
&= \int d\left\{\Omega^{-1}\left(\mathbf{r}\right) \cdot \hat{\omega}\right\} \exp\left\{-\mathbf{\Lambda}^{(0)} : \mathbf{q}(\hat{\omega})\right\} \\
&= \int d\hat{\omega} \exp\left\{-\mathbf{\Lambda}^{(0)} : \mathbf{q}(\hat{\omega})\right\} = \zeta^{(0)} \qquad (4.20)
\end{aligned}$$

so that

$$\begin{aligned}
\mathbf{Q}(\mathbf{r}) &= \int d\hat{\omega}\mathbf{q}(\hat{\omega}) \frac{\exp\left\{-\mathbf{\Lambda}(\mathbf{r}) : \mathbf{q}(\hat{\omega})\right\}}{\zeta(\mathbf{r})} \\
&= \int d\hat{\omega}\mathbf{q}(\hat{\omega}) \frac{\exp\left\{-\Omega\left(\mathbf{r}\right) \cdot \mathbf{\Lambda}^{(0)} \cdot \Omega^{-1}\left(\mathbf{r}\right) : \mathbf{q}(\hat{\omega})\right\}}{\zeta^{(0)}} \\
&= \int d\left\{\Omega^{-1}\left(\mathbf{r}\right) \cdot \hat{\omega}\right\} \Omega\left(\mathbf{r}\right) \cdot \mathbf{q}(\hat{\omega}) \cdot \Omega^{-1}\left(\mathbf{r}\right) \frac{\exp\left\{-\mathbf{\Lambda}^{(0)} : \mathbf{q}(\hat{\omega})\right\}}{\zeta^{(0)}} \\
&= \Omega\left(\mathbf{r}\right) \cdot \int d\hat{\omega}\mathbf{q}(\hat{\omega}) \frac{\exp\left\{-\mathbf{\Lambda}^{(0)} : \mathbf{q}(\hat{\omega})\right\}}{\zeta^{(0)}} \cdot \Omega^{-1}\left(\mathbf{r}\right) \\
&= \Omega\left(\mathbf{r}\right) \cdot \mathbf{Q}^{(0)} \cdot \Omega^{-1}\left(\mathbf{r}\right) \qquad (4.21)
\end{aligned}$$

so that we only need to consider the interaction term.

4.5 The effective interaction

4.5.1 The square gradient expansion

Consider

$$\begin{aligned}
&\int d\mathbf{r}d\mathbf{r}'\mathbf{Q}(\mathbf{r}) : \mathbf{W}^{(4)}(\mathbf{r} - \mathbf{r}') : \mathbf{Q}(\mathbf{r}') \\
&= \int d\mathbf{R}d\mathbf{s}\mathbf{Q}(\mathbf{R} + \frac{1}{2}\mathbf{s}) : \mathbf{W}^{(4)}(\mathbf{s}) : \mathbf{Q}(\mathbf{R} - \frac{1}{2}\mathbf{s}) \qquad (4.22)
\end{aligned}$$

where $\mathbf{R} = \frac{1}{2}\left(\mathbf{r} + \mathbf{r}'\right)$ is the center of mass coordinate and $\mathbf{s}$ the previously defined separation vector. As we are primarily interested in case where the

orientational distortions vary only slowly on the molecular scale, we can simplify the effective interaction (4.22) can further written by expanding $\mathbf{Q}$ in to second order in the derivatives as:

$$\int d\mathbf{R}d\mathbf{s}(\mathbf{Q}(\mathbf{R}) + \frac{1}{2}\nabla\mathbf{Q}(\mathbf{R})\cdot\mathbf{s}) : \mathbf{W}^{(4)}(\mathbf{s}) : (\mathbf{Q}(\mathbf{R}) - \frac{1}{2}\nabla\mathbf{Q}(\mathbf{R})\cdot\mathbf{s}). \quad (4.23)$$

We first evaluate the integral over the separation vector $\mathbf{s}$, dropping, for the moment, the dependence on the center of mass coordinate $\mathbf{R}$ and explicitly rewriting the contractions using Einstein's summation convention:

$$\int d\mathbf{s}(\mathbf{Q} + \frac{1}{2}\nabla\mathbf{Q}\cdot\mathbf{s}) : \mathbf{W}^{(4)}(\mathbf{s}) : (\mathbf{Q} - \frac{1}{2}\nabla\mathbf{Q}\cdot\mathbf{s}) =$$
$$= \int d\mathbf{s}(Q_{\mu\nu} + \frac{1}{2}\partial_\lambda Q_{\mu\nu}s_\lambda)W^{(4)}_{\mu\nu\tau\sigma}(\mathbf{s})(Q_{\tau\sigma} - \frac{1}{2}\partial_\beta Q_{\tau\sigma}s_\beta), \quad (4.24)$$

where

$$W^{(4)}_{\mu\nu\tau\sigma}(\mathbf{s}) = w^{(4)}_0(s)(\delta_{\mu\sigma}\delta_{\nu\tau} + \delta_{\mu\tau}\delta_{\nu\sigma}) + +w^{(4)}_2(s)(\hat{\mathbf{s}}_\mu\delta_{\nu\sigma}\hat{\mathbf{s}}_\tau$$
$$+\hat{\mathbf{s}}_\nu\delta_{\mu\sigma}\hat{\mathbf{s}}_\tau + \hat{\mathbf{s}}_\mu\delta_{\nu\tau}\hat{\mathbf{s}}_\sigma + \hat{\mathbf{s}}_\nu\delta_{\mu\tau}\hat{\mathbf{s}}_\sigma) + w^{(4)}_4(s)\hat{\mathbf{s}}_\mu\hat{\mathbf{s}}_\nu\hat{\mathbf{s}}_\sigma\hat{\mathbf{s}}_\tau. \quad (4.25)$$

The remaining integrals over the separation vector can be worked out analytically both in 2 dimensions as well as in 3 dimensions. The relevant details are given in Appendix 4.10.2.

4.5.2 The planar case

We are interested to apply this formalism to a nematic enclosed in a quasi two dimensional container. If the geometry is such that the depth of the container is much smaller than the other two dimensions and small compared to the length of the particles we expect an in-plane arrangement of the nematic. We therefore restrict ourselves to the planar problem, working out the explicit form of the effective interaction term in two dimensions. Note that the three dimensional effective interaction can be explicitly determined in a similar manner. In two dimensions, upon integration, the terms containing odd number of separation vectors will give vanishing contributions (see appendix 4.10.2). Keeping only the terms with even numbers of components of $\mathbf{s}$, the equation 4.24 becomes:

$$\int d\mathbf{s}\ Q_{\mu\nu}W^{(4)}_{\mu\nu\tau\sigma}(\mathbf{s})Q_{\tau\sigma} - \frac{1}{4}\int d\mathbf{s}\ \partial_\lambda Q_{\mu\nu}s_\lambda W^{(4)}_{\mu\nu\tau\sigma}(\mathbf{s})\partial_\beta Q_{\tau\sigma}s_\beta. \quad (4.26)$$

By integrating the above relation over the separation vector **s** we obtain:

$$Q_{\tau\sigma}Q_{\tau\sigma}\left[4\pi(\bar{w}_0^1+\bar{w}_2^1)+\frac{\pi}{2}\bar{w}_4^1\right]+\partial_\mu Q_{\tau\sigma}\partial_\mu Q_{\tau\sigma}\left(-\pi\bar{w}_0^3-\frac{\pi}{4}\bar{w}_2^3-\frac{\pi}{16}\bar{w}_4^3\right)$$
$$+\partial_\mu Q_{\mu\sigma}\partial_\tau Q_{\tau\sigma}\left(-\frac{\pi}{4}\bar{w}_2^3-\frac{\pi}{8}\bar{w}_4^3\right)++\partial_\mu Q_{\tau\sigma}\partial_\tau Q_{\mu\sigma}\left(-\frac{\pi}{4}\bar{w}_2^3-\frac{\pi}{8}\bar{w}_4^3\right).$$

The complete calculation can be found in the appendix (4.10.3). Including again the dependence on the center of mass gives us the following form for the effective interaction term:

$$\int d\mathbf{R}\left\{Q_{\tau\sigma}(\mathbf{R})Q_{\tau\sigma}(\mathbf{R})\left[4\pi(\bar{w}_0^1+\bar{w}_2^1)+\frac{\pi}{2}\bar{w}_4^1\right]+\partial_\mu Q_{\tau\sigma}(\mathbf{R})\partial_\mu Q_{\tau\sigma}(\mathbf{R})\right.$$
$$\left(-\pi\bar{w}_0^3-\frac{\pi}{4}\bar{w}_2^3-\frac{\pi}{16}\bar{w}_4^3\right)+\partial_\mu Q_{\mu\sigma}(\mathbf{R})\partial_\tau Q_{\tau\sigma}(\mathbf{R})\left(-\frac{\pi}{4}\bar{w}_2^3-\frac{\pi}{8}\bar{w}_4^3\right)$$
$$\left.+\partial_\mu Q_{\tau\sigma}(\mathbf{R})\partial_\tau Q_{\mu\sigma}(\mathbf{R})\left(-\frac{\pi}{4}\bar{w}_2^3-\frac{\pi}{8}\bar{w}_4^3\right)\right\}$$

The last last term can be partially integrated twice:

$$\int d\mathbf{R}\partial_\mu Q_{\tau\sigma}(\mathbf{R})\partial_\tau Q_{\mu\sigma}(\mathbf{R})=\int d\mathbf{A}\hat{n}_\mu Q_{\tau\sigma}(\mathbf{R})\partial_\tau Q_{\mu\sigma}(\mathbf{R})-$$
$$\int d\mathbf{R}Q_{\tau\sigma}(\mathbf{R})\partial_\mu\partial_\tau Q_{\mu\sigma}(\mathbf{R})=\int d\mathbf{A}\hat{n}_\mu Q_{\tau\sigma}(\mathbf{R})\partial_\tau Q_{\mu\sigma}(\mathbf{R})$$
$$-\int d\mathbf{A}\hat{n}_\tau Q_{\tau\sigma}(\mathbf{R})\partial_\mu Q_{\mu\sigma}(\mathbf{R})+\int d\mathbf{R}\partial_\tau Q_{\tau\sigma}(\mathbf{R})\partial_\mu Q_{\mu\sigma}(\mathbf{R}),$$

which allows us to recast the interaction term as:

$$\int d\mathbf{R}\left\{Q_{\tau\sigma}(\mathbf{R})Q_{\tau\sigma}(\mathbf{R})\left[4\pi(\bar{w}_0^1+\bar{w}_2^1)+\frac{\pi}{2}\bar{w}_4^1\right]+\partial_\mu Q_{\tau\sigma}(\mathbf{R})\right.$$
$$\partial_\mu Q_{\tau\sigma}(\mathbf{R})\left(-\pi\bar{w}_0^3-\frac{\pi}{4}\bar{w}_2^3-\frac{\pi}{16}\bar{w}_4^3\right)+\partial_\mu Q_{\mu\sigma}(\mathbf{R})\partial_\tau Q_{\tau\sigma}(\mathbf{R})$$
$$\left.\left(-\frac{\pi}{2}\bar{w}_2^3-\frac{\pi}{4}\bar{w}_4^3\right)\right\}+\int d\mathbf{A}\left[\hat{n}_\mu Q_{\tau\sigma}(\mathbf{R})\partial_\tau Q_{\mu\sigma}(\mathbf{R})\right.$$
$$\left.-\hat{n}_\tau Q_{\tau\sigma}(\mathbf{R})\partial_\mu Q_{\mu\sigma}(\mathbf{R})\right]\left(-\frac{\pi}{4}\bar{w}_2^3-\frac{\pi}{8}\bar{w}_4^3\right)\qquad(4.27)$$

4.6 The planar free energy functional

Recalling from section 4.3, the general form of the free energy given by eq. (4.17) can be expressed as:

$$\beta F\left[\mathbf{Q}\right] = -\rho \int d\mathbf{r}\ \log\ \zeta_{\ \mathbf{Q}}(\mathbf{r}) - \rho \int d\mathbf{r} \mathbf{\Lambda}_{\ \mathbf{Q}}(\mathbf{r}) : \mathbf{Q}(\mathbf{r}) + \\ + \frac{1}{2}\ \rho^2 \int d\mathbf{r} d\mathbf{r}' \mathbf{Q}(\mathbf{r}) \colon \mathbf{W}^{(4)}(\mathbf{r}-\mathbf{r}') : \mathbf{Q}(\mathbf{r}') + \beta F_0 \qquad (4.28)$$

For the planar case, the second term in the above expression can be rewritten (also using the results in appendix 4.10.4) as:

$$\int d\mathbf{r} \mathbf{\Lambda}_{\mathbf{Q}}(\mathbf{r}) : \mathbf{Q}(\mathbf{r}) = 2 \int d\mathbf{r} \Lambda_{\mathbf{Q}}(\mathbf{r}) Q(\mathbf{r}) (\cos^2(2\alpha(\mathbf{r})) + \\ sin^2(2\alpha(\mathbf{r}))) = 2 \int d\mathbf{r} \Lambda_{\mathbf{Q}}(\mathbf{r}) Q(\mathbf{r}), \qquad (4.29)$$

which, together with the results in the previous section, allows us to rewrite the planar free energy functional as:

$$\beta F\left[\mathbf{Q}\right] = -\rho \int d\mathbf{r}\ \log\ \left(2\pi I_0\left[2\Lambda(\mathbf{r})\right]\right) - 2\rho \int d\mathbf{r} \Lambda_{\mathbf{Q}}(\mathbf{r}) Q(\mathbf{r}) + \\ + \frac{1}{2}\ \beta\rho^2 \int d\mathbf{R} \Big\{ Q_{\tau\sigma}(\mathbf{R}) Q_{\tau\sigma}(\mathbf{R}) \left[4\pi(\bar{w}_0^1 + \bar{w}_2^1) + \frac{\pi}{2}\bar{w}_4^1 \right] + \partial_\mu Q_{\tau\sigma}(\mathbf{R}) \partial_\mu Q_{\tau\sigma}(\mathbf{R}) \\ \left(-\pi\bar{w}_0^3 - \frac{\pi}{4}\bar{w}_2^3 - \frac{\pi}{16}\bar{w}_4^3 \right) + \partial_\mu Q_{\mu\sigma}(\mathbf{R}) \partial_\tau Q_{\tau\sigma}(\mathbf{R}) \left(-\frac{\pi}{2}\bar{w}_2^3 - \frac{\pi}{4}\bar{w}_4^3 \right) \Big\} + \\ + \int dA \left[\hat{n}_\mu Q_{\tau\sigma}(\mathbf{R}) \partial_\tau Q_{\mu\sigma}(\mathbf{R}) - \hat{n}_\tau Q_{\tau\sigma}(\mathbf{R}) \partial_\mu Q_{\mu\sigma}(\mathbf{R}) \right] \left(-\frac{\pi}{4}\bar{w}_2^3 - \frac{\pi}{8}\bar{w}_4^3 \right) + \beta F_0.$$

It is convenient to redefine the constants as follows:

$$k := -2\beta\rho \left[4\pi(\bar{w}_0^1 + \bar{w}_2^1) + \frac{\pi}{2}\bar{w}_4^1 \right], \\ k_1 := \frac{\left(\pi\bar{w}_0^3 + \frac{\pi}{8}\bar{w}_2^3 \right)}{\left[4\pi(\bar{w}_0^1 + \bar{w}_2^1) + \frac{\pi}{2}\bar{w}_4^1 \right]}, \\ k_2 := \frac{\left(\frac{\pi}{8}\pi\bar{w}_2^3 + \frac{\pi}{16}\bar{w}_4^3 \right)}{\left[4\pi(\bar{w}_0^1 + \bar{w}_2^1) + \frac{\pi}{2}\bar{w}_4^1 \right]}.$$

By using the explicit values of the components of the two dimensional $\mathbf{Q}$, the free energy takes the form (see appendix 4.10.5 for details of the

summations):

$$\beta F\left[\mathbf{Q}\right] = -\rho \int d\mathbf{r}\ \log\left(2\pi I_0\left[2\Lambda(\mathbf{r})\right]\right) - 2\rho \int d\mathbf{r}\Lambda(\mathbf{r})Q(\mathbf{r}) + \rho \int d\mathbf{r}\left(-\frac{1}{2}kQ^2 + \frac{1}{2}k(k_1+3k_2)\left[(\partial_x Q)^2 + 4Q^2(\partial_x\alpha)^2 + (\partial_y Q)^2 + 4Q^2(\partial_y\alpha)^2\right] + 4kk_2Q(\partial_x Q\partial_y\alpha - \partial_y Q\partial_x\alpha)\right) + \rho \int dA\ 2kk_2Q^2(n_y\partial_x\alpha - n_x\partial_y\alpha) + \beta F_0. \quad (4.30)$$

4.7 The homogeneous solution

In the two dimensional fully homogeneous case the tensor order parameter no longer depends on spatial position, and takes on the simple form:

$$\mathbf{Q} = Q\begin{pmatrix} 1 & 0 \\ 0 & -1 \end{pmatrix}. \quad (4.31)$$

Since the derivatives of the tensor order parameter are identically zero, the free energy can be written as follows:

$$\begin{aligned}\beta F\left[Q\right] &= -\rho V\ \log\left(2\pi I_0\left[2\Lambda\right]\right) - 2\rho V\Lambda Q + \\ &\quad \beta\rho^2 VQ\underbrace{\left[4\pi(\bar{w}_0^1 + \bar{w}_2^1) + \frac{\pi}{2}\bar{w}_4^1\right]}_{\equiv w} + \beta F_0,\end{aligned}$$

where V denotes the volume.

Minimizing the free energy with respect to the scalar oder parameter Q gives us:

$$\frac{\delta\beta F\left[Q\right]}{\delta Q} = 0 \Rightarrow\ -N\frac{\delta\ \log\left(2\pi I_0\left[2\Lambda\right]\right)}{\delta Q} - 2N\Lambda - 2NQ\frac{\delta\Lambda}{\delta Q} + 2\beta\rho Nw Q = 0$$

which can be further rewritten as:

$$-2N\left(\frac{1}{I_0\left[2\Lambda\right]}\frac{\delta I_0\left[2\Lambda\right]}{\delta(2\Lambda)} + Q\right)\frac{\delta\Lambda}{\delta Q} - 2N\Lambda + 2\beta\rho Nw Q = 0 \quad (4.32)$$

Using relation (9.6.27) from Abramovitz & Stegun [112],

$$\frac{\delta I_0\left[2\Lambda\right]}{\delta(2\Lambda)} = I_1\left[2\Lambda\right],$$

the bracket in 4.32 vanishes, which leaves us with the simple solution $\Lambda = \beta\rho w Q$. The scalar order parameter is thus:

$$Q = \frac{I_1\left[kQ\right]}{I_0\left[kQ\right]}, \tag{4.33}$$

where $k \equiv -2\beta\rho w$.

To solve this last equation for the case where $Q \ll 1$, close to the phase transition point, we make the following expansions:

$$Q = \epsilon Q_1 + \epsilon^2 Q_2,$$
$$k = k_* + \epsilon k_1 + \epsilon^2 k_2,$$

rewriting equation 4.33 as:

$$\epsilon Q_1 + \epsilon^2 Q_2 = \frac{I_1\left[(k_* + \epsilon k_1 + \epsilon^2 k_2)(\epsilon Q_1 + \epsilon^2 Q_2)\right]}{I_0\left[(k_* + \epsilon k_1 + \epsilon^2 k_2)(\epsilon Q_1 + \epsilon^2 Q_2)\right]}$$

$$\epsilon Q_1 + \mathcal{O}(\epsilon^2) = \frac{I_1\left[k_* Q_1 \epsilon + \mathcal{O}(\epsilon^2)\right]}{I_0\left[k_* Q_1 \epsilon + \mathcal{O}(\epsilon^2)\right]}.$$

By Taylor expanding we get:

$$\begin{aligned} \epsilon Q_1 + \mathcal{O}(\epsilon^2) &= \frac{I_1\left[0\right]}{I_0\left[0\right]} + \frac{I_1'\left[0\right] I_0\left[0\right] - I_0'\left[0\right] I_1\left[0\right]}{I_0^2\left[0\right]}\, k_* Q_1 \epsilon + \mathcal{O}(\epsilon^2) \\ &= \frac{1}{2} k_* Q_1 \epsilon + \mathcal{O}(\epsilon^2). \end{aligned}$$

where we have used $I_0\left(0\right) = 1, I_1\left(0\right) = 0$ and $I_1'(0) = \frac{1}{2}$ (see formula (9.6.26) from Abramowitz& Stegun [112]). We thus predict that the critical

value of the coupling parameter is given by $k_* = 2$. It is also possible to solve equation 4.33 numerically by a relaxation technique. In figure 4.1 we can see that the transition indeed occurs at $k = 2$.

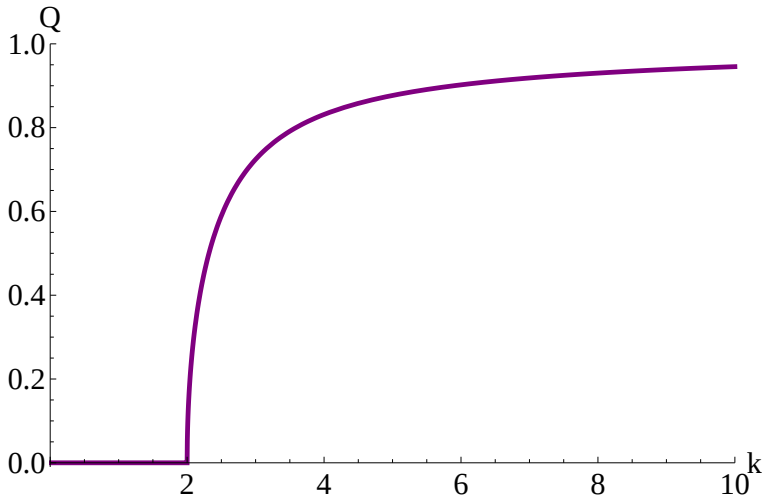

Figure 4.1: Plot of the scalar order parameter as function of parameter k. Note that the transition from the disordered phase to the ordered one occurs at $k = 2$.

4.8 Rectangular confinement

The free energy functional of our model (given in equation 4.30) describes the bulk behavior of a liquid crystal. To mimic confinement we add an anchoring therm to this free energy. We choose an anchoring free energy of the form:

$$\beta F_S[\rho^{(1)}(\mathbf{r}), \hat{\omega}] = \oint_{\partial A} \mathrm{d}s f_S(\hat{\mathbf{b}}(\mathbf{R}), \mathbf{Q}(\mathbf{R})), \tag{4.34}$$

where the local anchoring energy term is chosen to reproduce the classic Rapini-Papoular expression [113],

$$f_S(\hat{\mathbf{n}}(\mathbf{R}), \mathbf{Q}(\mathbf{R})) = \frac{1}{2\sqrt{2}} \frac{W\mathbf{Q}(\mathbf{R}) : \hat{\mathbf{n}}(\mathbf{R}) \otimes \hat{\mathbf{n}}(\mathbf{R})}{\sqrt{\mathbf{Q}(\mathbf{R}) : \mathbf{Q}(\mathbf{R})}} \tag{4.35}$$

$$= \frac{W}{2} \left(\hat{\mathbf{n}}(\mathbf{R}) \cdot \hat{\omega}(\mathbf{R})\right)^2 + \ constant, \tag{4.36}$$

where $\hat{\mathbf{n}}(\mathbf{R})$ is the outward unit normal and $\hat{\omega}(\mathbf{R})$ the local director. For $W > 0$ this term favors alignment parallel to the wall, the energy being minimized by an wall tangential organization.

This free energy functional can not be minimized analytically. We therefore solve it numerically by discretizing the tensor order parameter on a square lattice covering the rectangular container. We make use of a adaptive simulated annealing technique [114]. In addition to the global minima our free energy function has a number of local minima. By using a standard Monte Carlo technique the system would most likely relax to one of these local minima. The simulated annealing technique, however, allows us to cool the system progressively. In this way, in the beginning of the relaxation procedure a lot of non energetically favorable moves happen, allowing the system to escape from the local minima. The temperature is then progressively lowered during the course of the minimization, and the number of moves increasing the energy steadily decreases. We use an adaptive technique, where, in addition to progressively cooling the system we also make smaller and smaller Monte Carlo trial moves as the system approaches its minima. This allows to speed up the relaxation procedure.

For the numerical minimization we choose $k = 2.5$ which, in the bulk corresponds to $Q \approx 0.6$, so that patterns observed are not an artifact of the order saturation. This point is in fact just above the bulk isotropic to nematic transition. For the range of parameters in which the elastic energy competes with the boundary alignment we find two basic orientational patterns. The minimum energy configuration, which we call the D pattern, is characterized by alignment along the walls of the container competing with alignment along one of the diagonals in the central region. At the end of this diagonal spay occurs. On the other diagonal the nematic creates a bend to accommodate the two preferential directions of alignment given by the perpendicular walls (see figure 4.2).

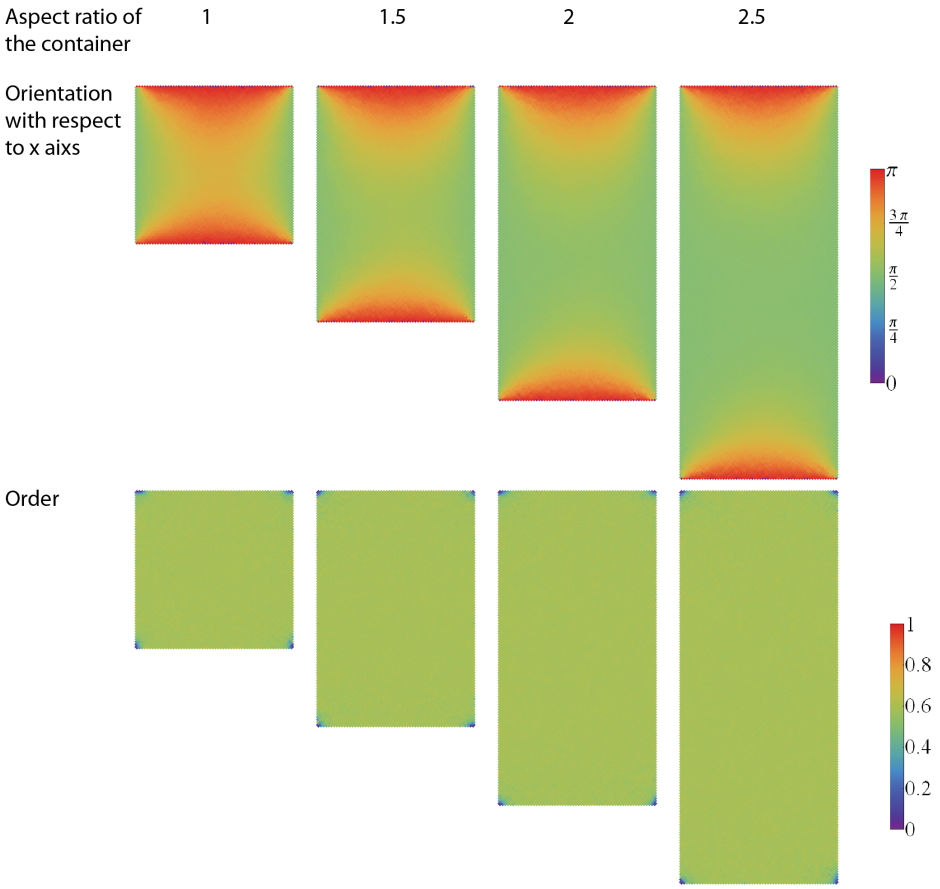

Figure 4.2: The D pattern in boxes with different aspect ratio. All results were obtained for $k = 2.5$*,* $k1 = k2 = 10^{-5}$ *and,* $W = 0.5$*.*

The other basic pattern, called U, is characterized by splays in two adjacent corners of the container, in between which the nematic field creates a u-like bend (see figure 4.3). In the rectangular geometry the two adjacent corners are always along the longest side of the container such that the region in which the nematic is aligned to the wall is increased, resulting in a lower free energy. As expected, the order in both these two patterns corresponds to the bulk value throughout the domain, being lower just in the corners.

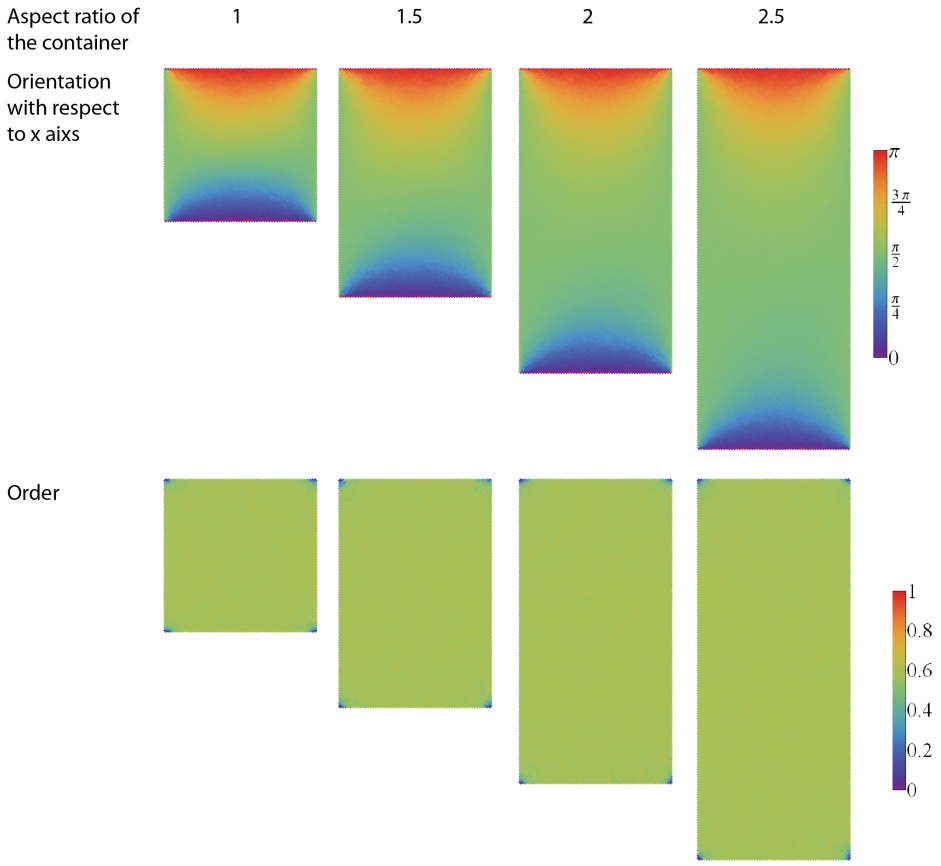

Figure 4.3: The U pattern in boxes with different aspect ratio. All results were obtained for $k = 2.5$, $k1 = k2 = 10^{-5}$ *and,* $W = 0.5$.

Occasionally, we also find these patterns with one or two disclination points. We denote these patterns corresponding to their continuously distorted counterpart as D_1^* and U_1^* for the ones containing one defect point, and as D_2^* and U_2^* for the ones containing two such defects (see figure 4.4). Besides the variation in the orientation around these disclination points we see a drop in scalar order parameter.

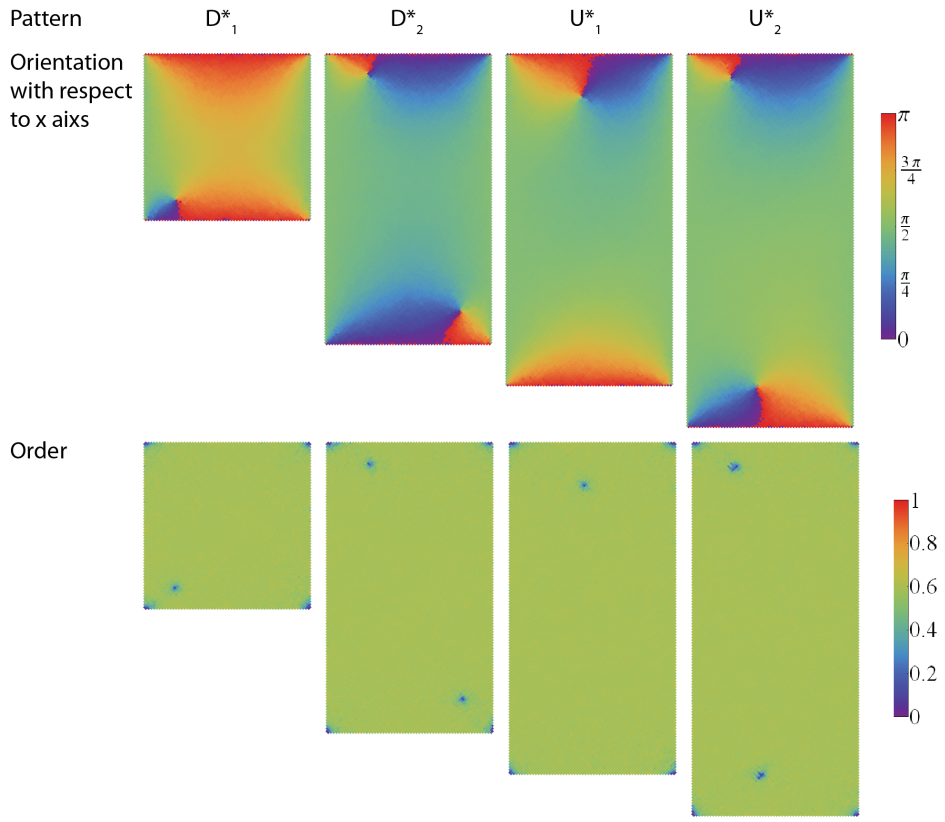

Figure 4.4: Patterns with one or two disclination points. All results were obtained for $k = 2.5$, $k1 = k2 = 10^{-5}$ *and,* $W = 0.5$.

To compare the free energies, we use the system with no elastic coupling (i.e. $k_1 = k_2 = 0$) as a reference. In the square geometry, the D state has the minimum free energy. The U pattern has a 20% higher free energy. In the presence of point defects these free energy differences increase even further, the U_1^* configuration with one point defect being 23% higher in energy and the D_2^* state which contains two point defects is 40% higher. In the rectangular geometry, the free energy between the D and U states decreases with increasing container aspect ratio as the director field will almost everywhere be parallel the longest wall, effectively decoupling the two end walls, which each impose a free energy cost.

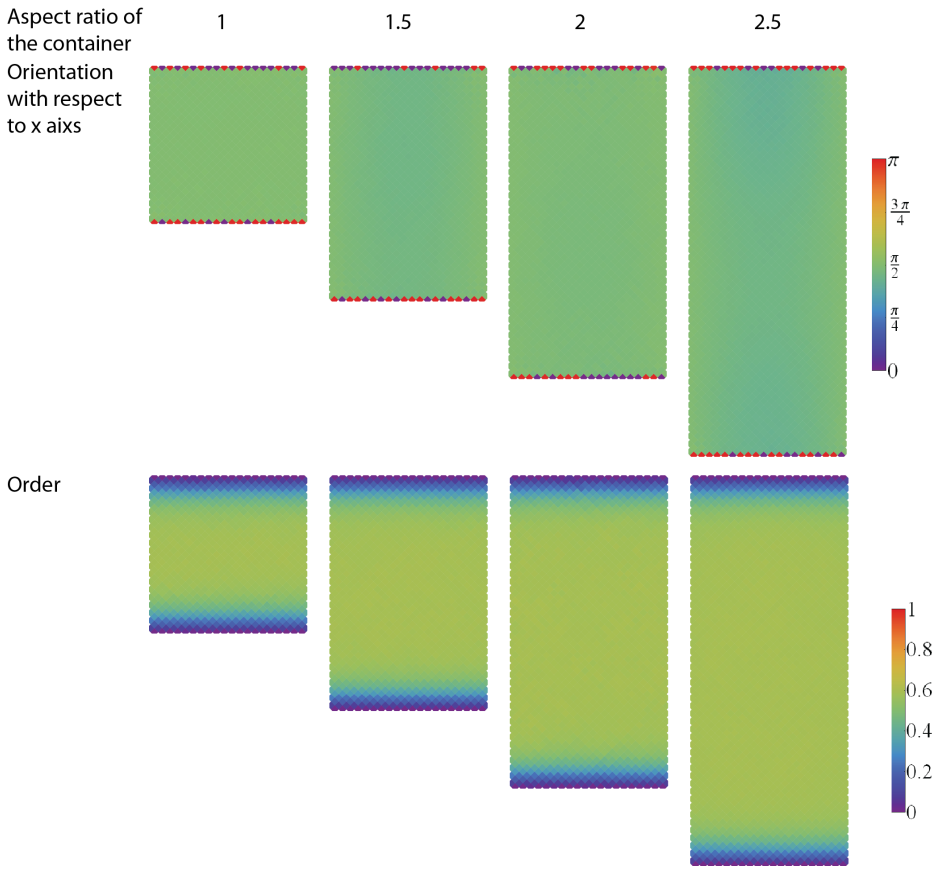

Figure 4.5: The L pattern in boxes with different aspect ratio. All results were obtained for $k = 2.5$, $k1 = 10^{-5}$, $k2 = 10^{-3}$ *and,* $W = 0.5$.

If we increase the elastic constants significantly, the bulk effects dominate the boundary effects and we predict the appearance of the L state, in which the director field is uniform and aligned with the longest axis of the domain (see figure4.5). In this case, we find that at the 'misaligned' walls the system accommodates the mismatch with the boundary potential by significantly decreasing the degree of local order.

4.9 Discussion

We designed a microscopic mean-field model which can accommodate both order and orientation variation. We can apply it to a confined nematic liquid crystals by introducing in our free energy a boundary according term. This term allows us to control the strength of the anchoring and does not require fixing the orientation on the boundary, as it is the case with the Oseen-Frank elastic model. For a rectangular geometry of the confining container, we find that, in the regime where the wall anchoring energy competes with the elastic contribution, the minimum energy configurations are characterized by continuous distortions such as bends or splays. This match the predictions of the Oseen-Frank elastic model. In addition to these continuously deformed configurations, we find that patterns containing one or two defect points are also stable, but have higher energy. For higher anchoring the system sacrifices order along the short wall to align along the longest one, this type of pattern being also forbidden in the Oseen-Frank model. In experiments of colloidal suspensions of fd-viruses confined to shallow rectangular chambers all the patterns predicted by our model appear [115].

4.10 Appendix

4.10.1 Derivation of the effective interaction

The most general interaction expressible as a quadratic in the microscopic polarizability tenor $\mathbf{q}$ is conveniently written as

$$W(\mathbf{r},\hat{\omega};\mathbf{r}',\hat{\omega}') = \mathbf{W}^{(0)}(\mathbf{r}-\mathbf{r}')+$$
$$\mathbf{q}(\hat{\omega}) : \mathbf{W}_1^{(2)}(\mathbf{r}-\mathbf{r}') + \mathbf{W}_2^{(2)}(\mathbf{r}-\mathbf{r}') : \mathbf{q}(\hat{\omega}') + \mathbf{q}(\hat{\omega}) : \mathbf{W}^{(4)}(\mathbf{r}-\mathbf{r}') : \mathbf{q}(\hat{\omega}')$$

This expression already takes care of translation invariance. We still need to insure that it is properly symmetric under the interchange of the two sets of particle coordinates and that the $\mathbf{W}^{(k)}$ actually are tensors of the proper rank. First, we need to introduce a shorthand notation for the separation vector $\mathbf{s} = s\hat{\mathbf{s}} = \mathbf{r}_1 - \mathbf{r}_2$. The tensors can now be built using the standard isotropic tensors $\delta_{\mu\nu}$ and $\epsilon_{\mu\nu\tau}$, the unit vector pointing along the separation vector $\hat{\mathbf{s}}$ and scalars which can be a function of the magnitude s of the interparticle separation. The basis for the zero'th rank tensors is

trivially given by a constant. A basis for the second rank tensors is given by

$$\delta_{\mu\nu} \tag{4.37}$$
$$\hat{\mathbf{s}}_\mu \hat{\mathbf{s}}_\nu \tag{4.38}$$

A basis for the fourth rank tensors constructed from these ingredients is given by

$$\delta_{\mu\nu}\delta_{\sigma\tau} \tag{4.39}$$
$$\hat{\mathbf{s}}_\mu \epsilon_{\nu\sigma\tau} \tag{4.40}$$
$$\hat{\mathbf{s}}_\mu \hat{\mathbf{s}}_\nu \delta_{\sigma\tau} \tag{4.41}$$
$$\hat{\mathbf{s}}_\mu \hat{\mathbf{s}}_\nu \hat{\mathbf{s}}_\sigma \hat{\mathbf{s}}_\tau \tag{4.42}$$

and all other inequivalent tensors obtained by permuting the indices of the above. Since all contractions are performed on the symmetric tensors $\mathbf{q}$ and $\mathbb{I}$, the relevant tensors can, without loss of generality, be taken to be symmetric in the indices that are contracted. Particle interchange symmetry implies that:

(i) $\mathbf{W}_1^{(2)} = \mathbf{W}_2^{(2)} = \mathbf{W}^{(2)}$,

(ii) $\mathbf{W}^{(4)}$ must be symmetric under the interchange of the first two indices with the second two,

(iii) all tensors must be invariant under the substitution $\hat{\mathbf{s}} \to -\hat{\mathbf{s}}$.

Together these requirements lead to the following general form

$$\mathbf{W}^{(0)}(\mathbf{s}) = w^{(0)}(s) \tag{4.43}$$
$$\mathbf{W}^{(2)}(\mathbf{s}) = w_0^{(2)}(s)\delta_{\mu\nu} + w_2^{(2)}(s)\hat{\mathbf{s}}_\mu\hat{\mathbf{s}}_\nu \tag{4.44}$$
$$\begin{aligned}\mathbf{W}^{(4)}(\mathbf{s}) = {} & w_a^{(4)}(s)\delta_{\mu\nu}\delta_{\sigma\tau} + w_b^{(4)}(s)\left\{\delta_{\mu\sigma}\delta_{\nu\tau} + \delta_{\mu\tau}\delta_{\nu\sigma}\right\} + \\ & w_c^{(4)}(s)\left\{\hat{\mathbf{s}}_\mu\hat{\mathbf{s}}_\nu\delta_{\sigma\tau} + \delta_{\mu\nu}\hat{\mathbf{s}}_\tau\hat{\mathbf{s}}_\sigma\right\} + \\ & w_d^{(4)}(s)\left\{\hat{\mathbf{s}}_\mu\delta_{\nu\sigma}\hat{\mathbf{s}}_\tau + \hat{\mathbf{s}}_\mu\delta_{\nu\tau}\hat{\mathbf{s}}_\sigma + \hat{\mathbf{s}}_\nu\delta_{\mu\sigma}\hat{\mathbf{s}}_\tau + \hat{\mathbf{s}}_\nu\delta_{\mu\tau}\hat{\mathbf{s}}_\sigma\right\} \\ & + w_e^{(4)}(s)\hat{\mathbf{s}}_\mu\hat{\mathbf{s}}_\nu\hat{\mathbf{s}}_\tau\hat{\mathbf{s}}_\sigma\end{aligned} \tag{4.45}$$

Finally, because $\mathbf{q}$ is traceless, all contraction with the unit tensor vanish, so that we can set $w_0^{(2)}(s) = w_a^{(4)}(s) = w_c^{(4)}(s) = 0$, leaving the five independent contributions shown in Eq. (4.8).

4.10.2 Integrals over the orientation of the separation vectors

In two dimension the separation vector has the form $\hat{\mathbf{s}} = (\cos\theta, \sin\theta)$. The integral over the orientation of one component of this vector will be:

$$\int d\hat{\mathbf{s}}\ \hat{\mathbf{s}}_\mu = \int_0^{2\pi} d\theta \hat{\mathbf{s}}_\mu = \begin{cases} \int_0^{2\pi} d\theta \cos\theta = 0 & for\ \mu = 0 \\ \int_0^{2\pi} d\theta \sin\theta = 0 & for\ \mu = 1 \end{cases}$$

$$\int d\hat{\mathbf{s}}\ \hat{\mathbf{s}}_\mu = 0 \tag{4.46}$$

The integral of a product of two components of $\hat{\mathbf{s}}$ is:

$$\int d\hat{\mathbf{s}}\hat{\mathbf{s}}_\mu\hat{\mathbf{s}}_\nu = \begin{cases} \int_0^{2\pi} d\theta \cos^2\theta = \pi & for\ (\mu,\nu) = (0,0) \\ \int_0^{2\pi} d\theta \cos\theta\sin\theta = 0 & for\ (\mu,\nu) \in \{(0,1),(1,0)\} \\ \int_0^{2\pi} d\theta \sin^2\theta = \pi & for\ (\mu,\nu) = (1,1) \end{cases}$$

$$\int d\hat{\mathbf{s}}\hat{\mathbf{s}}_\mu\hat{\mathbf{s}}_\nu = \pi\delta_{\mu\nu} \tag{4.47}$$

For a product of three such components the integral will be:

$$\int d\hat{\mathbf{s}}\ \hat{\mathbf{s}}_\mu\hat{\mathbf{s}}_\nu\hat{\mathbf{s}}_\tau = \begin{cases} \int_0^{2\pi} d\theta \cos^3\theta = 0 & for\ (\mu,\nu,\tau) = (0,0,0) \\ \int_0^{2\pi} d\theta \cos^2\theta\sin\theta = 0 & for\ (\mu,\nu,\tau) \in \{(0,0,1), \\ & \quad (0,1,0),(0,0,1)\} \\ \int_0^{2\pi} d\theta \cos\theta\sin^2\theta = 0 & for\ (\mu,\nu) \in \{(0,1,1), \\ & \quad (1,0,1),(1,1,0)\} \\ \int_0^{2\pi} d\theta \sin^3\theta = 0 & for\ (\mu,\nu,\tau) = (1,1,1) \end{cases}$$

$$\int d\hat{\mathbf{s}}\ \hat{\mathbf{s}}_\mu\hat{\mathbf{s}}_\nu\hat{\mathbf{s}}_\tau = 0 \tag{4.48}$$

Integrals of four components give:

$$\int d\hat{\mathbf{s}}\ \hat{\mathbf{s}}_\mu\hat{\mathbf{s}}_\nu\hat{\mathbf{s}}_\tau\hat{\mathbf{s}}_\sigma = \begin{cases} \int_0^{2\pi} d\theta \cos^4\theta = \frac{3\pi}{4} \quad for\ (\mu,\nu,\tau,\sigma) = (0,0,0,0) \\ \int_0^{2\pi} d\theta \sin^4\theta = \frac{3\pi}{4} \quad for\ (\mu,\nu,\tau,\sigma) = (1,1,1,1) \\ \int_0^{2\pi} d\theta \cos^2\theta \sin^2\theta = \frac{\pi}{4} \quad for\ (\mu,\nu,\tau,\sigma) \in \{(0,0,1,1), \\ (0,1,0,1),(1,0,0,1),(1,1,0,0),(1,0,1,0),(0,1,1,0)\} \\ 0 \qquad \text{otherwise} \end{cases}$$

This last result can be rewritten as:

$$\int d\hat{\mathbf{s}}\ \hat{\mathbf{s}}_\mu\hat{\mathbf{s}}_\nu\hat{\mathbf{s}}_\sigma\hat{\mathbf{s}}_\tau = \frac{\pi}{4}(\delta_{\mu\nu}\delta_{\sigma\tau} + \delta_{\mu\sigma}\delta_{\nu\tau} + \delta_{\mu\tau}\delta_{\nu\sigma}) \tag{4.49}$$

The integral of products five $\hat{\mathbf{s}}$ components will be 0:

$$\int d\hat{\mathbf{s}}\ \hat{\mathbf{s}}_\mu\hat{\mathbf{s}}_\nu\hat{\mathbf{s}}_\sigma\hat{\mathbf{s}}_\tau\hat{\mathbf{s}}_\beta = 0 \tag{4.50}$$

For products of six components:

$$\int d\hat{\mathbf{s}}\ \hat{\mathbf{s}}_\mu\hat{\mathbf{s}}_\nu\hat{\mathbf{s}}_\sigma\hat{\mathbf{s}}_\tau\hat{\mathbf{s}}_\beta\hat{\mathbf{s}}_\lambda = \begin{cases} \int_0^{2\pi} d\theta \cos^6\theta = \frac{5\pi}{8} \quad \text{for all indices equal to 0} \\ \int_0^{2\pi} d\theta \sin^6\theta = \frac{5\pi}{8} \quad \text{for all indices equal to 1} \\ \int_0^{2\pi} d\theta \cos^2\theta \sin^4\theta = \frac{\pi}{8} \quad \text{for any 2 indices equal to} \\ \text{0 and the rest of them equal to 1} \\ \int_0^{2\pi} d\theta \cos^4\theta \sin^2\theta = \frac{\pi}{8} \quad \text{for any 2 indices equal to} \\ \text{1 and the rest of them equal to 0} \\ 0 \qquad \text{otherwise} \end{cases}$$

It is more convenient to write the result in terms of Kronecker deltas as follows:

$$\begin{aligned} \int d\hat{\mathbf{s}}\ \hat{\mathbf{s}}_\mu\hat{\mathbf{s}}_\nu\hat{\mathbf{s}}_\sigma\hat{\mathbf{s}}_\tau\hat{\mathbf{s}}_\beta\hat{\mathbf{s}}_\lambda = \frac{\pi}{8}(&\delta_{\mu\nu}(\delta_{\sigma\tau}\delta_{\beta\lambda} + \delta_{\sigma\beta}\delta_{\tau\lambda} + \delta_{\sigma\lambda}\delta_{\tau\beta}) + \\ &\delta_{\mu\sigma}(\delta_{\nu\tau}\delta_{\beta\lambda} + \delta_{\nu\beta}\delta_{\tau\lambda} + \delta_{\nu\lambda}\delta_{\tau\beta}) + \delta_{\mu\tau}(\delta_{\nu\sigma}\delta_{\beta\lambda} + \delta_{\nu\beta}\delta_{\sigma\lambda} + \\ &\delta_{\nu\lambda}\delta_{\sigma\beta}) + \delta_{\mu\beta}(\delta_{\nu\sigma}\delta_{\tau\lambda} + \delta_{\nu\tau}\delta_{\sigma\lambda} + \delta_{\nu\lambda}\delta_{\sigma\tau}) + \delta_{\mu\lambda}(\delta_{\nu\sigma}\delta_{\tau\beta} + \\ &\delta_{\nu\tau}\delta_{\sigma\beta} + \delta_{\nu\beta}\delta_{\sigma\tau})) \end{aligned} \tag{4.51}$$

4.10.3 Planar effective interaction term: the integral over the separation vector

The only two terms in the effective interaction giving non-vanishing contribution upon integration over the separation vector $\mathbf{s}$ are:

$$\int d\mathbf{s}\; Q_{\mu\nu} W^{(4)}_{\mu\nu\tau\sigma}(\mathbf{s}) Q_{\tau\sigma} - \frac{1}{4}\int d\mathbf{s}\; \partial_\lambda Q_{\mu\nu} s_\lambda W^{(4)}_{\mu\nu\tau\sigma}(\mathbf{s}) \partial_\beta Q_{\tau\sigma} s_\beta. \qquad (4.52)$$

By inserting the explicit form of $W^{(4)}_{\mu\nu\tau\sigma}(\mathbf{s})$, given by (4.25), the first term in the above relation is becomes:

$$\begin{aligned}\int d\mathbf{s}\; Q_{\mu\nu} W^{(4)}_{\mu\nu\tau\sigma}(\mathbf{s}) Q_{\tau\sigma} = \int d\mathbf{s}\; Q_{\mu\nu} w_0^{(4)}(s)(\delta_{\mu\sigma}\delta_{\nu\tau} + \delta_{\mu\tau}\delta_{\nu\sigma}) Q_{\tau\sigma} + \\ + \int d\mathbf{s}\; Q_{\mu\nu} w_2^{(4)}(s)(\hat{\mathbf{s}}_\mu \delta_{\nu\sigma}\hat{\mathbf{s}}_\tau + \hat{\mathbf{s}}_\nu \delta_{\mu\sigma}\hat{\mathbf{s}}_\tau + \hat{\mathbf{s}}_\mu \delta_{\nu\tau}\hat{\mathbf{s}}_\sigma + \hat{\mathbf{s}}_\nu \delta_{\mu\tau}\hat{\mathbf{s}}_\sigma) Q_{\tau\sigma} + \\ + \int d\mathbf{s}\; Q_{\mu\nu} w_4^{(4)}(s)\hat{\mathbf{s}}_\mu\hat{\mathbf{s}}_\nu\hat{\mathbf{s}}_\sigma\hat{\mathbf{s}}_\tau Q_{\tau\sigma},\end{aligned}$$

which can be further rewritten as:

$$\begin{aligned}\int d\mathbf{s}\; 2w_0^{(4)}(s) Q_{\tau\sigma} Q_{\tau\sigma} + \\ + \int d\mathbf{s}\; w_2^{(4)}(s) \underbrace{(Q_{\mu\sigma}\hat{\mathbf{s}}_\mu\hat{\mathbf{s}}_\tau + Q_{\sigma\nu}\hat{\mathbf{s}}_\nu\hat{\mathbf{s}}_\tau + Q_{\mu\tau}\hat{\mathbf{s}}_\mu\hat{\mathbf{s}}_\sigma + Q_{\tau\nu}\hat{\mathbf{s}}_\nu\hat{\mathbf{s}}_\sigma)}_{4Q_{\mu\sigma}\hat{\mathbf{s}}_\mu\hat{\mathbf{s}}_\tau} Q_{\tau\sigma} + \\ + \int d\mathbf{s}\; w_4^{(4)}(s) Q_{\mu\nu}\hat{\mathbf{s}}_\mu\hat{\mathbf{s}}_\nu\hat{\mathbf{s}}_\sigma\hat{\mathbf{s}}_\tau Q_{\tau\sigma}.\end{aligned}$$

In polar coordinates this last result reads:

$$\begin{aligned}\int ds\; s\Big[2w_0^{(4)}(s) Q_{\tau\sigma} Q_{\tau\sigma}\int_0^{2\pi} d\theta + 4w_2^{(4)}(s)\int_0^{2\pi} d\theta\; Q_{\mu\sigma}\hat{\mathbf{s}}_\mu\hat{\mathbf{s}}_\tau Q_{\tau\sigma} + \\ + w_4^{(4)}(s)\int_0^{2\pi} d\theta Q_{\mu\nu}\hat{\mathbf{s}}_\mu\hat{\mathbf{s}}_\nu\hat{\mathbf{s}}_\sigma\hat{\mathbf{s}}_\tau Q_{\tau\sigma}\Big].\end{aligned}$$

Making use of the results in appendix 4.10.2 we get:

$$\begin{aligned}\int ds\ s\Big[4\pi w_0^{(4)}(s)Q_{\tau\sigma}Q_{\tau\sigma}+4\pi w_2^{(4)}(s)Q_{\mu\sigma}\delta_{\mu\tau}Q_{\tau\sigma}+\\ \frac{\pi}{4}w_2^{(4)}(s)Q_{\mu\nu}Q_{\tau\sigma}(\delta_{\mu\nu}\delta_{\sigma\tau}+\delta_{\mu\sigma}\delta_{\nu\tau}+\delta_{\mu\tau}\delta_{\nu\sigma})\Big]=\\ \int ds\ s\Big[4\pi w_0^{(4)}(s)Q_{\tau\sigma}Q_{\tau\sigma}+4\pi w_2^{(4)}(s)Q_{\tau\sigma}Q_{\tau\sigma}+\\ \frac{\pi}{4}w_2^{(4)}(s)(Q_{\mu\mu}Q_{\tau\tau}+Q_{\sigma\nu}Q_{\nu\sigma}+Q_{\tau\nu}Q_{\tau\nu})\Big].\end{aligned}$$

Since $\mathbf{Q}$ is traceless, the sum $Q_{\mu\mu}=0$. The final result for the first term in 4.52 is:

$$Q_{\tau\sigma}Q_{\tau\sigma}\left[4\pi\int ds\ s(w_0^{(4)}(s)+w_2^{(4)}(s))+\frac{\pi}{2}\int ds\ sw_4^{(4)}(s)\right]. \tag{4.53}$$

For the second thern in 4.52 we follow the same procedure, first inserting the explicit form of $W^{(4)}_{\mu\nu\tau\sigma}(\mathbf{s})$:

$$\begin{aligned}-\frac{1}{4}\int d\mathbf{s}\ \partial_\lambda Q_{\mu\nu}s_\lambda W^{(4)}_{\mu\nu\tau\sigma}(\mathbf{s})\partial_\beta Q_{\tau\sigma}s_\beta=\\ =-\frac{1}{4}\int d\mathbf{s}\ s^2\partial_\lambda Q_{\mu\nu}\hat{\mathbf{s}}_\lambda W^{(4)}_{\mu\nu\tau\sigma}(\mathbf{s})\partial_\beta Q_{\tau\sigma}\hat{\mathbf{s}}_\beta=\\ =-\frac{1}{4}\int d\mathbf{s}\ s^2\partial_\lambda Q_{\mu\nu}\hat{\mathbf{s}}_\lambda\Big[w_0^{(4)}(s)(\delta_{\mu\sigma}\delta_{\nu\tau}+\delta_{\mu\tau}\delta_{\nu\sigma})+\\ +w_2^{(4)}(s)(\hat{\mathbf{s}}_\mu\delta_{\nu\sigma}\hat{\mathbf{s}}_\tau+\hat{\mathbf{s}}_{nu}\delta_{\mu\sigma}\hat{\mathbf{s}}_\tau+\hat{\mathbf{s}}_\mu\delta_{\nu\tau}\hat{\mathbf{s}}_\sigma+\hat{\mathbf{s}}_\nu\delta_{\mu\tau}\hat{\mathbf{s}}_\sigma)+\\ +w_4^{(4)}(s)\hat{\mathbf{s}}_\mu\hat{\mathbf{s}}_\nu\hat{\mathbf{s}}_\sigma\hat{\mathbf{s}}_\tau\Big]\partial_\beta Q_{\tau\sigma}\hat{\mathbf{s}}_\beta.\end{aligned}$$

By going again to polar coordinates we obtain:

$$\begin{aligned}-\frac{1}{4}\int ds\ s^3\int_0^{2\pi}d\theta\Big[2w_0^{(4)}(s)\partial_\lambda Q_{\sigma\tau}\partial_\beta Q_{\sigma\tau}+\\ +2w_2^{(4)}(s)(\partial_\lambda Q_{\mu\sigma}\hat{\mathbf{s}}_\lambda\hat{\mathbf{s}}_\mu\hat{\mathbf{s}}_\tau\hat{\mathbf{s}}_\beta\partial_\beta Q_{\sigma\tau}+\partial_\lambda Q_{\sigma\nu}\hat{\mathbf{s}}_\lambda\hat{\mathbf{s}}_\nu\hat{\mathbf{s}}_\tau\hat{\mathbf{s}}_\beta\partial_\beta Q_{\sigma\tau}+\\ +\partial_\lambda Q_{\mu\tau}\hat{\mathbf{s}}_\lambda\hat{\mathbf{s}}_\mu\hat{\mathbf{s}}_\sigma\hat{\mathbf{s}}_\beta\partial_\beta Q_{\sigma\tau}+\partial_\lambda Q_{\tau\nu}\hat{\mathbf{s}}_\lambda\hat{\mathbf{s}}_\nu\hat{\mathbf{s}}_\sigma\hat{\mathbf{s}}_{beta}\partial_\beta Q_{\sigma\tau})+\\ +w_4^{(4)}(s)\partial_\lambda Q_{\mu\nu}\partial_\beta Q_{\tau\sigma}\hat{\mathbf{s}}_\lambda\hat{\mathbf{s}}_\mu\hat{\mathbf{s}}_\nu\hat{\mathbf{s}}_\sigma\hat{\mathbf{s}}_\tau\hat{\mathbf{s}}_\beta\Big].\end{aligned} \tag{4.54}$$

Upon performing the $d\theta$ integration the later relation becomes:

$$
\begin{aligned}
-\pi\partial_\lambda Q_{\sigma\tau}\partial_\beta Q_{\sigma\tau}\delta_{\lambda\beta}\int ds\ s^3 w_0^{(4)}(s) - \frac{\pi}{16}\,[\partial_\lambda Q_{\mu\tau}\,(\delta_{\lambda\mu}\delta_{\tau\beta}+\delta_{\lambda\tau}\delta_{\mu\beta}\ + \\
+\delta_{\lambda\beta}\delta_{\mu\tau})\,\partial_\beta Q_{\sigma\tau} + \partial_\lambda Q_{\sigma\nu}(\delta_{\lambda\nu}\delta_{\tau\beta}+\delta_{\lambda\tau}\delta_{\nu\beta}+\delta_{\lambda\beta}\delta_{\nu\tau})\partial_\beta Q_{\sigma\tau} + \\
+\partial_\lambda Q_{\mu\tau}(\delta_{\lambda\mu}\delta_{\sigma\beta}+\delta_{\lambda\sigma}\delta_{\mu\beta}+\delta_{\lambda\beta}\delta_{\mu\sigma})\partial_\beta Q_{\sigma\tau} + \partial_\lambda Q_{\tau\nu}\,(\delta_{\lambda\nu}\delta_{\sigma\beta}+ \\
+\delta_{\lambda\sigma}\delta_{\nu\beta}+\delta_{\lambda\beta}\delta_{\nu\sigma})\,\partial_\beta Q_{\sigma\tau}]\int ds\ s^3 w_2^{(4)}(s) - \frac{\pi}{32}\partial_\lambda Q_{\tau\nu}\partial_\beta Q_{\sigma\tau} \\
[\delta_{\lambda\mu}(\delta_{\nu\sigma}\delta_{\tau\beta}+\delta_{\nu\tau}\delta_{\sigma\beta}+\delta_{\nu\beta}\delta_{\sigma\tau}) + \delta_{\lambda\nu}(\delta_{\mu\sigma}\delta_{\tau\beta}+\delta_{\mu\tau}\delta_{\sigma\beta}+\delta_{\mu\beta}\delta_{\sigma\tau})\ + \\
+\delta_{\lambda\sigma}(\delta_{\mu\nu}\delta_{\tau\beta}+\delta_{\mu\tau}\delta_{\nu\beta}+\delta_{\mu\beta}\delta_{\nu\tau}) + \delta_{\lambda\tau}(\delta_{\mu\nu}\delta_{\sigma\beta}+\delta_{\mu\sigma}\delta_{\nu\beta}+\delta_{\mu\beta}\delta_{\nu\sigma})\ + \\
+\ \delta_{\lambda\beta}(\delta_{\mu\nu}\delta_{\sigma\tau}+\delta_{\mu\sigma}\delta_{\nu\tau}+\delta_{\mu\tau}\delta_{\nu\sigma})]\int ds\ s^3 w_4^{(4)}(s),
\end{aligned}
$$

which can be rewritten as:

$$
\begin{aligned}
-\pi\partial_\beta Q_{\sigma\tau}\partial_\beta Q_{\sigma\tau}\int ds\ s^3 w_0^{(4)}(s) - \frac{\pi}{16}\,(\partial_\mu Q_{\mu\sigma}\partial_\tau Q_{\sigma\tau}+\partial_\tau Q_{\mu\sigma}\partial_\mu Q_{\sigma\tau}\ + \\
+\partial_\beta Q_{\mu\sigma}\partial_\beta Q_{\sigma\mu}+\partial_\nu Q_{\sigma\nu}\partial_\tau Q_{\sigma\tau}+\partial_\tau Q_{\sigma\nu}\partial_\nu Q_{\sigma\tau}+\partial_\beta Q_{\sigma\nu}\partial_\beta Q_{\sigma\nu}\ + \\
+\partial_\mu Q_{\mu\tau}\partial_\sigma Q_{\sigma\tau}+\partial_\sigma Q_{\mu\tau}\partial_\mu Q_{\sigma\tau}+\partial_\beta Q_{\mu\tau}\partial_\beta Q_{\mu\tau}+\partial_\nu Q_{\tau\nu}\partial_\sigma Q_{\sigma\tau}\ + \\
+\partial_\sigma Q_{\tau\nu}\partial_\nu Q_{\sigma\tau}+\partial_\beta Q_{\tau\nu}\partial_\beta Q_{\nu\tau})\int ds\ s^3 w_2^{(4)}(s) - \frac{\pi}{32}\,[\partial_\mu Q_{\mu\nu}\partial_\beta Q_{\sigma\tau} \\
(\delta_{\nu\sigma}\delta_{\tau\beta}+\delta_{\nu\tau}\delta_{\sigma\beta}+\delta_{\nu\beta}\delta_{\sigma\tau}) + \partial_\nu Q_{\mu\nu}\partial_\beta Q_{\sigma\tau}(\delta_{\mu\sigma}\delta_{\tau\beta}+\delta_{\mu\tau}\delta_{\sigma\beta}+\delta_{\mu\beta}\delta_{\sigma\tau})\ + \\
+\partial_\sigma Q_{\mu\nu}\partial_\beta Q_{\sigma\tau}(\delta_{\mu\nu}\delta_{\tau\beta}+\delta_{\mu\tau}\delta_{\nu\beta}+\delta_{\mu\beta}\delta_{\nu\tau}) + \partial_\tau Q_{\mu\nu}\partial_\beta Q_{\sigma\tau}(\delta_{\mu\nu}\delta_{\sigma\beta}+ \\
+\ \delta_{\mu\sigma}\delta_{\nu\beta}+\delta_{\mu\beta}\delta_{\nu\sigma}) + \partial_\beta Q_{\mu\nu}\partial_\beta Q_{\sigma\tau}(\delta_{\mu\nu}\delta_{\sigma\tau}+\delta_{\mu\sigma}\delta_{\nu\tau}+\delta_{\mu\tau}\delta_{\nu\sigma})] \\
\int ds\ s^3 w_4^{(4)}(s) = \\
= -\pi\partial_\beta Q_{\sigma\tau}\partial_\beta Q_{\sigma\tau}\int ds\ s^3 w_0^{(4)}(s) - \frac{\pi}{4}\,(\partial_\mu Q_{\mu\sigma}\partial_\tau Q_{\sigma\tau}+\partial_\tau Q_{\mu\sigma}\partial_\mu Q_{\sigma\tau}\ + \\
+\partial_\tau Q_{\mu\sigma}\partial_\tau Q_{\sigma\mu})\int ds\ s^3 w_2^{(4)}(s) - \frac{\pi}{32}\,[\partial_\mu Q_{\mu\sigma}\partial_\tau Q_{\sigma\tau}+\partial_\mu Q_{\mu\tau}\partial_\sigma Q_{\sigma\tau}+ \\
+\partial_\mu Q_{\mu\beta}\partial_\beta Q_{\sigma\sigma}+\partial_\nu Q_{\sigma\nu}\partial_\tau Q_{\sigma\tau}+\partial_\nu Q_{\tau\nu}\partial_\sigma Q_{\sigma\tau}+\partial_\nu Q_{\beta\nu}\partial_\beta Q_{\sigma\sigma}\ + \\
+\partial_\sigma Q_{\nu\nu}\partial_\tau Q_{\sigma\tau}+\partial_\sigma Q_{\tau\nu}\partial_\nu Q_{\sigma\tau}+\partial_\sigma Q_{\beta\nu}\partial_\beta Q_{\nu\sigma}+\partial_\tau Q_{\nu\nu}\partial_\sigma Q_{\sigma\tau}\ + \\
+\partial_\tau Q_{\sigma\nu}\partial_\nu Q_{\sigma\tau}+\partial_\tau Q_{\beta\nu}\partial_\beta Q_{\nu\tau}+\partial_\beta Q_{\nu\nu}\partial_\beta Q_{\sigma\sigma}+\partial_\beta Q_{\sigma\nu}\partial_\beta Q_{\sigma\nu}\ + \\
+\ \partial_\beta Q_{\tau\nu}\partial_\beta Q_{\nu\tau}]\int ds\ s^3 w_4^{(4)}(s).
\end{aligned}
$$

The last result can be further simplified to :

$$-\pi\partial_\beta Q_{\sigma\tau}\partial_\beta Q_{\sigma\tau}\int ds\ s^3 w_0^{(4)}(s) - \frac{\pi}{4}\left(\partial_\mu Q_{\mu\sigma}\partial_\tau Q_{\sigma\tau} + \partial_\tau Q_{\mu\sigma}\partial_\mu Q_{\sigma\tau} + \right.$$
$$\left.+\partial_\tau Q_{\mu\sigma}\partial_\tau Q_{\sigma\mu}\right)\int ds\ s^3 w_2^{(4)}(s) - \frac{\pi}{32}\left[4\ \partial_\mu Q_{\mu\sigma}\partial_\tau Q_{\tau\sigma} + 4\ \partial_\mu Q_{\tau\sigma}\partial_\tau Q_{\mu\sigma} + \right.$$
$$\left. 2\ \partial_\mu Q_{\tau\sigma}\partial_\mu Q_{\tau\sigma} + 4\ \partial_\mu Q_{\mu\sigma}\partial_\sigma \underbrace{Q_{\tau\tau}}_{=0} + \partial_\mu \underbrace{Q_{\nu\nu}}_{=0}\partial_\mu \underbrace{Q_{\sigma\sigma}}_{=0}\right]\int ds\ s^3 w_4^{(4)}(s).$$

By rearranging the terms we get:

$$\partial_\mu Q_{\tau\sigma}\partial_\mu Q_{\tau\sigma}\left(-\pi\int ds\ s^3 w_0^{(4)}(s) - \frac{\pi}{4}\int ds\ s^3 w_2^{(4)}(s) - \frac{\pi}{16}\int ds\ s^3 w_4^{(4)}(s)\right) +$$
$$+\partial_\mu Q_{\mu\sigma}\partial_\tau Q_{\tau\sigma}\left(-\frac{\pi}{4}\int ds\ s^3 w_2^{(4)}(s) - \frac{\pi}{8}\int ds\ s^3 w_4^{(4)}(s)\right) +$$
$$+\partial_\mu Q_{\tau\sigma}\partial_\tau Q_{\mu\sigma}\left(-\frac{\pi}{4}\int ds\ s^3 w_2^{(4)}(s) - \frac{\pi}{8}\int ds\ s^3 w_4^{(4)}(s)\right).$$

We introduce the following notation:

$$\int ds\ s^k w_p^{(4)}(s) \equiv \bar{w}_p^k, \tag{4.55}$$

and rewrite the result as:

$$\partial_\mu Q_{\tau\sigma}\partial_\mu Q_{\tau\sigma}\left(-\pi\bar{w}_0^3 - \frac{\pi}{4}\bar{w}_2^3 - \frac{\pi}{16}\bar{w}_4^3\right) + \partial_\mu Q_{\mu\sigma}\partial_\tau Q_{\tau\sigma}$$
$$\left(-\frac{\pi}{4}\bar{w}_2^3\frac{\pi}{8}\bar{w}_4^3\right) + \partial_\mu Q_{\tau\sigma}\partial_\tau Q_{\mu\sigma}\left(-\frac{\pi}{4}\bar{w}_2^3 - \frac{\pi}{8}\bar{w}_4^3\right). \tag{4.56}$$

Putting the results 4.53 and 4.56 together gives us the following form for the planar effective interaction (4.52)

$$Q_{\tau\sigma}Q_{\tau\sigma}\left[4\pi(\bar{w}_0^1 + \bar{w}_2^1) + \frac{\pi}{2}\bar{w}_4^1\right] + \partial_\mu Q_{\tau\sigma}\partial_\mu Q_{\tau\sigma}$$
$$\left(-\pi\bar{w}_0^3 - \frac{\pi}{4}\bar{w}_2^3 - \frac{\pi}{16}\bar{w}_4^3\right) + \partial_\mu Q_{\mu\sigma}\partial_\tau Q_{\tau\sigma}\left(-\frac{\pi}{4}\bar{w}_2^3 - \frac{\pi}{8}\bar{w}_4^3\right)$$
$$+\partial_\mu Q_{\tau\sigma}\partial_\tau Q_{\mu\sigma}\left(-\frac{\pi}{4}\bar{w}_2^3 - \frac{\pi}{8}\bar{w}_4^3\right). \tag{4.57}$$

4.10.4 The explicit value of $\mathbf{\Lambda_Q}(\mathbf{r})$

In order to write the free energy functional in two dimensions we need know the explicit form of the field $\mathbf{\Lambda}_{\mathbf{Q}}(\mathbf{r})$. Let us make the following ansatz:

$$\mathbf{\Lambda_Q}(\mathbf{r}) = \Lambda_{\mathbf{Q}}(\mathbf{r}) \begin{pmatrix} \cos(2\alpha(\mathbf{r})) & \sin(2\alpha(\mathbf{r})) \\ \sin(2\alpha(\mathbf{r})) & -\cos(2\alpha(\mathbf{r})) \end{pmatrix}. \tag{4.58}$$

This ansatz should obey the constraint :

$$\mathbf{Q}(\mathbf{r}) = \int d\hat{\boldsymbol{\omega}} \mathbf{q}(\hat{\boldsymbol{\omega}}) \frac{\exp\{-\mathbf{\Lambda_Q}(\mathbf{r}) : \mathbf{q}(\hat{\boldsymbol{\omega}})\}}{\zeta_{\mathbf{Q}}(\mathbf{r})}, \tag{4.59}$$

where

$$\zeta_{\mathbf{Q}}(\mathbf{r}) = \int d\hat{\boldsymbol{\omega}} \ \exp\{-\mathbf{\Lambda_Q}(\mathbf{r}) : \mathbf{q}(\hat{\boldsymbol{\omega}})\}, \tag{4.60}$$

and the two dimensional polarizability tensor is:

$$\mathbf{q}(\hat{\boldsymbol{\omega}}) = 2\ \hat{\boldsymbol{\omega}} \otimes \hat{\boldsymbol{\omega}} - \mathbb{I} = \begin{pmatrix} 2\omega_1^2 - 1 & 2\omega_1\omega_2 \\ 2\omega_1\omega_2 & 2\omega_2^2 - 1 \end{pmatrix}.$$

Using the polar orientation $\hat{\boldsymbol{\omega}} = (\cos\theta, \sin\theta)$ the above expression can be rewritten as:

$$\mathbf{q}(\theta) = \begin{pmatrix} 2\cos^2(\theta) - 1 & 2\cos(\theta)\sin(\theta) \\ 2\cos(\theta)\sin(\theta) & 2\sin^2(\theta) - 1 \end{pmatrix} = \\ = \begin{pmatrix} \cos(2\theta) & \sin(2\theta) \\ \sin(2\theta) & -\cos(2\theta) \end{pmatrix}.$$

We start by computing the exponent in 4.60:

$$-\mathbf{\Lambda_Q}(\mathbf{r}) : \mathbf{q}(\hat{\boldsymbol{\omega}}) = -\Lambda_{\mu\nu}(\mathbf{r}) q_{\mu\nu}(\theta) = -\Lambda_{11}(\mathbf{r}) q_{11}(\theta) - \Lambda_{12}(\theta) q_{12}(\theta) - \\ -\Lambda_{21}(\mathbf{r}) q_{21}(\theta) - \Lambda_{22}(\mathbf{r}) q_{22}(\theta) = -\Lambda(\mathbf{r})(\cos(2\alpha(\mathbf{r}))\cos(2\theta) + \\ + \sin(2\alpha(\mathbf{r}))\sin(2\theta) + \sin(2\alpha(\mathbf{r}))\sin(2\theta) + \cos(2\alpha(\mathbf{r}))\cos(2\theta)) = \\ = -2\Lambda(\mathbf{r})(\cos(2\alpha(\mathbf{r}))\cos(2\theta) + \sin(2\alpha(\mathbf{r}))\sin(2\theta)) = -2\Lambda(\mathbf{r})\cos(2\theta - 2\alpha(\mathbf{r})),$$

which allows us to rewrite 4.60 as:

$$\zeta_{\mathbf{Q}}(\mathbf{r}) = \int_0^{2\pi} d\theta \ e^{-2\Lambda(\mathbf{r})\cos(2\theta - 2\alpha(\mathbf{r}))}.$$

In this last integral we make a variable shift $\theta'(\mathbf{r}) = 2\theta - 2\alpha(\mathbf{r})$ obtaining:

$$\zeta_{\mathbf{Q}}(\mathbf{r}) = \frac{1}{2}\int_{-2\alpha(\mathbf{r})}^{4\pi-2\alpha(\mathbf{r})} d\theta'(\mathbf{r})\; e^{-2\Lambda(\mathbf{r})\cos(\theta'(\mathbf{r}))}.$$

Note that the result is invariant under contour rotation. By using relation (9.6.16) from Abramowitz & Stegun [112] we get:

$$\zeta_{\mathbf{Q}}(\mathbf{r}) = 2\pi I_0\left[2\Lambda(\mathbf{r})\right], \tag{4.61}$$

where I_0 is the modified Bessel function.

The tensor of the right hand side of 4.59 is symmetric and traceless. The 11-component, which is also equal to minus the 22-component, can be written as:

$$\frac{1}{\zeta_{\mathbf{Q}}(\mathbf{r})}\int_0^{2\pi} d\theta\cos(2\theta)\; e^{-2\Lambda(\mathbf{r})\cos(2\theta-2\alpha(\mathbf{r}))},$$

while the other two equal components (12 and 21) read:

$$\frac{1}{\zeta_{\mathbf{Q}}(\mathbf{r})}\int_0^{2\pi} d\theta\sin(2\theta)\; e^{-2\Lambda(\mathbf{r})\cos(2\theta-2\alpha(\mathbf{r}))}.$$

Using again the same variable sift as before gives us:

$$\frac{1}{2\,\zeta_{\mathbf{Q}}(\mathbf{r})}\int_{-2\alpha(\mathbf{r})}^{4\pi-2\alpha(\mathbf{r})} d\theta'(\mathbf{r})\;\cos(\theta'(\mathbf{r})+2\alpha(\mathbf{r}))e^{-2\Lambda(\mathbf{r})\cos(\theta'(\mathbf{r}))},$$

and respectivly:

$$\frac{1}{2\,\zeta_{\mathbf{Q}}(\mathbf{r})}\int_{-2\alpha(\mathbf{r})}^{4\pi-2\alpha(\mathbf{r})} d\theta'(\mathbf{r})\;\sin(\theta'(\mathbf{r})+2\alpha(\mathbf{r}))e^{-2\Lambda(\mathbf{r})\cos(\theta'(\mathbf{r}))}.$$

The last two expression can be recast in the following form:

$$\frac{1}{2\,\zeta_{\mathbf{Q}}(\mathbf{r})}\int_{-2\alpha(\mathbf{r})}^{4\pi-2\alpha(\mathbf{r})} d\theta'(\mathbf{r})\;\Big[(\cos(\theta'(\mathbf{r}))\cos(2\alpha(\mathbf{r}))-\sin(\theta'(\mathbf{r}))\sin(2\alpha(\mathbf{r})))$$
$$e^{-2\Lambda(\mathbf{r})\cos(\theta'(\mathbf{r}))}\Big] = \frac{\cos(2\alpha(\mathbf{r}))}{2\,\zeta_{\mathbf{Q}}(\mathbf{r})}\int_{-2\alpha(\mathbf{r})}^{4\pi-2\alpha(\mathbf{r})} d\theta'(\mathbf{r})\;\cos(\theta'(\mathbf{r}))e^{-2\Lambda(\mathbf{r})\cos(\theta'(\mathbf{r}))} -$$
$$-\frac{\sin(2\alpha(\mathbf{r}))}{2\,\zeta_{\mathbf{Q}}(\mathbf{r})}\int_{-2\alpha(\mathbf{r})}^{4\pi-2\alpha(\mathbf{r})} d\theta'(\mathbf{r})\;\sin(\theta'(\mathbf{r}))e^{-2\Lambda(\mathbf{r})\cos(\theta'(\mathbf{r}))},$$

and

$$\frac{1}{2\ \zeta\ \mathbf{Q}(\mathbf{r})}\int_{-2\alpha(\mathbf{r})}^{4\pi-2\alpha(\mathbf{r})} d\theta'(\mathbf{r})\ \left[(\sin(\theta'(\mathbf{r}))\cos(2\alpha(\mathbf{r}))+\cos(\theta'(\mathbf{r}))\sin(2\alpha(\mathbf{r}))\right.$$
$$\left.e^{-2\Lambda(\mathbf{r})\cos(\theta'(\mathbf{r}))}\right] = \frac{\cos(2\alpha(\mathbf{r}))}{2\ \zeta\ \mathbf{Q}(\mathbf{r})}\underbrace{\int_{-2\alpha(\mathbf{r})}^{4\pi-2\alpha(\mathbf{r})} d\theta'(\mathbf{r})\ \sin(\theta'(\mathbf{r}))e^{-2\Lambda(\mathbf{r})\cos(\theta'(\mathbf{r}))}}_{\equiv A}+$$
$$+\frac{\sin(2\alpha(\mathbf{r}))}{2\ \zeta\ \mathbf{Q}(\mathbf{r})}\underbrace{\int_{-2\alpha(\mathbf{r})}^{4\pi-2\alpha(\mathbf{r})} d\theta'(\mathbf{r})\ \cos(\theta'(\mathbf{r}))e^{-2\Lambda(\mathbf{r})\cos(\theta'(\mathbf{r}))}}_{\equiv B}.$$

The integral A vanishes for symmetry reasons. To obtain the result of the integral B we will use the relation (9.6.19) from Abramowitz & Stegun [112]to obtain

$$B = -4\pi I_1\left[2\Lambda(\mathbf{r})\right].$$

Finally, the result for the tensor on the right hand side of 4.59 is:

$$-\frac{I_1\left[2\Lambda(\mathbf{r})\right]}{I_0\left[2\Lambda(\mathbf{r})\right]}\begin{pmatrix}\cos(2\alpha(\mathbf{r})) & \sin(2\alpha(\mathbf{r}))\\ \sin(2\alpha(\mathbf{r})) & -\cos(2\alpha(\mathbf{r}))\end{pmatrix}. \tag{4.62}$$

Since

$$\mathbf{Q}(\mathbf{r}) = Q(\mathbf{r})\begin{pmatrix}\cos(2\alpha(\mathbf{r})) & \sin(2\alpha(\mathbf{r}))\\ \sin(2\alpha(\mathbf{r})) & -\cos(2\alpha(\mathbf{r}))\end{pmatrix}, \tag{4.63}$$

in order for the constraint 4.59 to be obeyed, we should have:

$$Q(\mathbf{r}) = -\frac{I_1\left[2\Lambda(\mathbf{r})\right]}{I_0\left[2\Lambda(\mathbf{r})\right]}. \tag{4.64}$$

4.10.5 Computing the sums over components of Q

The free energy functional is written is terms of summations over components of the tensor order parameter and their derivatives. For the two dimensional case, using the explicit value of these components and performing the summation simplifies the form of the free energy functional.

$$Q_{\tau\sigma}Q_{\tau\sigma} = Q_{11}+Q_{12}+Q_{21}+Q_{22} = Q^2(\cos^2 2\alpha+\sin^2 2\alpha+$$
$$+\sin^2 2\alpha+\cos^2 2\alpha) = 2Q^2 \tag{4.65}$$

$$\partial_\mu Q_{\tau\sigma}\partial_\mu Q_{\tau\sigma} = 2(\partial_x Q_{11})^2 + 2(\partial_x Q_{12})^2 + 2(\partial_y Q_{11})^2 + 2(\partial_y Q_{12})^2 =$$
$$= 2\left[(\partial_x(Q\cos 2\alpha))^2 + (\partial_x(Q\sin 2\alpha))^2 + (\partial_y(Q\cos 2\alpha))^2 + (\partial_y(Q\sin 2\alpha))^2\right] =$$
$$= 2\left[(\partial_x Q\cos 2\alpha - 2Q\sin 2\alpha\partial_x\alpha)^2 + (\partial_x Q\sin 2\alpha + 2Q\cos 2\alpha\partial_x\alpha)^2 +\right.$$
$$\left.+(\partial_y Q\cos 2\alpha - 2Q\sin 2\alpha\partial_y\alpha)^2 + (\partial_y Q\sin 2\alpha + 2Q\cos 2\alpha\partial_y\alpha)^2\right] =$$
$$= 2\left[(\partial_x Q)^2\cos^2 2\alpha + 4Q^2\sin^2 2\alpha(\partial_x\alpha)^2 - 4Q\cos 2\alpha\sin 2\alpha\partial_x Q\partial_x\alpha +\right.$$
$$+ (\partial_x Q)^2\sin^2 2\alpha + 4Q^2\cos^2 2\alpha(\partial_x\alpha)^2 + 4Q\cos 2\alpha\sin 2\alpha\partial_x Q\partial_x\alpha +$$
$$(\partial_y Q)^2\cos^2 2\alpha + 4Q^2\sin^2 2\alpha(\partial_y\alpha)^2 - 4Q\cos 2\alpha\sin 2\alpha\partial_y Q\partial_y\alpha +$$
$$\left.+ (\partial_y Q)^2\sin^2 2\alpha + 4Q^2\cos^2 2\alpha(\partial_y\alpha)^2 + 4Q\cos 2\alpha\sin 2\alpha\partial_y Q\partial_y\alpha\right] =$$
$$= 2\left[(\partial_x Q)^2 + 4Q^2(\partial_x\alpha)^2 + (\partial_y Q)^2 + 4Q^2(\partial_y\alpha)^2\right]$$

$$\partial_\mu Q_{\mu\sigma}\partial_\tau Q_{\tau\sigma} = \partial_x Q_{11}\partial_x Q_{11} + \partial_x Q_{12}\partial_x Q_{12} + \partial_x Q_{11}\partial_y Q_{21} +$$
$$+\partial_x Q_{12}\partial_y Q_{22} + \partial_y Q_{21}\partial_x Q_{11} + \partial_y Q_{22}\partial_x Q_{12} + \partial_y Q_{21}\partial_y Q_{21} +$$
$$+\partial_y Q_{22}\partial_y Q_{22} = (\partial_x Q_{11})^2 + (\partial_x Q_{12})^2 + 2\partial_x Q_{11}\partial_y Q_{21} + 2\partial_x Q_{12}\partial_y Q_{22} +$$
$$+(\partial_y Q_{21})^2 + (\partial_y Q_{22})^2 = (\partial_x Q\cos 2\alpha - 2Q\sin 2\alpha\partial_x\alpha)^2 +$$
$$(\partial_x Q\sin 2\alpha + 2Q\cos 2\alpha\partial_x\alpha)^2 + 2(\partial_x Q\cos 2\alpha - 2Q\sin 2\alpha\partial_x\alpha)(\partial_y Q\sin 2\alpha +$$
$$+2Q\cos 2\alpha\partial_y\alpha) + 2(\partial_x Q\sin 2\alpha + 2Q\cos 2\alpha\partial_x\alpha)(-\partial_y Q\cos 2\alpha + 2Q\sin 2\alpha\partial_y\alpha) +$$
$$+(\partial_y Q\sin 2\alpha + 2Q\cos 2\alpha\partial_y\alpha)^2 + (\partial_y Q\cos 2\alpha - 2Q\sin 2\alpha\partial_y\alpha)^2 =$$
$$= (\partial_x Q)^2 + 4Q^2(\partial_x\alpha)^2 + 2(2Q\cos^2 2\alpha\partial_x Q\partial_y\alpha - 2Q\sin^2 2\alpha\partial_y Q\partial_x\alpha +$$
$$-2Q\cos^2 2\alpha\partial_y Q\partial_x\alpha + 2Q\sin^2 2\alpha\partial_x Q\partial_y\alpha) + (\partial_y Q)^2 + 4Q^2(\partial_y\alpha)^2 =$$
$$= (\partial_x Q)^2 + 4Q^2(\partial_x\alpha)^2 + 4Q(\partial_x Q\partial_y\alpha - \partial_y Q\partial_x\alpha) + (\partial_y Q)^2 + 4Q^2(\partial_y\alpha)^2$$

$$n_\mu Q_{\tau\sigma}\partial_\tau Q_{\mu\sigma} - n_\tau Q_{\tau\sigma}\partial_\mu Q_{\mu\sigma} = n_x Q_{11}\partial_x Q_{11} + n_x Q_{12}\partial_x Q_{12} +$$
$$+n_x Q_{21}\partial_y Q_{11} + n_x Q_{22}\partial_y Q_{21} + n_y Q_{11}\partial_x Q_{21} + n_y Q_{12}\partial_x Q_{22} +$$
$$+n_y Q_{21}\partial_y Q_{21} + n_y Q_{22}\partial_y Q_{22} - n_x Q_{11}\partial_x Q_{11} - n_x Q_{11}\partial_y Q_{21} -$$
$$-n_x Q_{12}\partial_x Q_{12} - n_x Q_{12}\partial_y Q_{22} - n_y Q_{21}\partial_x Q_{11} - n_y Q_{21}\partial_y Q_{21} -$$
$$-n_y Q_{22}\partial_x Q_{12} - n_y Q_{22}\partial_y Q_{22} = n_x(Q_{21}\partial_y Q_{11} + Q_{22}\partial_y Q_{12} -$$
$$-Q_{12}\partial_y Q_{22} - Q_{11}\partial_y Q_{21}) + n_y(Q_{11}\partial_x Q_{21} + Q_{12}\partial_x Q_{22} -$$
$$-Q_{21}\partial_x Q_{11} - Q_{22}\partial_x Q_{12}) = 2n_x(Q_{21}\partial_y Q_{11} - Q_{11}\partial_y Q_{21}) +$$
$$2n_y(Q_{11}\partial_x Q_{21} - Q_{21}\partial_x Q_{11}) = 2n_x(Q\sin 2\alpha(\partial_y Q\cos 2\alpha - 2Q\sin 2\alpha\partial_y\alpha) -$$
$$-Q\cos 2\alpha(\partial_y Q\sin 2\alpha + 2Q\cos 2\alpha\partial_y\alpha)) + 2n_y(Q\cos 2\alpha(\partial_x Q\sin 2\alpha + 2Q\cos 2\alpha\partial_x\alpha) -$$
$$-Q\sin 2\alpha(\partial_x Q\cos 2\alpha - 2Q\sin 2\alpha\partial_x\alpha)) = 2n_x(-2Q^2\partial_y\alpha) + 2n_y(2Q^2\partial_x\alpha) =$$
$$= 4Q^2(n_y\partial_x\alpha - n_x\partial_y\alpha)$$

5

The mechanical interplay between cytoskeletal filaments and cell membrane as a driver for the spatial organization of cells

The shape of animal cells is regulated by the interplay between the cytoskeleton and the enclosing cellular membrane. Both F-actin and microtubules are relatively stiff filamentous protein assemblies. In processes such as animal cell division or cell migration, networks of these filaments dynamically reorganize themselves in the intracellular space. On the one hand they exert forces on the membrane and deform it. On the other hand, the membrane itself is under tension and will therefore also exert forces on the cytoskeleton, thus constraining and influencing its organization. This mutual interplay of cytoskeleton and membrane shape remains poorly understood, since it is hard to dissect in the crowded intracellular environment. However, bio-mimetic systems such as liposomes and emulsion droplets encapsulating filaments are successfully used as minimal experimental model systems to study this problem. Inspired by this synthetic biology approach, we study the interplay between the organization of cytoskeletal filaments and the shape of the confining membrane using computer simulations.

5.1 Introduction

The mechanical interaction between the cytoskeleton and the cellular membrane is crucial for living cells. This interaction defines the shape of the cell and in turn constrains the spatial organization of the cytoskeleton. All animal cells have a lipid bilayer membrane that separates the cytoplasm from the extra-cellular space. Unlike plants and bacteria, animal cells do not have a cell wall to rigidify the membrane, and thus can be deformed. The enclosed cytoskeletal polymers grow against it and modify its shape. However, the cytoskeletal filaments are flexible themselves, and when they encounter the membrane they often bend. This interaction plays an important part in key processes such as migration and division. During migration, actin pushes against the membrane and creates thin protrusions called lamellipodia [24]. The actin network is in turn forced to organize itself inside this flat confining geometry. During cell division, microtubules radiating outward from centrosomes exert forces on the membrane, and in turn are acted upon by the membrane, causing them to bend or buckle. Together these processes are responsible for the proper positioning and orientation of the mitotic spindle [116]. By deforming the membrane, the cytoskeleton creates an anisotropic geometrical environment, which in turn influences the spatial organization of the filaments, thus contributing to cell polarization. Strikingly, this interaction is also important not only in complete cells, but also in cell fragments. An example is blood platelets: In the inactivate state platelets have a discoid shape defined by a ring of strongly bent microtubules located on the circumference of the disk [117, 118, 119]. The ring is essential for maintaining the discoidal shape, and disassembling this ring makes the platelets become spherical [21].

Clearly, living cells are very complex systems containing many components with complex interactions. The modern synthetic biology approach aims to understand, and perhaps eventually build cells, by bottom-up engineering of cells from a few essential components. Experiments along these lines, like enclosing cytoskeletal filaments inside lipid vesicles, are proving to be very useful for understanding the mechanical interaction between the cytoskeleton and the membrane [120, 43, 44, 121]. This method is more suited to study the actin cortex [46], since the forces that a single filament applies to the membrane are generally small compared to the elasticity and surface tension of the bilayer. To understand the mechanical interaction between microtubules and membranes emulsion droplets offer a more ap-

propriate set-up. Microtubules are stiffer than actin filaments and, when pushing against just a naked bilayer, they can create large deformations. Most experimental studies so far [50, 122, 49] focused on this regime, in which the filaments are very stiff compared to the membrane. In a biological context these large deformations are less common since the membrane is reinforced by the actin cortex. Emulsion droplets are much stiffer than liposomes due to the oil buffer in which they are immersed. This offers a more relevant biological regime in which the stiffness of the membrane and the filaments are comparable. It is thus a powerful tool to study self organization of microtubules in confinement [123] and microtubule aster positioning [48]. It can also be useful for studying actin bundles in confinement since actin filaments crosslinked, for example, with fascin reach persistence lengths comparable to that of microtubules [124]. Experiments by Feng-Ching Tsai (group of Prof Dr Gijsje Koenderink, AMOLF) show that actin filaments bundled by fascin enclosed in emulsion droplets self organize, depending on their length, in either asters or circumferential rings [125]. Microtubules confined to emulsion droplets exhibit more diversity in the organization as a function of length as the experiments of Sophie Roth (group of Prof Dr Marileen Dogterom, TU Delft) reveal [126]. Short enough filaments remain straight and are evenly dispersed in the volume of the droplet. However, if they are longer, such that they are effectively constrained by the droplet walls, they form either a single bundle along a diameter of the droplet or an aster-like structure in the equatorial plane. Bipolar structures and patterns characterized by one circumferential ring were also observed. The difference between the patterns formed by these two cytoskeletal polymers is due to their bending stiffness compared to the surface tension and the elasticity of the monolayer. The shape of a liposome or of an emulsion droplet in the absence of any external forces is spherical [127]. Actin bundles are less stiff and do not deform the droplet whereas microtubules change the shape of the droplet into an ellipsoid, which is either flattened (oblate) or elongated (prolate). This creates an asymmetric confinement volume which exhibits preferential directions of alignment giving rise to anisotropic structures such as bundles.

Inspired by these intriguing experimental results, we study the mechanisms that dictate the mechanical interactions between the membrane and the cytoskeletal filaments. So far, the theoretical studies [128, 129, 130] have mostly focused on deformation of membranes by a rigid filaments. Studies

of semiflexible polymers enclosed in spherical cavities deal with the regime where the persistence length is low compared to the confining volume dimensions [131, 132] which is more relevant, for example, for chromatin packing inside the nucleus rather than for cytoskeletal filaments. Other studies concentrate on a confined closed semi-flexible ring [133, 134, 135, 136, 137] or analyze the regime in which the polymer confined by a soft membrane is several times longer than the dimension of the confining volume [138, 139]. We aim to investigate the interplay between the forces applied by the cytoskeleton and the elastic response of the membrane in a biologically more relevant regime, where these responses are comparable. We direct our attention to the regime where the confined polymers have a length up to the circumference of the droplet since this seems to correspond most closely to the experimental situation.

The problem of mechanical interplay between the cytoskeletal polymers and the confining membrane is rather complex, since it relies on the minimization of both the the elastic energy of the cytoskeleton enclosed and of the confining surface. This problem can be divided in several parts, employing a combination of computer simulations and elasticity theory. In this chapter, using Monte Carlo simulation, we study the organization of semiflexible filaments inside fixed ellipsoidal geometries. These simulations allow us to determine the organization of the filaments for different geometrical parameters of the confining surface. For each set of parameters the filaments will adopt the most favorable configuration. The simulations also enable us to study the influence of the total length of the filaments and of their rigidity on the cytoskeletal organization as a function of the asymmetry of the confining surface. The elastic energy of the membrane and the surface tension can be computed analytically and, in combination with the bending energy of the enclosed cytoskeleton — determined from the curvature predicted by the simulations- gives the minimum energy of the whole system. More details on this procedure will be given in the final chapter.

5.2 Semiflexible polymers confined in ellipsoidal volumes

Microtubules as well as bundles of actin crosslinked with fascin confined in spheroidal volumes with an average diameter of 10-20 μm behave like

an elastic rod. At this length scale the thermal fluctuations can be ignored since the persistence length of these polymers or polymers bundles is around two orders of magnitude higher than the maximum length available inside the confining volume. Microtubules or F-actin bundles are fairly accurately described by semiflexible polymers. We model semiflexible polymers as chains of spherocylindrical segments of length l and diameter D, two neighboring segments sharing the same capping sphere (see figure 5.1 (a)). Each joint has a bending energy associated to it that is a function of the angle between the segments. The total bending energy of the polymer is a sum of the bending cost of all of its joints. For such a semiflexible chain the bending energy can thus be written as:

$$U_B = \frac{\kappa}{2l} \sum_{i=2}^{n} \theta_{i-1,i}^2 \tag{5.1}$$

where κ is the bending constant, $\theta_{i-1,i}$ the angle between two adjacent segments and n the total number of segments. The bending constant κ can be directly related to the persistence length via the following relation:

$$l_p = \frac{\kappa}{k_B T} \tag{5.2}$$

where k_B is the Boltzmann constant and T the temperature [7]. In the absence of forces applied to it, the polymer will adopt a straight rod configuration, corresponding to the minimum of the bending energy. As the polymers are extended tree-dimensional objects, characterized by a thickness and a total length, they will interact with each other and the enclosing membrane via steric repulsion. In the experiments on reconstructed systems, the polymer density is very low (volume fraction of the polymers in the droplets being $\sim 0.1\%$ [126, 125]). Thus the polymer-polymer interactions can therefore in first instance be neglected. We will study the behavior of one single polymer, obtaining the multi-polymer patterns as a superposition of single polymer configurations. The straight rod configuration of a polymer can be maintained as long as there is enough space inside the confining volume. When the polymer exceeds in length the diameter of the confining volume it becomes constrained by the walls having to bend in order to fit inside.

When F-actin bundles are confined in emulsion droplets, the shape of the droplet remains spherical. However, for microtubules, slightly ellipsoidal droplets (both oblate and prolate) were observed. This asymmetry

of the confining volume gives rise to organizations that are unlikely to appear in the spherical geometry, such as single bundles or planar asters. To understand how this asymmetry influences the organization of the polymers inside, we design Monte Carlo simulations of semiflexible polymers enclosed in rigid ellipsoidal surfaces. We obtain the ellipsoidal surface by deforming a sphere into a rotation ellipsoid, which can be either oblate or prolate, keeping the enclosed volume constant. The ellipsoids are fully described by the lengths of the two symmetry axes L_z and $L_x = L_y$ (see figure 5.1 (b)). For the oblate geometry we have $L_z < L_x$, whereas the prolate geometry obeys $L_z > L_x$. We define the asymmetry (also called the aspect ratio) as the ratio of the two principal axis as:

$$\lambda = \frac{L_z}{L_x}. \tag{5.3}$$

We analyze the regime where the parameter λ is between 0.5 and 2.

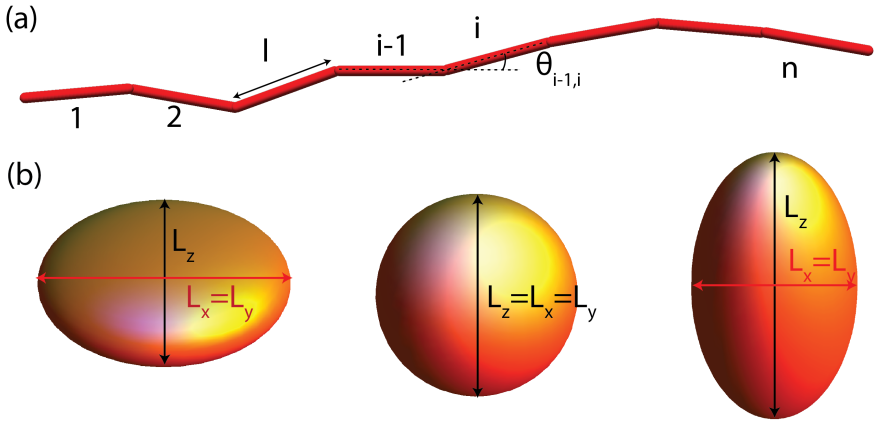

Figure 5.1: (a) Illustration of our semiflexible polymer. (b) Illustration of the confining surface (left— oblate ellipsoid, center— sphere and right— prolate ellipsoid).

5.2.1 Simulation technique

We use a conformational-bias Monte Carlo technique [66] to grow a single polymer at the time inside the confining surface. This technique of growing polymers bond-by bond is based on the Rosenbluth scheme [140] which allows generation of ensembles of polymer conformations. However the configurations generated by the Rosenbluth method are not necessarily a representative sample of all the possible configurations. The conformational-bias Monte Carlo technique introduces a bias in the acceptance rate which ensures that the sampling is done according to the Boltzmann weight of the configuration.

The standard continuous conformational-bias Monte Carlo works as follows: assuming we have already grown $i-1$ segments, for each new bond i we want to grow we generate a set of k trail bonds, each trail bond being generated according to the Boltzmann weight associated with the bending energy. The probability to generate a bond with orientation $\mathbf{b}$ is:

$$p_i^{bond}(\mathbf{b})d\mathbf{b} = Ce^{-\beta u_i^{bond}(\mathbf{b})}d\mathbf{b} = Ce^{-\frac{lp}{2l}\theta_{i-1,i}^2}d\mathbf{b}, \tag{5.4}$$

where C is a normalization constant. In order to choose one of these k bonds we use the external potential. Since we have steric repulsion both in between the spherocylinders constituting the chain and in between the polymer and the wall, the Boltzmann factor $e^{-\beta u_i^{ext}(\mathbf{b})}$ of a trial segment will be 0 when the segment overlaps with another one or with the wall and will be 1 otherwise. The overlap criteria between an ellipsoidal surface and a rod is discussed in the appendix 5.5.1. The probability of choosing a bond j out of our set is:

$$p_i^{ext}(\mathbf{b}_j) = \frac{e^{-\beta u_i^{ext}(\mathbf{b}_j)}}{w_i^{ext}(j)}, \tag{5.5}$$

where

$$w_i^{ext}(j) = \sum_{m=1}^{k} e^{-\beta u_i^{ext}(\mathbf{b}_m)} \tag{5.6}$$

is defined as the Rosenbluth factor. The chosen bond becomes part of our chain and we repeat the procedure until reach the desired length $L = nl$ of the polymer. For the full chain we compute the Rosenbluth weight as a product of Rosenbluth factors of each segment:

$$W^{ext}(new) = \prod_{i=1}^{n} w_i^{ext}(j). \tag{5.7}$$

The Rosenbluth factor of the initial segment is given by:

$$w_1^{ext}(j) = ke^{-\beta u_i^{ext}(\mathbf{b}_1)} = k. \tag{5.8}$$

This procedure allows us to grow a new polymer. The acceptance rate of this new configuration is:

$$acc(old \rightarrow new) = min(1, W^{ext}(new)/W^{ext}(old)) \tag{5.9}$$

Therefore, if the new chain has a lower Rosenbluth weight, it is always accepted, otherwise it is accepted with a probability that depends on the ratio of their Rosenbluth weights. This procedure ensures that the ensemble of polymers we generate is representative for the ensemble of possible configurations [141].

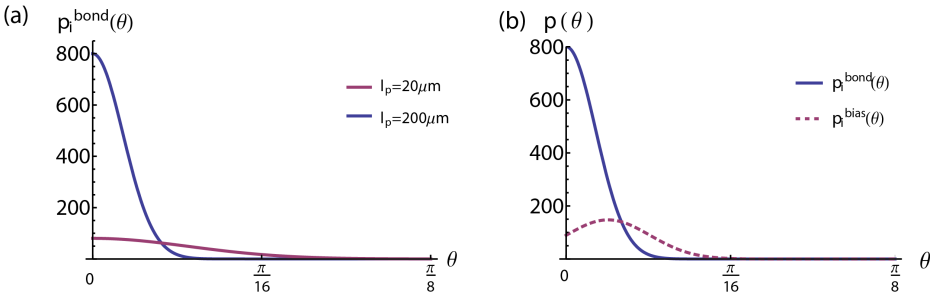

Figure 5.2: (a) Probability distribution from which trial segments are choose for two different persistence length. (b) Probability distribution associated with the bending and biased distribution for $l_p = 200\mu m$. The bias angle is $\theta^1 = 0.1$. We only show the probability distributions up to $\theta = \pi/8$, since above this value, for the persistence lengths considered, they are zero.

The above procedure works very well for polymers that do not exceed in length the diameter of the confining surface or for polymers with a persistence length comparable to the distance available in the confining volume. When the polymer becomes stiffer the probability distribution from which we draw the new bonds becomes narrower (see figure 5.2 (a)), the angle that the new bond make with the existing one becoming very small. Effectively the polymer is almost straight. When the polymer is short enough that it can fit inside the confining surface without bending, the technique is

still efficient. However, when the polymer is longer than the minimum distance available it has to bend in order to fit. The probability of generating bent polymers is low, but the straight configurations almost surely collide with the wall and are therefore rejected. In this regime this simulation technique becomes too costly, the computational time needed to generate a representative ensemble being too high.

It is possible to modify the above scheme by introducing an additional bias [142]. The idea is the following: instead of generating the new bonds according to the Boltzmann weight associated with the bending energy we generate them from a different distribution that is more likely to result in accepted configurations. One of the problems of standard conformational-bias Monte Carlo technique is that, in confinement, the polymer "feels" the wall only when it is at maximum one bond length away from it. This means that, especially for stiff polymers, the chain grows more or less straight towards the wall and in its close proximity, almost all the possible trial segments will go through the wall leading to the rejection of the whole polymer (see figure 5.3 (a)). In order to avoid this problem, the bonds can be sampled from a distribution that prefers segments to be closer in orientation to the tangent to the wall as the distance to the wall becomes smaller. This potential generates polymers that deflect from the wall (see figure 5.3 (b)) and is effective in a simple geometry, such a the cylindrical one. In the case of long stiff polymers confined in ellipsoidal volumes computing the distance from a point to the surface is computationally demanding. The polymer will fit in the ellipsoid only if the angle between its segments is high (see figure 5.3 (c)). We choose to sample the segments from the following distribution:

$$p_i^{bias}(\theta_{i-1,i}) = C_1 e^{-\frac{lp}{2l}((\theta_{i-1,i}-\theta^1)^2+(\theta_{i-1,i})^2)/4}, \tag{5.10}$$

where C_1 ensures the normalization and θ^1 is a biasing angle. This distribution is not peaked at 0 as the one corresponding to the bending energy, but rather around a higher value of the angle (see figure 5.2 (b)), therefore the segments generated according to it will have higher bending angles. We need to correct for this bias, such that our ensemble of polymers is not influenced by it. This is done by introducing an additional weight function defined as:

$$g_j = \frac{p_i^{bond}(\theta_{i-1,j})}{p_i^{bias}(\theta_{i-1,j})}, \tag{5.11}$$

where j is the segment selected according to the external potential, as in the standard technique, from the set generated through the additional bias. The the total weight function of the polymer is product of the individual weight functions of each segment:

$$G(new) = \prod_{j=1}^{n} g_j. \tag{5.12}$$

The final acceptance rate is now written as:

$$acc(old \rightarrow new) = min\left(1, \frac{W^{ext}(new)G^{-1}(new)}{W^{ext}(old)G^{-1}(old)}\right), \tag{5.13}$$

where the Rosenbluth factors are computed in the same manner as before.

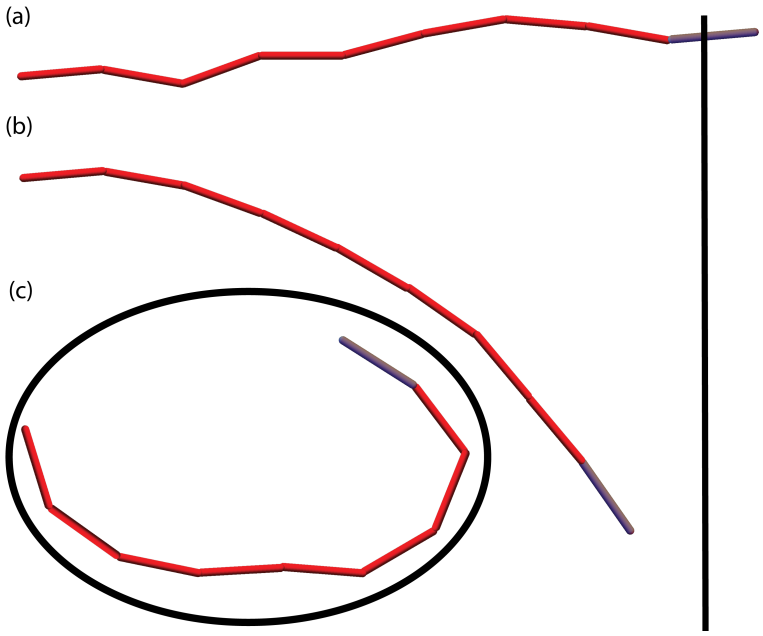

Figure 5.3: (a) Typical configuration of a polymer generated by confrontational biased Monte Carlo (b) Deflection from the wall in the modified technique (c) Highly confined polymer. In all the illustrations the gray spherocylinder represents a trial bond.

5.3 Results

Depending on the shape of the confining membrane and on the length of the cytoskeletal polymers we observe different patterns of organization for the enclosed polymers. The shape of the confining surface is fully characterized by the length of the two axis. The longest of these two axis, also called the major axis, gives the maximum distance available inside the surface. For polymers that are shorter than the major axis confining surface, which we will further call short polymers, we observe patterns characterized by straight configurations of the polymer. The polymers that exceed the length of the major axis, which we call long polymers, form more bent patterns. The asymmetry of the confining surface is essential for the formation of the the of non-trivial patterns such as planar asters, bundles or confined circles.

5.3.1 Short polymers

The short polymers are have enough space to fit inside the confining surface without bending. Bending costs energy, and their most energetically favorable state, neglecting the thermal fluctuations, is a straight rod. Unless there are other forces at play, the polymer is unlikely to bend. Therefore we expect the polymers to look for the directions inside the volume which offer them a distance at least equal to their length, similar to the organization of short rigid rod-like polymers. This is also what we observe in the simulations of confined semiflexible polymers. As a function of the length of the polymers, we find patterns characterized by isotropic organization, asters, both three dimensional and planar, and bundles.

The isotropic organization is characterized by a homogeneous distribution, both in position and in orientation, of straight polymers throughout the volume of the ellipsoid. This type of organization appears for all geometries of the confining surface provided that the length of the polymer is a few times shorter than the diameter of the confining volume (for the sphere) and shorter than the minor axis (for the ellipsoids). Figure 5.4 shows a composite of several of polymer configurations obtained for the same parameters, in the three geometries considered. The upper and lower image correspond to different projections of the same configuration.

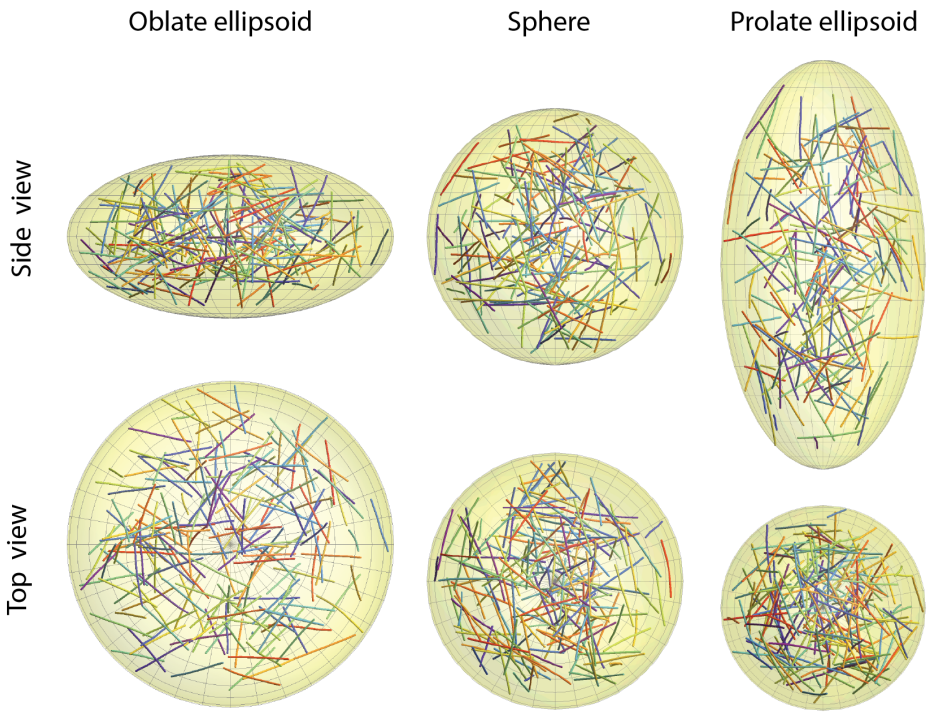

Figure 5.4: Isotropic organization of polymers in an oblate ellipsoid ($L_x = 12.6\mu m$ and $L_z = 6.3\mu m$), a sphere ($L_x = 10\mu m$) and a prolate ellipsoid ($L_x = 7.95\mu m$ and $L_z = 15.85\mu m$). All polymers have $L = 2.5\mu m$ and $D = 0.25\mu m$. Each image shows a composite of 200 polymer configurations. For convenience the polymers are shown three times as thick as their real diameter. The different color of the polymers is used to better distinguish them and it is not correlated with any other quantity. The three surfaces presented enclose the same volume, the representations being shown to scale.

Irrespective of their length, in the sphere geometry the polymers have isotropically distributed orientations but, as their length approaches the diameter of the sphere they tend to be more and more confined to the diameter. As a result, all polymers cross the central region of the sphere, their overlap resembling a three dimensional aster (see figure 5.5). As the length of the polymers is closer to the diameter the aster is better localized,

the intersection volume being smaller.

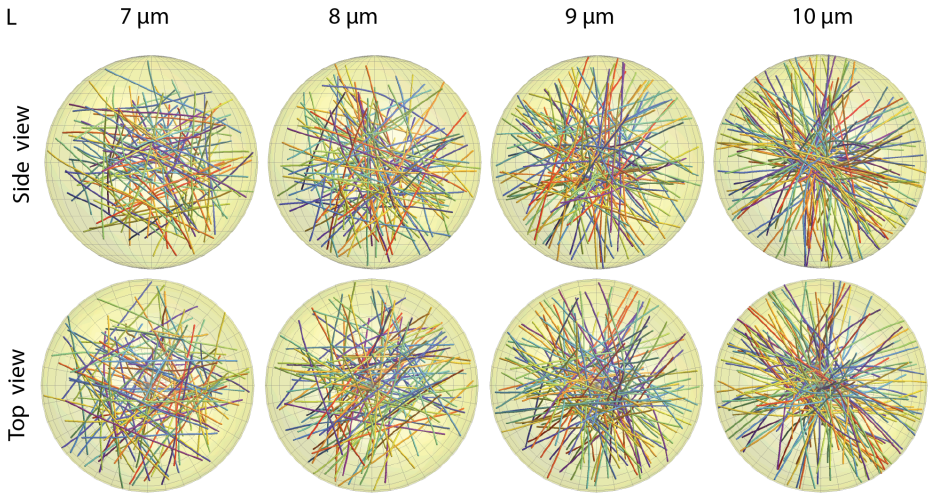

Figure 5.5: Three dimensional aster configurations for different polymer lengths confined in a sphere of diameter $L_x = 10\mu m$. The images show a composite of 100 configuration.

In the ellipsoid geometry, the asymmetry starts playing a role when the polymers become longer than the minor axis. At this point the direction of the minor axis becomes unfavorable, since the polymers would have to bend in order to fit along it. This creates an anisotropy in the polymer orientation. As the polymers become longer the directions offering enough length for the polymer to fit straight inside the confining surface become more and more confined around the major axis. In the prolate geometry the polymers follow more the the major axis as their length becomes closer to the length of this axis, their angle with the axis decreasing. This effectively results in a bundle-like structure (see figure 5.6). The diameter of the bundle decrees as a the polymer length increases. In the oblate geometry, the maximum distance available is no longer offered by a single direction as it is the case in the prolate ellipsoid, but by a full plane: the equatorial plane. There is no preference in orientation along any of the diameters of the equatorial plane. Polymers longer than the minor axis will be forced to align more and more to this plane as their length becomes closer to the

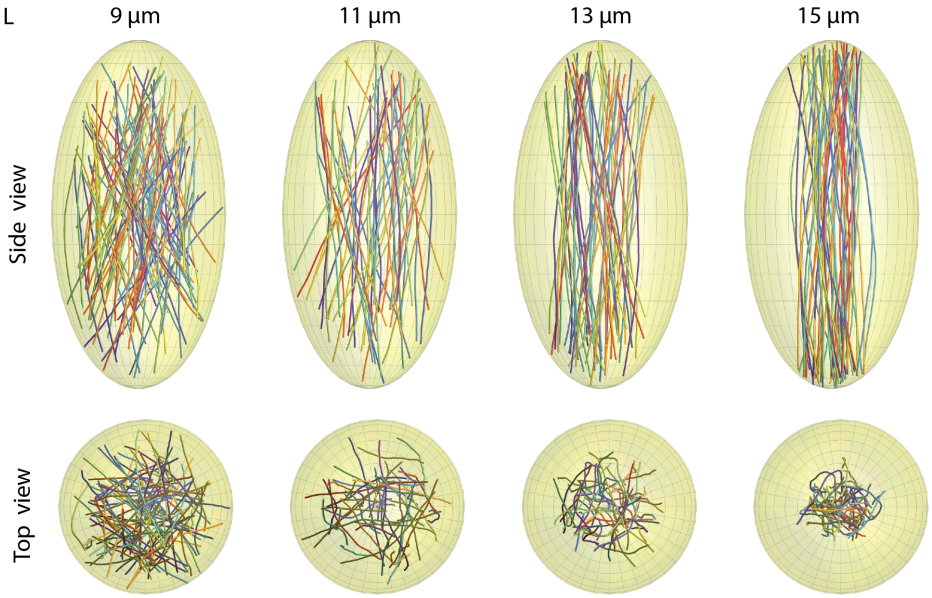

Figure 5.6: Bundle organization in an prolate ellipsoid ($L_x = 7.95\mu m$ and $L_z = 15.85\mu m$) for various polymer lengths. Each image is a composite of 100 polymers.

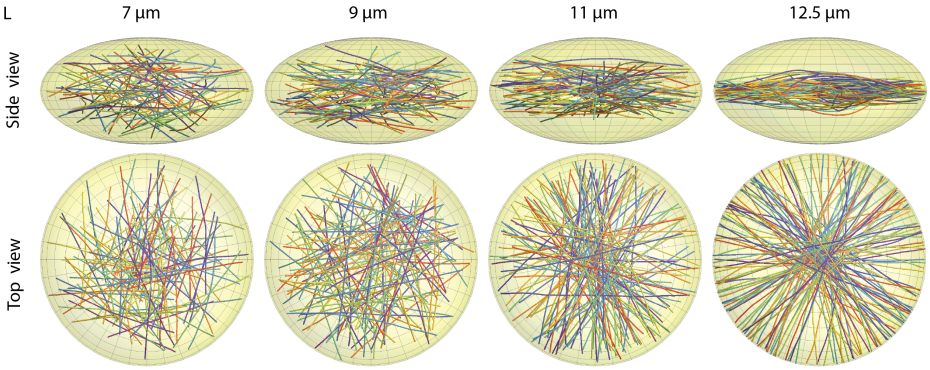

Figure 5.7: Planar aster in an oblate ellipsoid ($L_x = 12.6\mu m$ and $L_z = 6.3\mu m$) for different lengths of the enclosed polymers, showing a composite of 100 configurations.

major axis until they are fully confined to this equatorial plane. The polymers form an almost planar aster as whose thickness decreases as $L \to Lx$ (see figure 5.7).

To gain insight on the organization of the polymers we compute the tensor order parameter for a fixed polymer length L and a fixed shape of the confining surface characterized by the asymmetry λ. This quantity is can be computed as an average over the ensemble of polymers of length L enclosed by one particular surface. We typically use ensembles 10^4 different polymer configurations with their respective weight for determining the overall tensor order parameter as well as for the another quantities computed in the rest of this section. This tensor can be written as average over the polymer ensemble as follows:

$$\mathbf{Q} = \frac{1}{n} \left\langle \sum_{i=1}^{n} \left(\frac{3}{2} \hat{\mathbf{u}}_i \otimes \hat{\mathbf{u}}_i - \frac{1}{2} \mathbf{1}_3 \right) \right\rangle, \tag{5.14}$$

where $n = L/l$ is the number of segments of length l composing our semi-flexible polymer, $\hat{\mathbf{u}}_i$ the orientation of each segment and $\mathbf{1}_3$ the 3×3 unit matrix. Its highest eigenvalue Q represents the degree of order and the corresponding eigenvector $\mathbf{n}$ gives the direction along which the polymers are oriented on average. For an ensemble of straight polymers all aligned in the same direction the parameter $Q = 1$ whereas for an isotropic pattern $Q = 0$. In plane isotropic organizations are characterized by two highest eigenvalues both equal to $Q = 0.25$.

The organization in the spherical geometry, irrespective of the length of the polymers, is characterized by the lack of order, $Q = 0$, (see figure 5.8 (a) and (b)). A small variation in the asymmetry of the surface induces spontaneous organization of the enclosed polymers. For the oblate geometry ($\lambda < 1$) as the polymer exceeds in length the minor axis, the order parameter Q converges to 0.25 (see figure 5.8 (a)), its other two eigenvalues being 0.25 and -0.5. This indicates an in-plane organization, where the polymers have no apparent order within the planar phase. For $\lambda > 1$, which corresponds to the prolate enclosing surface, the polymers start aligning to each other as a function of L and become fully parallel as $L \to L_z$ (see figure 5.8 (b)).

The preferential direction of alignment is different for the three types of shapes considered. In figure 5.8 panels (c) and (d) we show the length of the projection of the unit orientation vector $\mathbf{n}$ on the xy-plane n_{xy} and

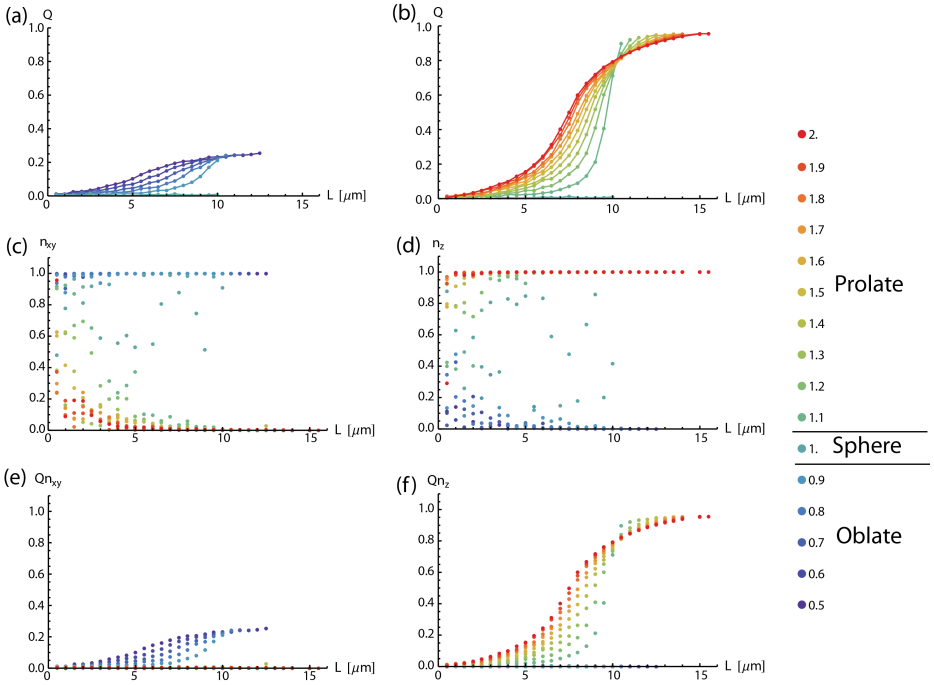

Figure 5.8: Degree of order and orientation of polymers of different length for different asymmetries of the confining surface (color scale the right hand side) as a function of polymer length L. All the confining surfaces enclose the same volume, $\lambda = 1$ corresponding to a sphere of diameter $L_x = 10\mu m$. Top row shows the degree of order as a function of the length for oblate confining ellipsoids (left) and prolate ellipsoid (right). In the middle row we display the projection on the xy-plane n_{xy} (left panel) and z-projection n_z (right panel) of the of the orientation $\boldsymbol{n}$. The last row presents the product between order Q and the n_{xy} (left) and n_z (right) projections.

of its z-projection (n_z) respectively. In the sphere geometry both these projection show no trend, being randomly distributed. The polymers enclosed in a surface with $\lambda < 1$ (oblate), if long enough, orient along the xy-plane, whereas for $\lambda > 1$ (prolate) they align to the z-axis. These two directions correspond to the maximum distance available in the considered geometry.

In both the prolate and the oblate geometry the shorter polymers exhibit a orientation pattern similar to the sphere case. In order to see trends in the in the orientation we need to correlate the degree of order to the direction of orientation. In figure 5.8 ((e) and (f)) we show the product between order and the considered projections of the orientation. We see that alignment along the xy-plane arises in the oblate geometry and z-aliment in the prolate.

The tensor order parameter gives information about the overall orientation of the polymers but does not characterize the local patterns. It gives, for example, the same result for a random isotropic organization and for a three dimensional aster, these two types of organization being indistinguishable if only this parameter is considered. To gain more insight into the polymer organization, a measure of local polymer density is required. We chose to use the average length of the polymer enclosed between two parallel planes that are perpendicular to one of the coordinate axis and denote this length by l_x, l_y or l_z, according to the axis on which the sectioning planes are perpendicular. We divide the volume of the ellipsoid by equidistant panes with a width of $\approx 0.25\mu m$. This type of measure has the advantage that it can be directly related to the experimental data: the imaging of droplets enclosing cytoskeletal polymers is usually done by confocal microscopy, the resulting data being a collection of planar images containing single optical sections of the droplet along one axis. The total fluorescence in each slice is directly proportional to the polymer length comprised in the respective slice.

In the spherical geometry, the average length of the polymer, for polymers several times shorter than the diameter, is the same for all the slices (see figure 5.9). This indicates a isotropic distribution of the center of mass of the polymers. As the polymer becomes longer its length in the central region of the droplet increases and, as the polymer approaches the diameter in length, a peak in the average length can be observed in this region. The center of mass of the polymer becomes confined in an increasingly small region around the center as its length grows. This density profile matches an aster configuration since all polymers cross the central region (corresponding to the peak) and splay out towards the exterior resulting in a lower average length in the peripheral sections. The profiles corresponding to sections along the three coordinate axis exhibit the same features implying that the structure is fully symmetric around the center of the droplet.

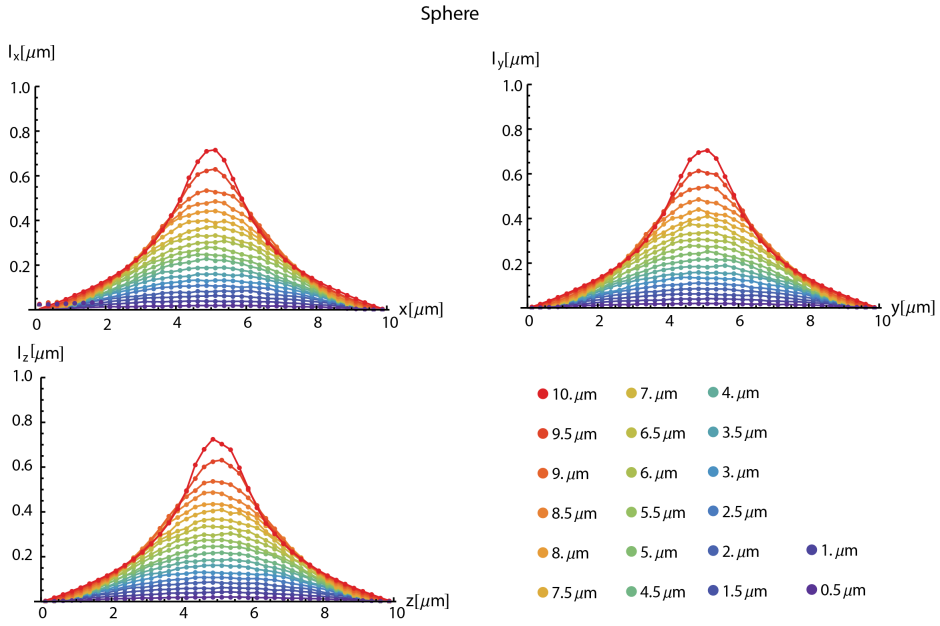

Figure 5.9: Average length of the polymers in sections, corresponding to each of the three coordinate axis, through a sphere of $L_x = 10\mu m$. The different color of the curves codes the length of the polymer L.

Polymers shorter than the minor axis enclosed in an oblate ellipsoid exhibit profiles similar to the the ones enclosed in a sphere. Above this length the polymer l_x and l_y profile remain similar to the sphere case but l_z exhibits a hight peak in the central region of the droplet, around which the length density is zero. The with of the peak decreases with L. This shows that most of the polymers are confined in a thin slice in the equatorial region. The observed profiles are consistent with a planar aster located in the xy-plane.

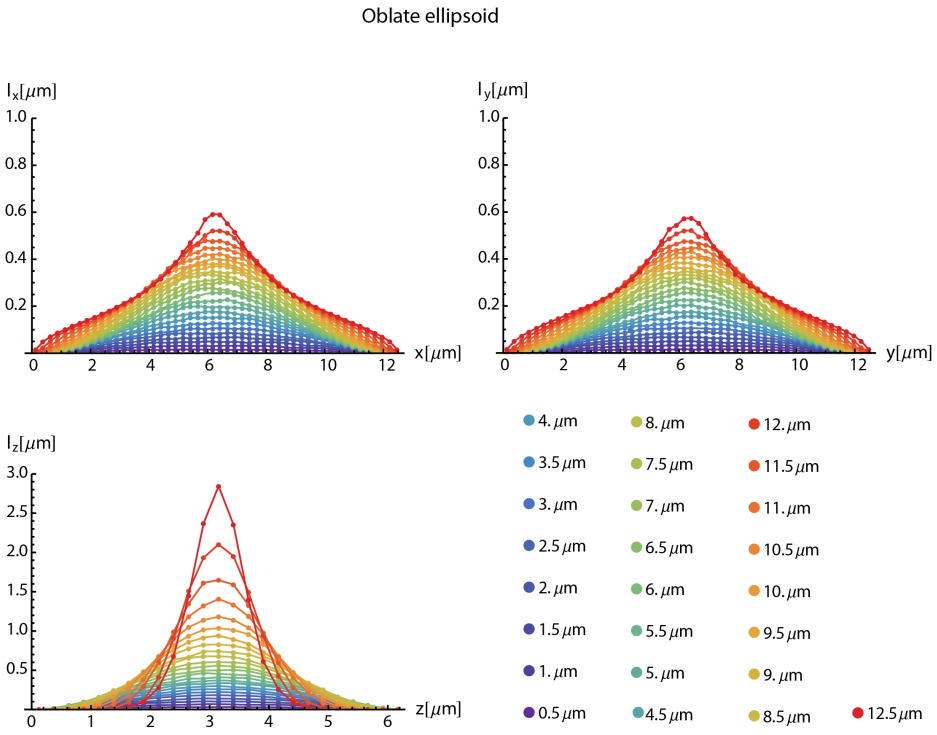

Figure 5.10: Average length of the polymers in sections, corresponding to each of the three coordinate axis, through an oblate ellipsoid with $L_x = 12.6\mu m$ and $L_z = 6.3\mu m$. The different color of the curves codes the length of the polymer L.

In the prolate geometry the the profiles for l_x and l_y show a similar behavior to the l_z profile for the oblate indicating a packing of the polymers in the middle of the xy-plane. For $L > L_x$ the the average length l_z becomes constant throughout almost all the domain, its value matching the the separation distance in between the sectioning planes. This indicates that the polymer is parallel to the major axis. These average length profiles are coherent with a bundle organization along the z-axis.

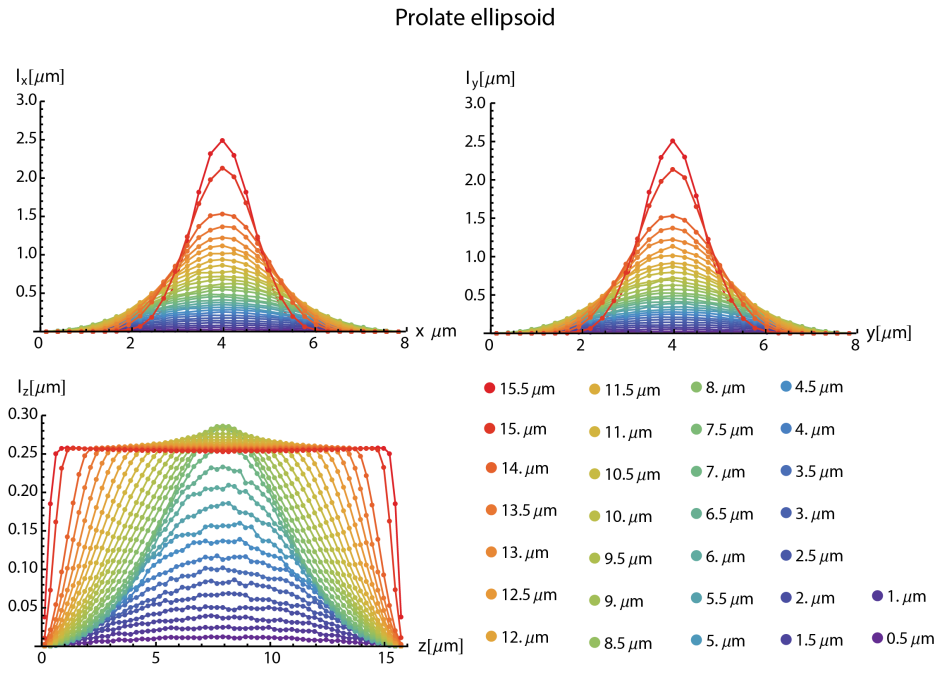

Figure 5.11: Average length of the polymers in sections, corresponding to each of the three coordinate axis, through an prolate ellipsoid with $L_x = 7.95\mu m$ and $L_z = 15.85\mu m$. The different color of the curves codes the length of the polymer L.

5.3.2 Long polymers

When polymers become longer then the maximum distance available inside the confining volume, they are forced to bend. In a sphere, the maximum distance available is along a diameter. Polymers exceeding in length the diameter are forced to bend away from it (see figure 5.12). If the length of the polymers is not much higher than L_x, it appears that both its ends remain in contact with the surface at points situated on the same diameter. In a sphere, there is no a priori preference for any diameter, therefore the bent configurations are isotropically distributed. As L approaches $(\pi/2)L_x$ the polymer touches the confining surface over most of its length, its cur-

vature becoming closer to the one of the surface. For $L \to \pi L_x$ we observe the formation of rings just beneath the surface. All these bent configurations leave the middle of the droplet free consistent with the experimental observations [123].

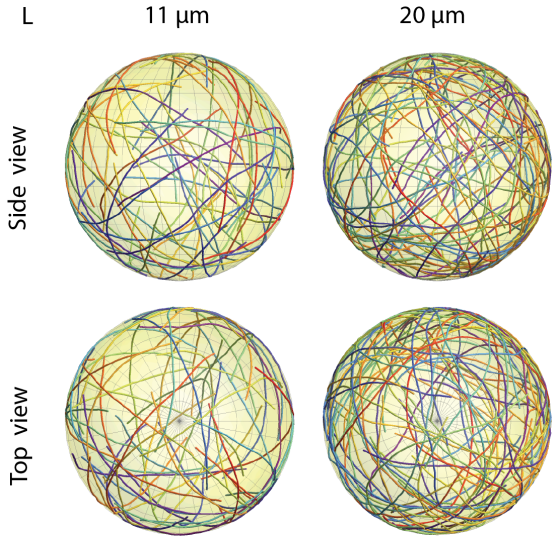

Figure 5.12: Representative organization for different polymer lengths confined in a sphere of diameter $L_x = 10\mu m$. The images show a composite of 50 configuration.

In the prolate geometry the maximum distance available is given by the major axis of the ellipsoid. For polymers with $L > L_z$ we first see, as a function of L, a bending away from the major axis, the end of the polymer remaining close to the end point of this symmetry axis. The overlay of multiple such configurations results in a bipolar structure 5.13. For longer polymers we observe the formation of elliptical rings. The polymers that are shorter than the perimeter of the ellipse having the same major and minor axis as the ellipsoid do not organize entirely following this ellipse. Depending on their length the polymers pick an ellipse (or part of an ellipse) with perimeter at most equal to their length which has the higher curvature radius since that leads to minimum bending energy. They try to exploit the less curved of parts membrane located around the equatorial plane but

try to avoid the highly curved zones around the poles, organizing on ellipse which have the minor axis the same as the confining ellipsoid but a shorter major axis. These curves have a lower average curvature. This elliptical ring does not necessarily have to be in the plane of the major axis, since there are more directions inside the ellipsoid offering sufficient space.

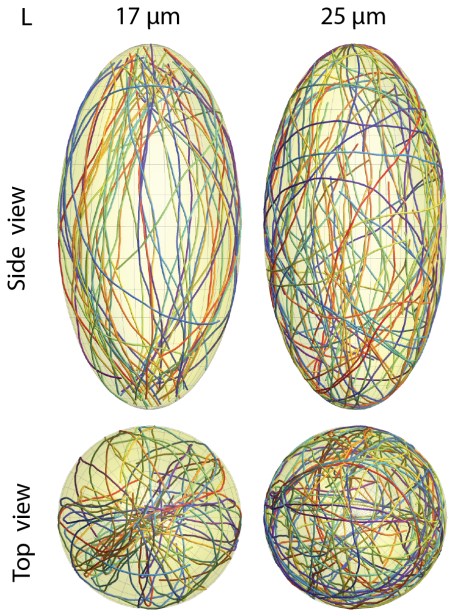

Figure 5.13: Representative organization for different polymer lengths confined in an prolate ellipsoid ($L_x = 7.95\mu m$ and $L_z = 15.85\mu m$). Each image is a composite of 50 polymers.

In the oblate geometry the filaments start bending out the equatorial plane as $L > L_x$, the ends laying preferentially in this plane (see figure 5.14). The two ends appear to be on the same diameter of the equatorial circle. All diameter of the this circle offer equivalent polymer configurations, leading to an isotopic distribution in the xy-plane. This type of organization also leaves an unoccupied volume in the center of the droplet. As the length increases the polymers start following the surface, ultimately forming circumferential rings. The circumferential rings are more confined in the equatorial plane as $L \to L_x$.

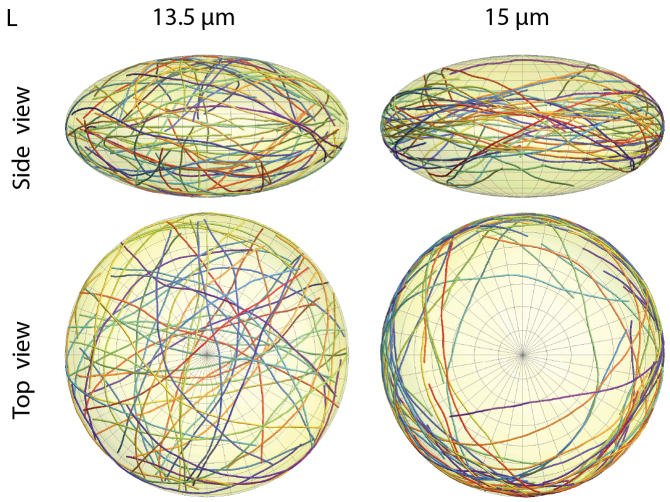

Figure 5.14: Representative organization for different polymer lengths confined in an oblate ellipsoid ($L_x = 12.6\mu m$ and $L_z = 6.3\mu m$). Images show a composite of 50 configurations.

5.4 Discussion

Using Monte Carlo simulation, we investigated the organization of confined cytoskeletal polymers as a function of their length and of the asymmetry of the confining ellipsoidal surface. We find that even small asymmetries of the membrane lead to drastic changes in the cytoskeletal organization: The three dimensional aster observed in spherical geometry becomes planar if the confining surface is an oblate ellipsoid. The homogeneously distributed circumferential rings formed for long polymers confined in a sphere collapse on top of each other as $\lambda < 1$. In prolate confinement, we find single bundles and bipolar structures, which are not observable in the other geometries. The overall type of organization does not depend strongly on the persistence length of the polymer, the minimum energy configuration being the same. For lower persistence length the thermal fluctuations are higher resulting in more configurations close to the minimum energy one being accessible.

The patterns appearing in the simulations are very similar to the ones observed in the preliminary experiments on emulsion droplets encapsulat-

ing microtubules (experiments by Sophie Roth, Marileen Dogterom Group, TU Delft) and actin filaments crosslinked with fascin (experiments by Feng-Ching Tsai, Gijsje Koenderink Group, AMOLF). Actin filaments crosslinked with fascin form bundles, and when confined in emulsion droplets, they show a homogeneous distribution in the short filament regime, a three dimensional aster for the intermediate regime, and isotropically distributed circumferential ring for long bundles. These patterns are in good agreement with our simulation results for polymers enclosed in spherical surfaces, these results being consistent with actin bundles not being stiff enough to deform the emulsion droplet. Microtubules enclosed in droplets show, besides the homogeneous distribution appearing for short filaments, single bundles, planar asters, single circumferential rings and bipolar structures. The emulsion droplets in which these pattern are observed have an ellipsoidal shape, but with only a small eccentricity. The patterns match our simulation results for oblate and prolate geometries. In the above experiments the deformation of the droplet is the result of the cytoskeleton pushing against the membrane. To address experimentally the question how the shape of the asymmetry in the membrane influences the organization cytoskeletal filaments enclosed, it is possible to externally deform the droplets by confining them in microchambers. Preliminary experiment by Nuria Taberner and Sophie Roth (Marileen Dogterom Group, TU Delft) show the patterns matching our simulation results.

We will discuss the next step of this project which is the minimization of the total elastic energy (of the membrane and the enclosed cytoskeletal polymers) in the concluding chapter.

5.5 Appendix

5.5.1 Overlap criterion of a rigid rod with an ellipsoidal surface

Since both the spherocylinder and the ellipsoidal surface that it encloses in are convex bodies, it is sufficient to check if the two end of the spherocylinder are located inside the confining surface. All points on the surface of the spherocylinder are at one radius r distance from the center line therefore the overlap criterion amounts to verifying whether the end points of this center line are at a further than one radius r below the surface. This is equivalent with checking if the two end points are inside a surface that is characterized by all its points being at a distance r from the confining surface. This type of surface is called a inner parallel body. The parallel body of a sphere with radius R is a sphere with radius $R - r$. For the non-overlap with a sphere, each of the two ends of the central line should obey the following condition:

$$pr_x^2 + pr_y^2 + pr_z^2 < (R - r)^2, \tag{5.15}$$

where pr_x, pr_y and pr_z are the projections of the end of the central line on the three coordinate axes. The parallel body of an ellipsoid is unfortunately not itself an ellipsoid, but a higher order surface. The two ellipsoids that we consider as confining surfaces are oblate and prolate which are obtained by rotating an ellipse around one of its symmetry axis. Due to this symmetry we can consider the two dimensional equivalent problem of determining the distance from a a point to an ellipse and the generalize it to three dimensions. We know that any point (x, z) of an ellipse of axis L_x and L_z obeys the following equation:

$$\frac{x^2}{(L_x/2)^2} + \frac{z^2}{(L_z/2)^2} = 1. \tag{5.16}$$

The perpendicular form a point (x_p, z_p) to the ellipse has the equation:

$$\frac{z}{(L_x/2)^2}(x_p - x) - \frac{x}{(L_z/2)^2}(z_p - z) = 0 \tag{5.17}$$

and, since we want this point to be at a distance r from the ellipse,

$$(x_p - x)^2 + (z_p - z)^2 = r^2 \tag{5.18}$$

should be true. The pair (x_p, z_p) describes the curve located at a distance r from the ellipse. Combining the last three equations results in a fourth order polynomial equation. This equation can be solved analytically, but the solutions are lengthy and complicated. Since the overlap check is done frequently in our Monte Carlo algorithm, we want it to be as efficient as possible, and using the above solutions most likely slows it down. An approximation to the parallel curve is an ellipse with semi-axes shorter with r than the ones of our initial ellipse. The equation of this curve can be written as follows:

$$\frac{x_e^2}{(L_x/2 - r)^2} + \frac{z_e^2}{(L_z/2 - r)^2} = 1. \tag{5.19}$$

For a circle ($L_x = L_z$) the curves (x_p, z_p) and (x_e, z_e) coincide. As the asymmetry increases or decreases the difference between the two curves becomes higher. For all our simulation we use a confining surface that has the same volume as a sphere of $10\mu m$ diameter, the asymmetry being between $\lambda = 0.5$ and $\lambda = 2$. In figure 5.15 we show the difference Δ between these two curves (defined as $\Delta = z_e - z_p$) for the two most asymmetric ellipses considered as a function of the x-coordinate. The plot shows the parameter Δ for various thicknesses of the spherocylinder. Microtubules have a diameter of $25nm$, which corresponds to the red line on the plot. We see that even for these very asymmetric ellipses the difference between the exact curve and our approximation is less than one tenth of the radius of the polymer. Compared to the size of the droplet these variations are negligible. We can therefore consider that the two ends of the center line spherocylinder should be inside the ellipsoidal surface obtained by rotating the curve (x_e, z_e). Checking if the spherocylinder overlaps with the ellipsoidal confining surface amount to verifying that each end of the center line of the spherocylinder satisfies the following inequality:

$$\frac{pr_x^2 + pr_y^2}{(L_x/2 - r)^2} + \frac{pr_z^2}{(L_z/2 - r)^2} < 1. \tag{5.20}$$

Note that, for a sphere the above relation becomes exact.

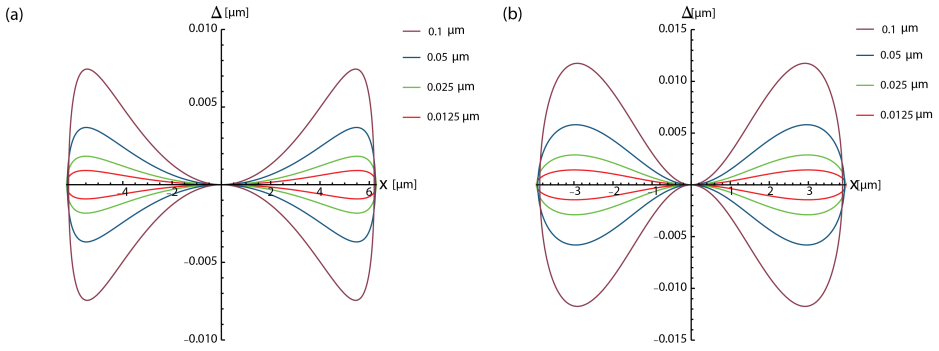

Figure 5.15: Difference between the exact solution for the inner parallel curve of an ellipsoid and the approximative solution (a) for an ellipse corresponding to the oblate ellipsoid ($\lambda = 0.5$, $L_x = 12.6\mu m$ and $L_z = 6.3\mu m$) (b) and for an ellipse corresponding to the prolate ellipsoid ($\lambda = 2$, $L_x = 7.95\mu m$, and $L_z = 15.85\mu m$

6

Steric repulsion of microtubule asters

In cell division, the exact positioning of the two microtubule asters is crucial for the proper separation of the daughter cells. The positioning of a single microtubule aster is the result of the competition between the pushing forces exerted by the microtubule on the cell membrane and pulling forces due to the microtubules anchoring to the membrane through cortical motors. When two asters are enclosed in the same cellular volume their interaction leads to a spatial separation between their centers indicating an effective repulsion between them. We study the repulsion between two microtubule asters due to excluded volume interactions and find that it indeed leads to a spatial separation that depends on the density of microtubules in the asters and on their length.

6.1 Introduction

Cell division in animal cells requires the formation of a mitotic spindle which consists of two microtubule asters [69]. Each microtubule aster has a spherical ball of proteins, called a centrosome, at its core from which microtubule radiate outwards. The size and shape of the centrosome varies somewhat during the cell division cycle but, for animal cells, the shape is roughly spherical with diameter around $0.5 - 1\mu m$ [143, 144]. Interphase cells, the typical cell configuration in which the cells spend most of their time, contain usually just one microtubule aster. During cell division two asters are created by first dividing the centrosome. This separation begins at an early stage of cell division, but is fully completed only at the beginning of the so-called M-phase, with microtubules growing out of the both centrosomes. At this stage each chromosome has already duplicated, the cell now containing two copies of the DNA. The nuclear envelope is then disassembled and microtubules capture the chromosomes. In order that division happens properly, the centrosomes need to move to opposite ends of the cell creating the poles of the spindle. Then the chromosomes, which are now all attached to microtubules growing from both spindle poles, need to be be placed in the midplane between the poles, which is again a microtubule dependent process. Once aligned in the middle plane, the chromosomes are pulled by microtubules towards the poles, separating the duplicated genome into two identical daughter genomes. Once in position, the nuclear envelope is reassembled around the daughter genomes. The division cycle continues with the assembly of a contractile acto-myosin ring in the plane perpendicular to the middle of the axis between the two poles, which subsequently cleaves the daughter cells apart.

Throughout the division process the precise positioning of the two microtubule aster is crucial for creating functional daughter cells: it ensures the proper separation of the genetic information and determines the position where the cells will separate [116]. Studying the positioning of microtubule asters in cells is challenging since it is the combined effect of individual microtubule dynamics, the interaction of the asters with the membrane, which acts as a confining space, but also attaches microtubules via motor proteins. In addition to this, motor proteins in the cytoplasm, the so-called cytoplasmic motors, also contribute to the positioning of the spindle poles [145]. To understand the mechanics underlying aster positioning and the relative importance of each of the contributing factors, it is

useful to use a bottom-up approach, first reconstructing a minimal system and progressively adding more complexity to it. The first step in understanding spindle positioning is finding what parameters are relevant for the positioning of a single confined microtubule aster. To study effect of confinement on a microtubule asters *in vitro* assays using microchambers and emulsion droplets are employed to mimic real cells [146, 147, 48, 123]. Both these assays offer rigid confining volumes: microchambers have hard walls and the stiffness of the oil, in which the drops of buffer solutions containing the aster are immersed, can be high enough that the lipid monolayer is not deformed by the microtubules enclosed by it. The rigid walls therefore allow to isolate the effect of a predefined shape of the confining volume, without considering the membrane deformations (which occur in vesicle). As already mentioned, the positioning of a confined aster is based on microtubule dynamics. Microtubules are dynamical polymers, alternating phases of growth and shrinkage. Growing microtubules generate a pushing force [27, 148], while shrinking microtubules can exert pulling forces[149, 150]. When enclosed in an emulsion droplet, growing microtubules will exert a pushing force against the membrane, and the shrinking ones will pull on the membrane provided they are attached to cortical motors (see figure 6.1). The positioning of the aster is the result of the balance between these forces and depends on the distribution of the microtubules at the cortex. The cortical distribution is also influenced by microtubules sliding along the membrane. These mechanisms together lead to the robust centering of the aster [68, 151]. If no cortical motors are present and hence pulling is absent, the centrosome is typically driven to the boundary of the droplet.

The next step towards reconstructing a spindle *in vitro* is confining two microtubule asters in the same emulsion droplet. Experiments by Dr Sophie Roth (group of Prof Dr Marileen Dogeterom, TU Delft), with whom we are collaborating on a project out of which the work in this chapter is part, have shown that a distinct spatial separation between the two centrosomes always occurs. In the absence of cortical motors, the two centrosomes are pushed to the cortex. This is consistent with the single aster case. When motor are present, pulling contributes to centering of the asters. Naively, we would expect that the two centrosomes are both found in middle of the droplet, in contrast to the experiment. This leads us to believe that, in addition to the centering mechanism known from the confined single aster, there is also a repulsive force in between the two asters that contributes to

the positioning. Since microtubule asters are spatially extended objects, we hypothesize that this repulsion is the result of steric repulsion. Therefore we study the repulsion between two microtubule asters due to excluded volume interaction between the component microtubules.

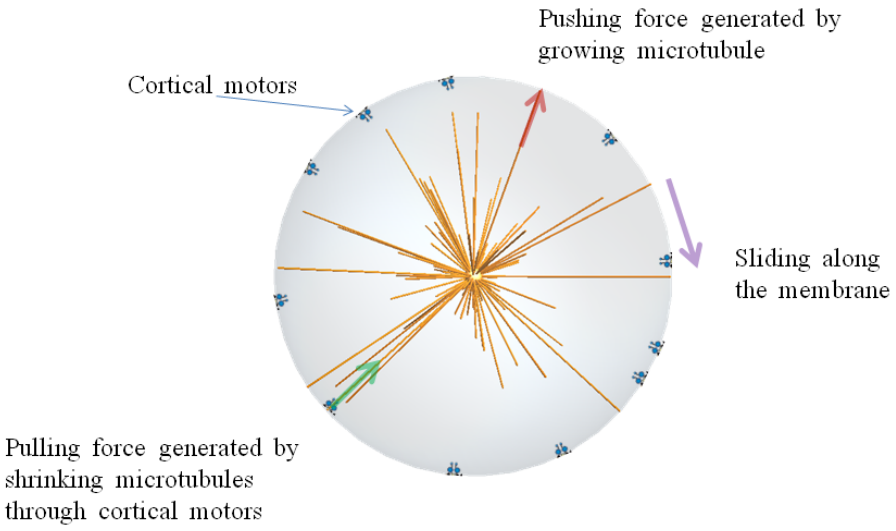

Figure 6.1: Illustration of the main mechanisms involved in centering of a confined microtubule aster.

6.2 Steric repulsion

Geometrically a microtubule aster can be described by a sphere of radius R representing the centrosome and a number of N tube-like objects radiating out of it which correspond to the microtubules. Since the persistence length of the microtubules is two orders of magnitude higher than the typical diameter of the emulsion droplets used in the experimental work on which this chapter is based, their behavior can be well described by a rigid rod. We therefore represented the microtubules by spherocylinders of diameter D and length L with one end embedded in the centrosome.

The positioning of the two asters inside the confining surface is the result of balance between the centering (induced by pulling and pushing

forces) and the mutual repulsion. Both pushing and pulling are the result of microtubule-membrane interaction. However, the repulsion involves only the two asters. In order to interact the two asters need to be close enough so they can touch each other. This occurs only in the lens-shaped volume resulting from the intersection of the bounding sphere of the two asters (see figure 6.2 (b)). For an aster we define the bounding sphere as the imaginary spherical surface constructed around the center of the centrosome having a radius $R_b = L_{max} + R$, where L_{max} is the length of the longest microtubule in the aster. The lens shaped volume is located in the region between the asters, away from the surface. The aster-membrane interaction and the the aster repulsion can be therefore decoupled. We therefore study the repulsion between the two aster in bulk, without considering the full system which includes the membrane (see figure 6.2 (b)).

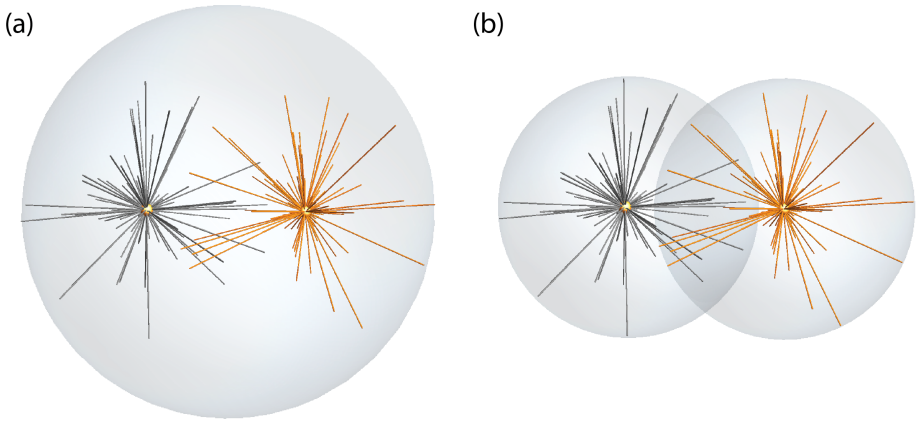

Figure 6.2: (a) Illustration of two asters confined in a spherical volume. (b) Interaction volume of the two asters given by the intersection of their bounding spheres.

6.2.1 Potential of mean force

Steric repulsion is due to objects occupying a certain amount of volume. Around the center of mass of an object there is a excluded volume in which the center of mass of another particle can never been found. The simplest example is the case two identical spherical objects of radius R_s. Their ex-

cluded volume is given by a sphere with the radius $R_{excl} = 2R_s$, which amounts to 8 times the volume of a single sphere. For other particles, such as spherocylinders, it is also possible to compute this volume analytically [152]. Unfortunately the asters described above are too complex geometrical objects to allow an analytical calculation of their excluded volume. A numerical approach to calculate the excluded volume is based on the Monte Carlo technique. The strategy is the following: by keeping one object fixed and repeatedly trying to insert the other object, the trial positions of its the center of mass being homogeneously distributed in in a volume V around the center of mass of the other object, the number of successful trials n_s are counted. A trial insertion is successful when the two objects do not overlap. The number of successful trials over the total number of trials n_t is equal to the excluded volume V_{excl} over the total volume ($n_s/n_t = V_{excl}/V$).

Since our aster in complex concave body the total excluded volume calculated by the above described method does not offer so much information. Unlike for the case of two hard sphere, where the interaction potential is infinite inside the excluded volume sphere and zero outside, the potential for asters will be a function of the distance between the centers of mass. The microtubules splay out away from the centrosome, effectively leaving more free volume between them, allowing for more possible insertions of the other aster. Effectively the repulsion decreases as a function of distance, behavior which is closer to a soft, deformable, particle than to a hard one. Polymer coils are also highly complicated non-compact geometrical objects interacting by steric repulsion. They can also be effectively modeled as soft particles, their pair potential as a function center of mass separation distance being calculated through a Monte Carlo technique similar to the one used for excluded volume estimation [153]. The idea is to insert the object at a certain distance d from the center of mass of the other object and count the overlaps at this particular distance. Repeating this procedure for different separation distances allows to determine the insertion probability as a function of distance $p(d)$. The insertion probability can be related to the potential of mean force via the simple relation:

$$U(d) = -k_B T \ln[p(d)], \tag{6.1}$$

where k_B is the Boltzmann constant and T the temperature [66]. From this effective potential the repulsion force $F(d)$ can be obtained by differ-

entiating with respect to the separation distance d:

$$F(d) = -U'(d). \tag{6.2}$$

6.2.2 Numerical effective potential estimation

Using the Monte Carlo method described in the previous section we set out to compute the effective potential due to steric repulsion as a function of the separation between the center of mass of the two asters. We take the radius of the sphere representing the centrosome $R = 0.25\mu m$, consistent with the experiments according to which we construct our model. Rigid microtubules of diameter $D = 25nm$ are homogeneously distributed around the centrosome. We consider two types of aster depending on the length distribution of the microtubules: one with equal length microtubules, which we call a monodisperse aster, and one where the microtubules are exponentially distributed, characterized by a mean length L_m (see figure 6.3). Notice that the aster having an exponential distribution of microtubule lengths has a much lager bounding sphere due to a few long microtubules, but is less dense than the monodisperse one. Considering monodisperse asters is a simplification of the real situation where microtubules have an exponential length distribution [105], but provides a useful reference case. To determine the insertion probability we keep one aster fixed and insert another one with the same characteristics– same number of microtubules, distribution and length– at points homogeneously distributed on the surface of a sphere with radius d. The trial aster is also rotated prior to insertion. We count the number of overlaps ($n_{overlap}$) and compute the insertion probability as $p(d) = 1 - n_{overlap}/n_t$, where n_t is the total number of trial insertions (typically $n_t = 10^6$). The insertion probability depends on the particular realization of the two asters, we therefore repeat the calculation for 10 pairs of different asters, estimating the errors.

As a function of separation distance between the center of mass of the two asters, the insertion probability starts at zero for low d, corresponding to the inaccessible volume, then gradually increases to 1, where all insertions are successful (see figure 6.4). For monodisperse asters the increase in microtubule number, at the same L, extends the inaccessible volume, the curve becoming much steeper. As the aster becomes denser the profile resembles a step function, which corresponds to the insertion probability for two hard spheres. In this regime, the asters effectively behave as two

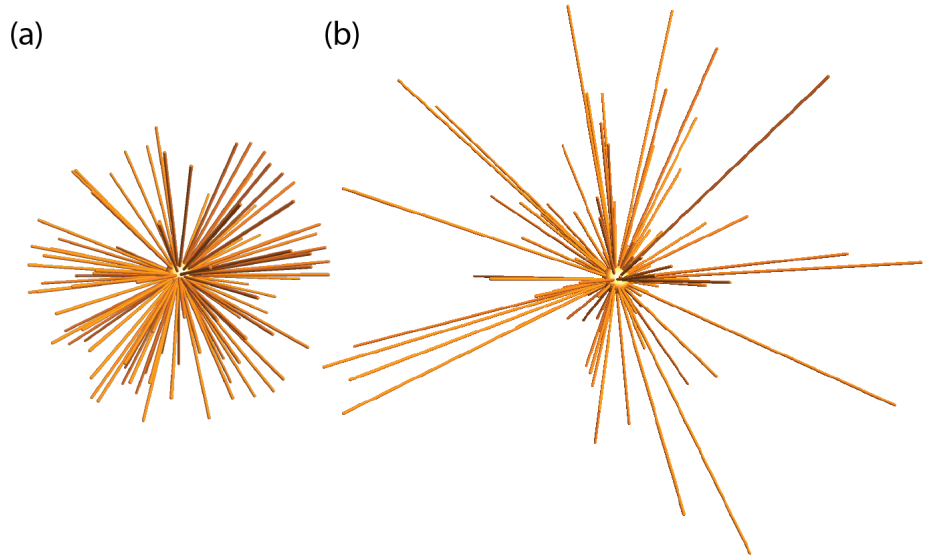

Figure 6.3: Illustration of monodisperse aster with $L = 2.5\mu m$ (a) and of an aster with microtubules having an exponential length distribution (with mean microtubule length $L_m = 2.5\mu m$) (b). The centrosome is depicted in yellow and the microtubules in orange. Both aster contain the same number of microtubule $N = 100$ and are drawn to scale.

spheres of radius $L + R$: the microtubules are so closely packed that the space between the is not sufficient for the microtubules of the other aster to fit into it. For the asters with exponential length distribution the profiles are less steep and inaccessible separation distance shorter (see figure 6.4 (b)). This is due to the shorter microtubules in one of the asters which leave directions open for the longer microtubules in the other aster, facilitating interdigitation. Note also that the interaction extends over a larger distance due to the few long microtubules. The error bars are larger for the asters with exponential length distribution, since there is more variability between the different realizations. The increase in microtubule length leads to a lees abrupt curve for the insertion probability and to an higher inaccessible separation distance (see figure 6.4 (c) and (d)). However, the separation distance represents a lower fraction of the radius of the bounding sphere of the aster as the length of the microtubules grows. This can be understood

as the microtubules splay out towards the exterior of the aster. For the same microtubule density there is effectively more free space in between the microtubules in the bigger asters. All the results show a much larger inaccessible volume than just the one given by the two centrosomes which corresponds to a sphere of radius $2R$.

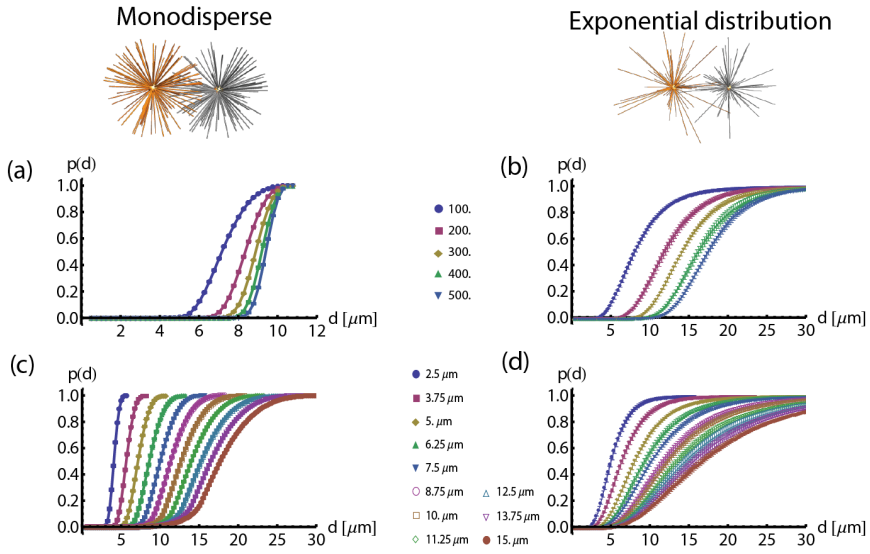

Figure 6.4: Insertion probability as a function of separation for monodisperse asters– panels (a)and (c)– and asters with exponentially distributed length of the microtubules–panels (b) and (d). (a) and (b) show different number of microtubules N for the same microtubule length $L = 5\mu m$ or mean length $L_m = 5\mu m$. Panels (c) and (d) present the results for different microtubule length or mean length, respectively for asters containing $N = 100$ microtubules. The error bars for the monodisperse asters are smaller than the symbols.

The effective repulsion potential determined from the insertion probability is shown in figure 6.5. Bellow a certain separation distance all the curves go asymptotically to $+\infty$. This vertical asymptote marks separation distance d_h bellow which the interactions become hard. The effective potential shows that the two asters can be effectively described by a spherical rigid

core of radius $d_h/2$ from which the microtubules grow. For monodisperse asters a shoulder-like structure can be observed in the effective potential at $d \approx L + 2R$ (see figure 6.5 (c)). This is the effect of excluded volume interaction between the microtubules and the centrosome of the other aster. For dense asters this feature in not observable, since in this regime most of the overlaps occur in between microtubules, the microtubules rarely reaching the other centrosome. The repulsion force computed from the effective potential for $d > d_h$ is lower than a 1 pN. Compared to the centering forces which were estimated to be in the order of 100 pN [68, 151], the contribution of this part of the effective potential is negligible.

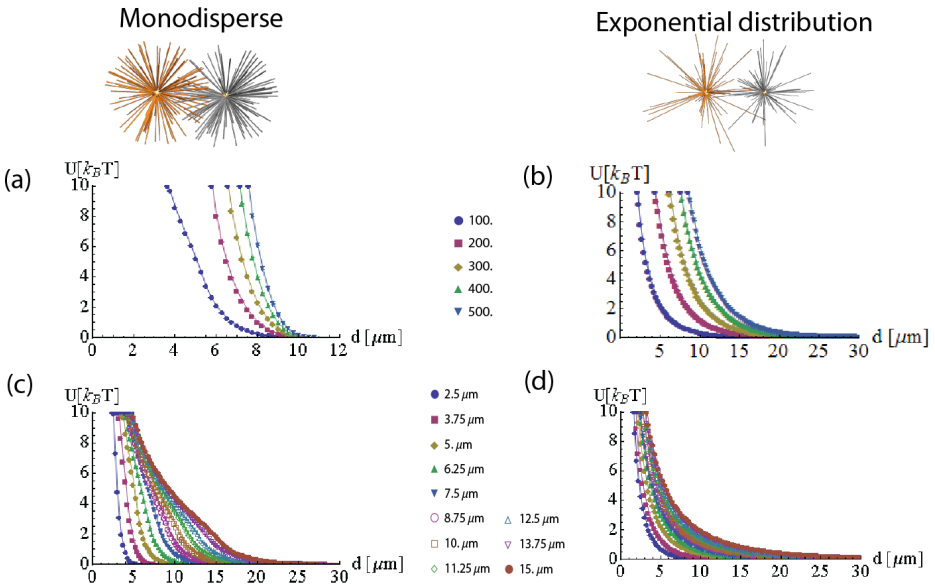

Figure 6.5: Effective potential as a function of separation for monodisperse asters– panels (a)and (c)– and asters with exponentially distributed length of the microtubules–panels (b) and (d). Parameters are the same as for figure 6.4.

6.3 Discussion

We investigate the positioning of two microtubule asters enclosed in the same spherical volume due to steric repulsion. Since the interaction volume of the two asters is located away from the membrane the steric repulsion can be determined without considering the confining surface. Using a Monte Carlo technique, we compute the effective repulsion potential between the two asters, finding that there is a minimum distance of approach of the two asters. Above this distance the interaction is weak compared to the centering forces. In confinement, in the absence of pulling forces, we expect to find the asters on the boundary. When pulling is also present we predict that the asters will position themselves in the central region, separated by a distance which depends on the number of microtubules and on their average length. This behavior is consistent with the experimental evidence. This hard repulsion due to the effective core is probably not the only repulsion mechanism. The microtubules are likely to exert pushing forces on the core of the other aster increasing the separation. Furthermore the presence of an hard aster core could influence the number of microtubules from the other aster reaching the membrane, thus anisotropically modulating the pushing forces. This would lead to a change in the force balance which could influence the aster positioning. This opens new exciting directions in investigating positioning of confined asters.

7

General Discussion

In this final chapter we summarize the results obtained in the previous chapters and also put these findings in a biological context. We also give some possible new research directions that the present work opens.

7.1 Biological context

The present work tries to answer a number of open questions on how the cytoskeleton contributes to the spatial organization of cells. The cytoskeleton is involved in cellular process that lead to significant changes in the cell shape and architecture. These process are crucial for the survival of the cell. One example is cell migration where actin filaments, one of the main components of the cytoskeleton, continuously reorganize inside a flat membrane protrusion called lamellipodium [154]. There, the actin filaments are responsible for pushing the membrane forward enabling the cell to move. Another example is cell division where the correct separation of the genetic information and the proper positioning of the division plane are ensured by microtubules, the other main cytoskeletal component [116], whereas actin filaments constructs a ring which separates the daughter cells [23]. The precise mechanisms underlying these two processes and the role played by the cytoskeletal polymers is still poorly understood.

Cells are exquisitely complex systems with a lot of processes taking place simultaneously. Isolating one single process and studying the role of each component *in vivo* is thus experimentally challenging. One way to gain more understanding into the role of cytoskeleton in the spatial organization of the cell and studying its interactions with other cell components is the bottom-up approach, which involves reconstructing a minimal system and progressively adding more complexity. Reconstructed systems such as microchambers, emulsion droplets and liposomes offer the possibility of studying the behavior of cellular components such as the cytoskeleton in a controlled environment.

7.2 Rigid confinement

One of the first questions that arises is how the cytoskeletal polymers deal with confinement, since this factor is always present in the cell: the cellular volume is separated from the outside environment by an envelope that forces the cytoskeleton to organize inside of it. Plants have rigid walls, whereas animal cells have a deformable membrane. The simplest reconstructed system to study cytoskeleton confinement is a fully closed microchamber with planar walls. Experiments on actin filaments in such *in vitro* assays show that, provided the density is high enough, the filaments

follow the walls, but also self-align along the longest distance available inside the confining volume [42]. This type of confinement would mimic well the confinement inside a lamellipodium.

7.2.1 Planar confining walls

Inspired by these experimental findings,we investigate, in Chapter 2, the organization of rigid filaments confined is a slab-like geometry. Our choice to model the actin filaments as rigid is based on the relative size of the the lamelipodia comped to the actin persistence length. The filaments are long compared to the chamber hight precluding out of plane rotation. We modeled this system as a confined liquid crystal. Using Monte Carlo simulation of rigid rods we find that the organization of the liquid crystal is the results of the two competing alignment tendencies: on the one hand particles align to the walls and on the other hand they tend to self align. At low particle densities the former contribution is dominant, whereas in the high density regime the self-alignment becomes significant. In the intermediate regime these two tendencies compete the particles following all the four side walls, but also creating a nematic phase along one of the diagonals of the container. This alignment competition leads to the to the formation of wall defects on the other diagonal, this being the first observation of such a defect structure. The nematic phase forms at lower densities than we would expect from the bulk simulations. We therefore construct a Onsager-like toy model to understand this density decrease. Our results suggest that confinement lowers the transition density, which is partially compensated by the presence of the defect structures.

Our findings show that, in confinement, the organization of rigid rod-like mesogens, such as actin filaments confined in lamelipodia, is the result of a competition between wall alignment and mutual alignment. For actin filaments polydispersity is likely to smoothen out the wall defects. However, from a liquid crystal perspective, the defect walls are relevant in the context of continuously shrinking display pixel sizes. It would be interesting to to address the question whether this kind of wall defect structures appear in other confining geometries featuring planar wall. The pattern we observed is symmetric along the diagonals which leads us to believe that in a triangular container — half of our square one — the defect wall should still be present. It would be also interesting to study how characteristics of this wall such as its length is influenced by the opening angle of

the triangular container, if the structure is present in this geometry. This could open new perspectives for investigating the organization of nematics in containers with higher order polygons as base.

7.2.2 Curved confining walls

Adding more complexity to the system, in Chapter 3, we study the effect of a curved wall on the organization of confined rigid filaments. We find find that the mesogens form the bipolar pattern expected from topological arguments. The location of the point defects can be controlled by varying density or the length of the particles. The location of the defect points ranges from inside the container at a finite distance to the wall, to defects located outside the container, similar to the virtual boojums for the nematic droplets [85, 100]. When in the middle of this flat cylindrical container we open a hole, changing its topology, the particles reorganize drastically: they form a number of nematic domains separated by wall structures. The number of domains depends on the length on the particles and the radius of the inner hole. In a cellular context the introduction of an excluded area inside the confining volume can be justified by the presence other cellular components that the cytoskeletal polymers are forced to grow around.

Other confining geometries with curved walls could be relevant for the organization of cytoskeletal polymers. In the divisions of animal cells a bipolar structure called a spindle is formed. The spindle is has a lens shape and inside it multiple rigid microtubules compete for space. Even if this structure does not really have a confining envelope, its shape is highly conserved. Using the same technique, the organization inside a lens-shaped container could be addressed.

7.3 Addressing confinement with a mean-field type theory

In Chapters 2 and 3 we focused on the regime in which the rigid particles are of the same order as the confining volume. The patterns observed are the result of a finite size effect. At this length scale Monte Carlo simulations are an effective tool. When particles are much smaller than the confining volume the system is well described by continuum theories, since the nematic field is expected to change over distances comparable to the

confinement. The existing continuum theories describing liquid crystals however have some shortcomings: the Oseen-Frank theory assumes a constant order parameter throughout the domain, which excludes singularities, whereas the Landau-De Gennes theory is only valid close to the isotropic to nematic transition. In Chapter 4 we construct a novel mean-field theory where both the scalar order parameter and the nematic director are allowed to vary, and which is valid for all values of the density or the temperature. We apply this theory to nematic enclosed in a flat rectangular box finding that the minimum energy patterns are characterized by continuum distortions such as splays and bends. Point defects may also arise increasing the energy of the configuration. Our results are in good agreement with experiments on fd-viruses (which can be used effectively as rod-like mesogens) confined in similar geometries [115]. The problem discuss in this chapter is the limiting case (when the length of the particles is much smaller than the confinement size) of the system considered in Chapter 2. In this regime wall defects are not present, indicating that they are due to the finite size of the mesogens.

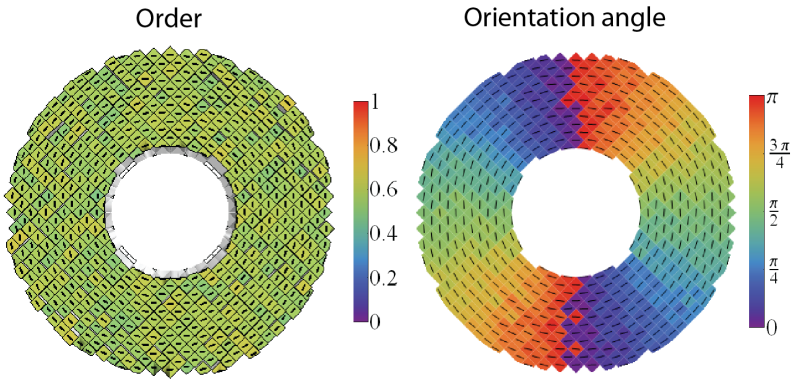

Figure 7.1: Minimum energy configuration of liquid crystal confined in a container with annular geometry. Parameters are the same as for figure 4.2.

The mean-field model we constructed can be successfully applied to other quasi 2D confined liquid crystalline systems. It can useful for the round or annular geometry discuss in Chapter 3, as comparison to the

Monte Carlo simulations. For the annular geometry preliminary results (shown in figure 7.1) indicate that in the continuum limit the wall defects vanish, the nematic director following the walls. This pattern is similar to a the one appearing around a point defect of topological charge +1 (see figure 1.3) located in the center of the container, point which is located outside the container.

Our mean-field theory is by no mens restricted to two dimensional systems or to planar wall anchoring. It would be interesting to apply our model to problems that have preoccupied the the liquid crystal community for a long time and for which solutions yielded by the different models are known. Such a problem is, for example, the organization of the director field around a colloidal particle with radial anchoring immersed in a homogeneous nematic. There it is expected to find a singular ring of a $-1/2$ disclination in the equatorial plane [155].

7.4 Membrane deformation versus cytoskeleton bending

In animal cells, where the membrane is deformable, the shape of the cell is the result of a mechanical interplay between the cytoskeletal filaments and the membrane. Experimentally, this problem is addressed in reconstructed systems. Starting from such *in vitro* experiments, we propose to study this interplay in two steps, finding first the configuration of a cytoskeletal polymers as a function of the membrane shape and then, by an energy minimization where we use the results obtained in the first step, finding the most favorable configuration of the full system (membrane and polymers together). In Chapter 5, using a conformational-biased Monte Carlo technique, we determine the shape of polymers enclosed in an ellipsoidal surface. We find that, even for small asymmetries of the confining surface the organization of the polymers changes significantly. Patterns observed include bundles, planar asters, circular and ellipsoidal rings.

The next step in understanding the mechanical interplay between membrane deformational and cytoskeletal organization is to correlate the total elastic energy of the pattern observed in simulation with the surface tension and elastic energy stored in the monolayer. The energy of the whole system, composed of membrane and enclosed polymers, should be minimized. This minimization will probably exclude the additional patterns seen in

simulations that are not experimentally observed, such as the ellipsoidal rings.

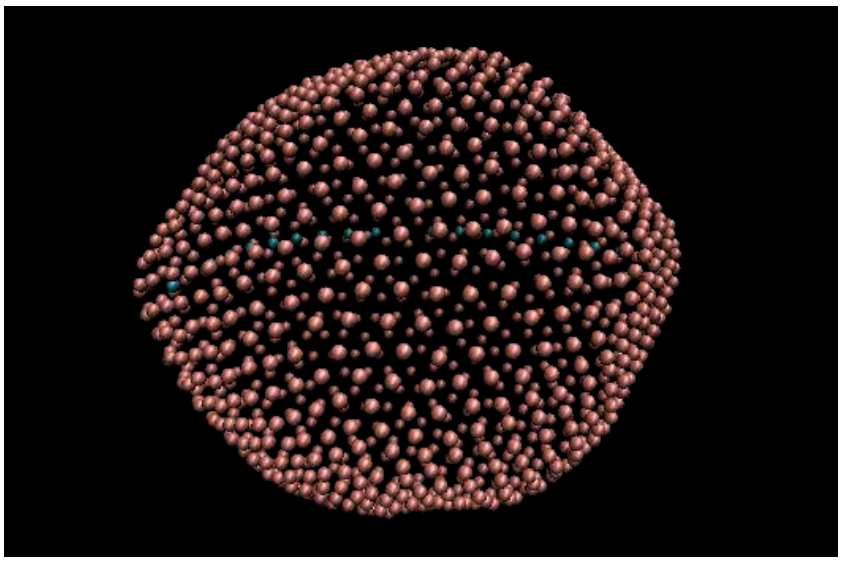

Figure 7.2: Elastic shell enclosing a polymer with length comparable with its diameter. Note that the surface adopts a lemon shape configuration. For a prolate ellipsoidal geometry surface tension is also needed. Configuration obtained using LAMMPS.

Another approach to this problem is to try to minimize both the energy of membrane and of the polymers at the same time. To this end open source software can be useful. An example of such a software that can handle both membranes and polymers is LAMMPS, a classical molecular dynamics code. The membrane is constructed out of a spherical particles which are linked by an elastic potential, whereas the polymers are strings of spheres with a bending cost associated to them. In figures 7.2 and 7.3 we show two representative configurations obtained by using this software. Unfortunately, this kind of software is only based on energy constraints, and thus it does not keep the enclosed volume constant. From the perspective of our model system (the emulsion droplet), this is unrealistic. However this kind of tools could be useful for a qualitative, rather than qualitative comparison to the results obtained by the other method described in this

section.

Generally, structures such as single bundles or asters contain cross-linking proteins, but our simulations show that the presence of cross-linkers is not essential for their formation. They can emerge from purely mechanical interactions. However, it would be interesting to address the role of motor proteins and crosslinkers in the stability of the patterns. To this end Cytosim software offers the ideal tool [156].

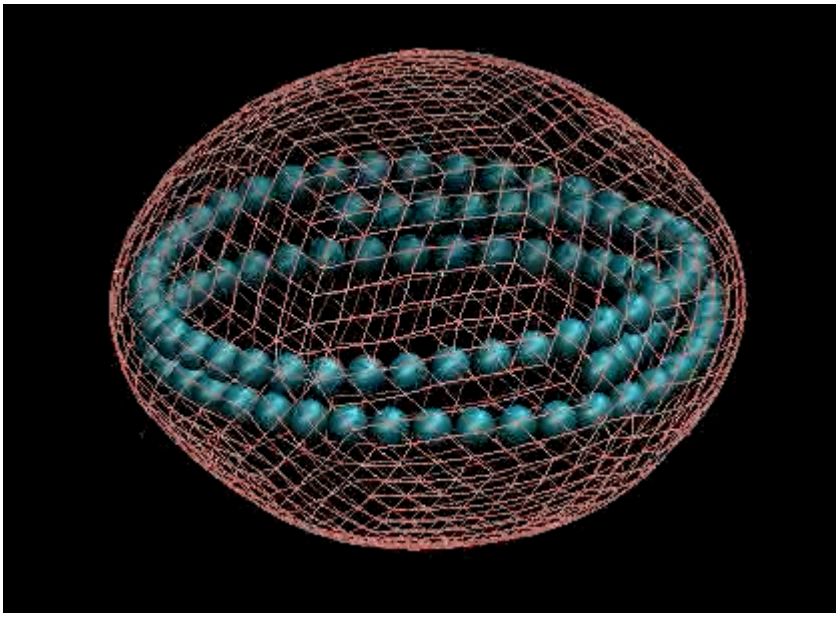

Figure 7.3: Elastic shell enclosing a polymer with much longer than the diameter of the confining surface. The membrane has an oblate shape. Configuration obtained using LAMMPS.

7.5 Positioning of microtubule asters

In Chapter 6 we investigated the repulsion between two microtubule asters due to steric interactions. We find that there is a minimum distance of approach between the two asters, consistent with experimental observations [126]. Effectively the aster behaves like a hard sphere with a diameter much higher than the one of the centrosome, but lower than the diameter of the

full aster. This effective diameter depends on the microtubule density in the asters and on their mean length.

The currently employed theoretical models designed to predict the positioning of a single microtubule aster enclosed by a rigid surface only account for pushing and pulling as force generation mechanisms, allowing also sliding of the microtubules along the membrane [151, 68]. The steric repulsion is probably not the only repulsive mechanism at work when two asters inside the same confining surface. Additionally there will most likely be a repulsion due to microtubules growing, and hence generating pushing forces, against the other aster. Also, the presence of the other aster may modify the microtubule distribution reaching the cortex, which in turn can lead to a positional change of the asters. Both these mechanism deserve further investigation and, if relevant, should be included in the current theoretical models.

7.6 Final remarks

The present work casts light on a few aspects of the cytoskeleton organization when subject to confinement and on how the cytoskeleton contributes to the organization of the cell. It is by no means complete, however, it opens a number of new research directions which can lead to a better understanding of the cytoskeleton but also to new perspectives in the field of confined liquid crystals.

Bibliography

[1] B. Alberts, D. Bray, J. Lewis, M. Raff, K. Robers, and J. D. Watson, *Molecular Biology of the Cell*. Garland Publishing, 3rd ed., 1994.

[2] M. Schuh, "An actin-dependent mechanism for long-range vesicle transport.," *Nature cell biology*, vol. 13, pp. 1431–6, Dec. 2011.

[3] B. L. Goode, D. G. Drubin, and G. Barnes, "Functional cooperation between the microtubule and actin cytoskeletons," *Current Opinion in Cell Biology*, vol. 12, no. 1, pp. 63 – 71, 2000.

[4] S. Etienne-Manneville, "Actin and microtubules in cell motility: Which one is in control?," *Traffic*, vol. 5, no. 7, pp. 470–477, 2004.

[5] Z. Gitai, "The new bacterial cell biology: Moving parts and subcellular architecture," *Cell*, vol. 120, no. 5, pp. 577 – 586, 2005.

[6] S. F. Edwards and M. Doi, *The theory of polymer dynamics*. 1986.

[7] M. R. Mofrad and R. Kamm, *Cytoskeletal mechanics*. Cambridge University Press New York:, 2006.

[8] F. Gittes, B. Mickey, J. Nettleton, and J. Howard, "Flexural rigidity of microtubules and actin filaments measured from thermal fluctuations in shape.," *The Journal of Cell Biology*, vol. 120, no. 4, pp. 923–934, 1993.

[9] F. Pampaloni, G. Lattanzi, A. Jon, T. Surrey, E. Frey, and E.-L. Florin, "Thermal fluctuations of grafted microtubules provide evidence of a length-dependent persistence length," *Proceedings of the National Academy of Sciences*, vol. 103, no. 27, pp. 10248–10253, 2006.

[10] H. Li, D. J. DeRosier, W. V. Nicholson, E. Nogales, and K. H. Downing, "Microtubule structure at 8 a resolution," *Structure*, vol. 10, no. 10, pp. 1317 – 1328, 2002.

[11] A. Desai and T. J. Mitchison, "Microtubule polymerization dynamics.," *Annual review of cell and developmental biology*, vol. 13, pp. 83–117, Jan. 1997.

[12] V. I. Gelfand and A. D. Bershadsky, "Microtubule dynamics: mechanism, regulation, and function.," *Annual review of cell biology*, vol. 7, pp. 93–116, Jan. 1991.

[13] I. Arnal and R. H. Wade, "How does taxol stabilize microtubules?," *Current Biology*, vol. 5, no. 8, pp. 900 – 908, 1995.

[14] A. Ott, M. Magnasco, A. Simon, and A. Libchaber, "Measurement of the persistence length of polymerized actin using fluorescence microscopy," *Phys. Rev. E*, vol. 48, pp. R1642–R1645, Sep 1993.

[15] A. Bremer and U. Aebi, "The structure of the f-actin filament and the actin molecule," *Current Opinion in Cell Biology*, vol. 4, no. 1, pp. 20 – 26, 1992.

[16] J.-M. Neuhaus, M. Wanger, T. Keiser, and A. Wegner, "Treadmilling of actin," *Journal of Muscle Research & Cell Motility*, vol. 4, no. 5, pp. 507–527, 1983.

[17] E. Fuchs and K. Weber, "Intermediate filaments: structure, dynamics, function, and disease.," *Annual review of biochemistry*, vol. 63, pp. 345–82, Jan. 1994.

[18] Q. Wen and P. A. Janmey, "Polymer physics of the cytoskeleton," *Current Opinion in Solid State and Materials Science*, vol. 15, no. 5, pp. 177 – 182, 2011.

[19] D. A. Fletcher and R. D. Mullins, "Cell mechanics and the cytoskeleton.," *Nature*, vol. 463, pp. 485–92, Jan. 2010.

[20] E. Debus, K. Weber, and M. Osborn, "The cytoskeleton of blood platelets viewed by immunofluorescence microscopy.," *European journal of cell biology*, vol. 24, pp. 45–52, Apr. 1981.

[21] J. G. White and G. H. Rao, "Microtubule coils versus the surface membrane cytoskeleton in maintenance and restoration of platelet discoid shape.," *The American journal of pathology*, vol. 152, pp. 597–609, Feb. 1998.

[22] F. J. McNally, "Mechanisms of spindle positioning.," *The Journal of cell biology*, vol. 200, pp. 131–40, Jan. 2013.

[23] D. N. Robinson and J. A. Spudich, "Towards a molecular understanding of cytokinesis," *Trends in Cell Biology*, vol. 10, no. 6, pp. 228 – 237, 2000.

[24] T. D. Pollard and G. G. Borisy, "Cellular motility driven by assembly and disassembly of actin filaments," *Cell*, vol. 112, no. 4, pp. 453 – 465, 2003.

[25] B. Gunning and M. Steer, *Plant Cell Biology, Structure and Function.* Jones & Barlett Learning, Boston, 1996.

[26] S. H. Tindemans, R. J. Hawkins, and B. M. Mulder, "Survival of the aligned: Ordering of the plant cortical microtubule array," *Phys. Rev. Lett.*, vol. 104, p. 058103, Feb 2010.

[27] M. Dogterom, J. W. Kerssemakers, G. Romet-Lemonne, and M. E. Janson, "Force generation by dynamic microtubules," *Current Opinion in Cell Biology*, vol. 17, no. 1, pp. 67 – 74, 2005.

[28] M. E. Janson, M. E. de Dood, and M. Dogterom, "Dynamic instability of microtubules is regulated by force," *The Journal of Cell Biology*, vol. 161, no. 6, pp. 1029–1034, 2003.

[29] J. V. Small, M. Herzog, and K. Anderson, "Actin filament organization in the fish keratocyte lamellipodium.," *The Journal of Cell Biology*, vol. 129, no. 5, pp. 1275–1286, 1995.

[30] A. B. Verkhovsky, O. Y. Chaga, S. Schaub, T. M. Svitkina, J.-J. Meister, and G. G. Borisy, "Orientational order of the lamellipodial actin network as demonstrated in living motile cells.," *Molecular biology of the cell*, vol. 14, pp. 4667–75, Nov. 2003.

[31] E. Urban, S. Jacob, M. Nemethova, G. P. Resch, and J. V. Small, "Electron tomography reveals unbranched networks of actin filaments in lamellipodia.," *Nature cell biology*, vol. 12, pp. 429–35, May 2010.

[32] G. Gallo and P. C. Letourneau, "Regulation of growth cone actin filaments by guidance cues," *Journal of Neurobiology*, vol. 58, no. 1, pp. 92–102, 2004.

[33] P. M. Bendix, G. H. Koenderink, D. Cuvelier, Z. Dogic, B. N. Koeleman, W. M. Brieher, C. M. Field, L. Mahadevan, and D. A. Weitz, "A quantitative analysis of contractility in active cytoskeletal protein networks," *Biophysical Journal*, vol. 94, no. 8, pp. 3126 – 3136, 2008.

[34] B. Wagner, R. Tharmann, I. Haase, M. Fischer, and A. R. Bausch, "Cytoskeletal polymer networks: The molecular structure of cross-linkers determines macroscopic properties," *Proceedings of the National Academy of Sciences*, vol. 103, no. 38, pp. 13974–13978, 2006.

[35] M. Edlund, M. A. Lotano, and C. A. Otey, "Dynamics of -actinin in focal adhesions and stress fibers visualized with -actinin-green fluorescent protein," *Cell Motility and the Cytoskeleton*, vol. 48, no. 3, pp. 190–200, 2001.

[36] P. K. Mattila and P. Lappalainen, "Filopodia: molecular architecture and cellular functions.," *Nature reviews. Molecular cell biology*, vol. 9, pp. 446–54, June 2008.

[37] A. J. Ehrlicher, F. Nakamura, J. H. Hartwig, D. A. Weitz, and T. P. Stossel, "Mechanical strain in actin networks regulates FilGAP and integrin binding to filamin A.," *Nature*, vol. 478, pp. 260–3, Oct. 2011.

[38] F. Jülicher, A. Ajdari, and J. Prost, "Modeling molecular motors," *Rev. Mod. Phys.*, vol. 69, pp. 1269–1282, Oct 1997.

[39] R. B. Vallee, G. E. Seale, and J.-W. Tsai, "Emerging roles for myosin II and cytoplasmic dynein in migrating neurons and growth cones.," *Trends in cell biology*, vol. 19, pp. 347–55, July 2009.

[40] E. Luna and A. Hitt, "Cytoskeleton–plasma membrane interactions," *Science*, vol. 258, no. 5084, pp. 955–964, 1992.

[41] V. Bennett, "The spectrin-actin junction of erythrocyte membrane skeletons," *Biochimica et Biophysica Acta (BBA) - Reviews on Biomembranes*, vol. 988, no. 1, pp. 107 – 121, 1989.

[42] M. Soares e Silva, J. Alvarado, J. Nguyen, N. Georgoulia, B. M. Mulder, and G. H. Koenderink, "Self-organized patterns of actin filaments in cell-sized confinement," *Soft Matter*, vol. 7, pp. 10631–10641, 2011.

[43] S. Matosevic, "Synthesizing artificial cells from giant unilamellar vesicles: state-of-the art in the development of microfluidic technology.," *BioEssays : news and reviews in molecular, cellular and developmental biology*, vol. 34, pp. 992–1001, Nov. 2012.

[44] S. F. Fenz and K. Sengupta, "Giant vesicles as cell models.," *Integrative biology : quantitative biosciences from nano to macro*, vol. 4, pp. 982–95, Sept. 2012.

[45] F. C. Tsai, S. Roth, M. Dogterom, and G. H. Koenderink, *Biomimetic liposome model systems to study cell shape control by the cytoskeleton*, pp. Chap. 6: 139–174. Elsevier, May 6th 2014.

[46] L.-L. Pontani, J. van der Gucht, G. Salbreux, J. Heuvingh, J.-F. Joanny, and C. Sykes, "Reconstitution of an actin cortex inside a liposome.," *Biophysical journal*, vol. 96, pp. 192–8, Jan. 2009.

[47] K. Sengupta, L. Limozin, M. Tristl, I. Haase, M. Fischer, and E. Sackmann, "Coupling artificial actin cortices to biofunctionalized lipid monolayers.," *Langmuir : the ACS journal of surfaces and colloids*, vol. 22, pp. 5776–85, June 2006.

[48] M. Pinot, F. Chesnel, J. Z. Kubiak, I. Arnal, F. J. Nedelec, and Z. Gueroui, "Effects of confinement on the self-organization of microtubules and motors.," *Current biology : CB*, vol. 19, pp. 954–60, June 2009.

[49] D. Kuchnir Fygenson, M. Elbaum, B. Shraiman, and A. Libchaber, "Microtubules and vesicles under controlled tension," *Phys. Rev. E*, vol. 55, pp. 850–859, Jan 1997.

[50] M. Elbaum, D. Kuchnir Fygenson, and A. Libchaber, "Buckling Microtubules in Vesicles," *Physical Review Letters*, vol. 76, pp. 4078–4081, May 1996.

[51] P. K. Sorger, M. Dobles, R. Tournebize, and A. A. Hyman, "Coupling cell division and cell death to microtubule dynamics," *Current Opinion in Cell Biology*, vol. 9, no. 6, pp. 807 – 814, 1997.

[52] A.-M. C. Yvon, P. Wadsworth, and M. A. Jordan, "Taxol suppresses dynamics of individual microtubules in living human tumor cells," *Molecular Biology of the Cell*, vol. 10, no. 4, pp. 947–959, 1999.

[53] M. a. Ojeda-Lopez, D. J. Needleman, C. Song, A. Ginsburg, P. a. Kohl, Y. Li, H. P. Miller, L. Wilson, U. Raviv, M. C. Choi, and C. R. Safinya, "Transformation of taxol-stabilized microtubules into inverted tubulin tubules triggered by a tubulin conformation switch.," *Nature materials*, vol. 13, pp. 1–9, Jan. 2014.

[54] G. R. Heath, R. H. Abou-Saleh, S. A. Peyman, B. R. G. Johnson, S. D. Connell, and S. D. Evans, "Self-assembly of actin scaffolds on lipid microbubbles," *Soft Matter*, vol. 10, pp. 694–700, 2014.

[55] P. G. de Gennes and J. Prost, *The Physics of Liquid Crystals*. Claredon Press, Oxford, 1993.

[56] S. Fraden, "Phase transitions in colloidal suspensions of virus particles," in *Observation, Prediction and Simulation of Phase Transitions in Complex Fluids* (M. Baus, L. Rull, and J.-P. Ryckaert, eds.), vol. 460 of *NATO ASI Series*, pp. 113–164, Springer Netherlands, 1995.

[57] E. Barry, D. Beller, and Z. Dogic, "A model liquid crystalline system based on rodlike viruses with variable chirality and persistence length," *Soft Matter*, vol. 5, pp. 2563–2570, 2009.

[58] Z. Dogic and S. Fraden, "Ordered phases of filamentous viruses," *Current Opinion in Colloid & Interface Science*, vol. 11, no. 1, pp. 47 – 55, 2006.

[59] J.-L. Barrat and J.-P. Hansen, *Basic Concepts for Simple and Complex Liquids*. Cambridge University Press, 2003.

[60] L. Onsager, "The effects of shape on the interaction of colloidal particles," *Annals of the New York Academy of Sciences*, vol. 51, no. 4, pp. 627–659, 1949.

[61] J. A. C. Veerman and D. Frenkel, "Phase diagram of a system of hard spherocylinders by computer simulation," *Phys. Rev. A*, vol. 41, pp. 3237–3244, Mar 1990.

[62] J. Viamontes, P. W. Oakes, and J. X. Tang, "Isotropic to nematic liquid crystalline phase transition of f-actin varies from continuous to first order," *Phys. Rev. Lett.*, vol. 97, p. 118103, Sep 2006.

[63] M. Cosentino Lagomarsino, C. Tanase, J. W. Vos, A. M. C. Emons, B. M. Mulder, and M. Dogterom, "Microtubule organization in three-dimensional confined geometries: evaluating the role of elasticity through a combined in vitro and modeling approach.," *Biophysical journal*, vol. 92, pp. 1046–57, Feb. 2007.

[64] M. Dijkstra, R. v. Roij, and R. Evans, "Wetting and capillary nematization of a hard-rod fluid: A simulation study," *Phys. Rev. E*, vol. 63, p. 051703, Apr 2001.

[65] D. Demus and L. Richter, *Textures of liquid crystals*. Verlag Chemie Weinheim, 1978.

[66] D. Frenkel and B. Smit, *Understanding Molecular Simulation, Second Edition: From Algorithms to Applications (Computational Science)*. Academic Press, 2001.

[67] M. P. Allen, G. T. Evans, D. Frenkel, and B. Mulder, *Hard convex body fluids*, vol. 86 of *Advances in chemical physics*. New York, Wiley, 1993.

[68] N. Pavin, L. Laan, R. Ma, M. Dogterom, and F. Jlicher, "Positioning of microtubule organizing centers by cortical pushing and pulling forces," *New Journal of Physics*, vol. 14, no. 10, p. 105025, 2012.

[69] B. Alberts, A. Johnson, J. Lewis, M. Raff, K. Roberts, and P. Walter, *Molecular Biology of the Cell*. Garland Science, 2007.

[70] R. H. Chen, *Liquid Crystal Displays: Fundamental Physics and Technology (Wiley Series in Display Technology)*. Wiley, 2011.

[71] C. Tsakonas, A. J. Davidson, C. V. Brown, and N. J. Mottram, "Multistable alignment states in nematic liquid crystal filled wells," *Applied Physics Letters*, vol. 90, no. 11, p. 111913, 2007.

[72] C. Luo, A. Majumdar, and R. Erban, "Multistability in planar liquid crystal wells," *Physical Review E*, vol. 85, no. 6, p. 061702, 2012.

[73] M. Cosentino Lagomarsino, M. Dogterom, and M. Dijkstra, "Isotropicnematic transition of long, thin, hard spherocylinders confined in a quasi-two-dimensional planar geometry," *The Journal of Chemical Physics*, vol. 119, no. 6, pp. 3535–3540, 2003.

[74] J. Galanis, D. Harries, D. L. Sackett, W. Losert, and R. Nossal, "Spontaneous patterning of confined granular rods," *Phys. Rev. Lett.*, vol. 96, p. 028002, Jan 2006.

[75] J. Z. Y. Chen, "Structure of two-dimensional rods confined by a line boundary," *Soft Matter*, vol. 9, pp. 10921–10930, 2013.

[76] L. Verlet, "Computer "experiments" on classical fluids. i. thermodynamical properties of lennard-jones molecules," *Phys. Rev.*, vol. 159, pp. 98–103, Jul 1967.

[77] P. G. de Gennes and J. Prost, *The Physics of Liquid Crystals (International Series of Monographs on Physics)*. Oxford University Press, USA, 1995.

[78] P. Bolhuis and D. Frenkel, "Tracing the phase boundaries of hard spherocylinders," *The Journal of Chemical Physics*, vol. 106, no. 2, pp. 666–687, 1997.

[79] R. F. Kayser and H. J. Raveché, "Bifurcation in onsager's model of the isotropic-nematic transition," *Phys. Rev. A*, vol. 17, pp. 2067–2072, Jun 1978.

[80] I. Gradshteyn and I. Ryzhik, "Definite integrals of special functions," in *Table of Integrals, Series, and Products (Seventh Edition)* (A. Jeffrey, D. Zwillinger, I. Gradshteyn, and I. Ryzhik, eds.), pp. 631 – 857, Boston: Academic Press, seventh edition ed., 2007.

[81] J. Dzubiella, M. Schmidt, and H. Löwen, "Topological defects in nematic droplets of hard spherocylinders," *Physical Review E*, vol. 62, no. 4, pp. 5081–5091, 2000.

[82] D. de las Heras, E. Velasco, and L. Mederos, "Topological defects in a two-dimensional liquid crystal confined in a circular nanocavity," *Physical Review E*, vol. 79, no. 6, p. 061703, 2009.

[83] D. d. l. Heras and E. Velasco, "Domain walls in two-dimensional nematics confined in a small circular cavity," *Soft Matter*, vol. 10, pp. 1758–1766, 2014.

[84] Y. Trukhina and T. Schilling, "Computer simulation study of a liquid crystal confined to a spherical cavity," *Phys. Rev. E*, vol. 77, p. 011701, Jan 2008.

[85] P. Prinsen and P. van der Schoot, "Shape and director-field transformation of tactoids," *Physical Review E*, vol. 68, no. 2, p. 021701, 2003.

[86] M. A. Bates, "Nematic ordering and defects on the surface of a sphere: a Monte Carlo simulation study.," *The Journal of chemical physics*, vol. 128, no. 10, p. 104707, 2008.

[87] T. Lopez-Leon, V. Koning, K. B. S. Devaiah, V. Vitelli, and A. Fernandez-Nieves, "Frustrated nematic order in spherical geometries," *Nature Physics*, vol. 7, no. 5, pp. 391–394, 2011.

[88] S. R. Seyednejad, M. R. Mozaffari, and M. R. Ejtehadi, "Confined nematic liquid crystal between two spherical boundaries with planar anchoring," *Physical Review E*, vol. 88, no. 1, p. 012508, 2013.

[89] D. M. Brink and G. R. Satchler, *Angular momentum*. Clarendon Press, 1968.

[90] G. T. Charras, C.-K. Hu, M. Coughlin, and T. J. Mitchison, "Reassembly of contractile actin cortex in cell blebs," *The Journal of Cell Biology*, vol. 175, no. 3, pp. 477–490, 2006.

[91] G. P. Crawford and S. Zumer, *Liquid crystals in complex geometries: formed by polymer and porous networks*. CRC Press, 1996.

[92] J. W. Doane and G. P. Crawford, *Polymer Dispersed Liquid Crystals*. John Wiley & Sons, Ltd, 2007.

[93] S. Žumer and J. W. Doane, "Light scattering from a small nematic droplet," *Phys. Rev. A*, vol. 34, pp. 3373–3386, Oct 1986.

[94] B. Bahadur and M. Tilton, *Liquid crystals: applications and uses*, vol. 3. World Scientific, 1992.

[95] H. Shin, M. J. Bowick, and X. Xing, "Topological defects in spherical nematics," *Phys. Rev. Lett.*, vol. 101, p. 037802, Jul 2008.

[96] A. Fernández-Nieves, V. Vitelli, A. S. Utada, D. R. Link, M. Márquez, D. R. Nelson, and D. A. Weitz, "Novel defect structures in nematic liquid crystal shells," *Phys. Rev. Lett.*, vol. 99, p. 157801, Oct 2007.

[97] V. Koning, T. Lopez-Leon, A. Fernandez-Nieves, and V. Vitelli, "Bivalent defect configurations in inhomogeneous nematic shells," *Soft Matter*, vol. 9, pp. 4993–5003, 2013.

[98] R. J. Ondris-Crawford, G. P. Crawford, S. Zumer, and J. W. Doane, "Curvature-induced configuration transition in confined nematic liquid crystals," *Phys. Rev. Lett.*, vol. 70, pp. 194–197, Jan 1993.

[99] K. Jian, R. H. Hurt, B. W. Sheldon, and G. P. Crawford, "Visualization of liquid crystal director fields within carbon nanotube cavities," *Applied Physics Letters*, vol. 88, no. 16, p. 163110, 2006.

[100] P. Prinsen and P. van der Schoot, "Continuous director-field transformation of nematic tactoids," *The European Physical Journal E*, vol. 13, no. 1, pp. 35–41, 2004.

[101] H. Poincaré, "Mémoire sur les courbes définies par une équation différentielle (ii)," *Journal de mathématiques pures et appliquées*, pp. 251–296, 1882.

[102] R. D. Kamien, "The geometry of soft materials: a primer," *Rev. Mod. Phys.*, vol. 74, pp. 953–971, Sep 2002.

[103] T. C. Lubensky, D. Pettey, N. Currier, and H. Stark, "Topological defects and interactions in nematic emulsions," *Phys. Rev. E*, vol. 57, pp. 610–625, Jan 1998.

[104] J. Alvarado, *Biological polymers : confined, bent, and driven.* PhD thesis, VU University Amsterdam, June 17th 2013.

[105] M. Dogterom and S. Leibler, "Physical aspects of the growth and regulation of microtubule structures," *Phys. Rev. Lett.*, vol. 70, pp. 1347–1350, Mar 1993.

[106] B. M. Mulder, "Microtubules interacting with a boundary : mean length and mean first-passage times," *Phys. Rev. E*, vol. 86, pp. 011902 1–11, July 2nd 2012.

[107] M. KAWAMURA and K. MARUYAMA, "Electron microscopic particle length of f-actin polymerized in vitro," *Journal of Biochemistry*, vol. 67, no. 3, pp. 437–457, 1970.

[108] C. Oseen, "The theory of liquid crystals," *Trans. Faraday Soc*, no. 29, pp. 833–899, 1933.

[109] F. C. Frank, "I. liquid crystals. on the theory of liquid crystals," *Discuss. Faraday Soc.*, vol. 25, pp. 19–28, 1958.

[110] L. Landau and E. Lifshitz, *Statistical Physics, Vol. 1.* Oxford: Pergamon Press, 1980.

[111] P. De Gennes, "Short range order effects in the isotropic phase of nematics and cholesterics," *Molecular Crystals and Liquid Crystals*, vol. 12, no. 3, pp. 193–214, 1971.

[112] M. Abramowitz and I. A. Stegun, *Handbook of mathematical functions: with formulas, graphs, and mathematical tables.* No. 55, Courier Dover Publications, 1972.

[113] I. P. A. Rapini, "Distortion dune lamelle nematique sous champ magnetique conditions dancrage aux parois.," *J. de Phys. Colloq*, vol. 30, no. C4-54-C4-56, 1969.

[114] L. Ingber, "Adaptive simulated annealing (asa): Lessons learned," *Control and cybernetics*, vol. 25, pp. 33–54, 1996.

[115] A. H. Lewis, I. Garlea, J. Alvarado, O. J. Dammone, P. D. Howell, A. Majumdar, B. M. Mulder, M. P. Lettinga, G. H. Koenderink, and D. G. A. L. Aarts, "Colloidal liquid crystals in rectangular confinement: theory and experiment," *Soft matter*, vol. 10, no. 39, pp. 7865–7873, 2014.

[116] J. C. Canman, L. A. Cameron, P. S. Maddox, A. Straight, J. S. Tirnauer, T. J. Mitchison, G. Fang, T. M. Kapoor, and E. Salmon, "Determining the position of the cell division plane," *Nature*, vol. 424, no. 6952, pp. 1074–1078, 2003.

[117] J. White and J. Sauk, "Microtubule coils in spread blood platelets," *Blood*, vol. 64, no. 2, pp. 470–478, 1984.

[118] G. Escolar, M. Krumwiede, and J. White, "Organization of the actin cytoskeleton of resting and activated platelets in suspension.," *The American journal of pathology*, vol. 123, no. 1, p. 86, 1986.

[119] V. T. Nachmias, "Cytoskeleton of human platelets at rest and after spreading.," *The Journal of Cell Biology*, vol. 86, no. 3, pp. 795–802, 1980.

[120] F.-C. Tsai, B. Stuhrmann, and G. H. Koenderink, "Encapsulation of active cytoskeletal protein networks in cell-sized liposomes," *Langmuir*, vol. 27, no. 16, pp. 10061–10071, 2011.

[121] S. K. Vogel and P. Schwille, "Minimal systems to study membranecytoskeleton interactions," *Current Opinion in Biotechnology*, vol. 23, no. 5, pp. 758 – 765, 2012. Tissue, cell and pathway engineering.

[122] D. K. Fygenson, J. F. Marko, and A. Libchaber, "Mechanics of microtubule-based membrane extension," *Phys. Rev. Lett.*, vol. 79, pp. 4497–4500, Dec 1997.

[123] H. Baumann and T. Surrey, "Motor-mediated cortical versus astral microtubule organization in lipid-monolayered droplets," *Journal of Biological Chemistry*, vol. 289, no. 32, pp. 22524–22535, 2014.

[124] M. M. A. E. Claessens, M. Bathe, E. Frey, and A. R. Bausch, "Actin-binding proteins sensitively mediate f-actin bundle stiffness," *Nat Mater*, vol. 5, pp. 748–753, Sept. 2006.

[125] F. C. Tsai, "Private communication."

[126] S. Roth, "Private communication."

[127] R. Lipowsky, "The conformation of membranes," *Nature*, vol. 349, no. 6309, pp. 475–481, 1991.

[128] R. Morikawa, Y. Saito, and H. Hyuga, "Monte carlo study of a vesicle morphology caused by microtubule assembly," *Journal of the Physical Society of Japan*, vol. 68, no. 5, pp. 1760–1768, 1999.

[129] T. Umeda, H. Nakajima, and H. Hotani, "Theoretical analysis of shape transformations of liposomes caused by microtubule assembly," *Journal of the Physical Society of Japan*, vol. 67, no. 2, pp. 682–688, 1998.

[130] W. T. Gozdz, "Influence of spontaneous curvature and microtubules on the conformations of lipid vesicles," *The Journal of Physical Chemistry B*, vol. 109, no. 44, pp. 21145–21149, 2005. PMID: 16853739.

[131] J. Gao, P. Tang, Y. Yang, and J. Z. Y. Chen, "Free energy of a long semiflexible polymer confined in a spherical cavity," *Soft Matter*, vol. 10, pp. 4674–4685, 2014.

[132] A. Cacciuto and E. Luijten, "Self-avoiding flexible polymers under spherical confinement," *Nano Letters*, vol. 6, no. 5, pp. 901–905, 2006. PMID: 16683822.

[133] K. Alim and E. Frey, "Fluctuating semiflexible polymer ribbon constrained to a ring," *The European Physical Journal E*, vol. 24, no. 2, pp. 185–191, 2007.

[134] K. Ostermeir, K. Alim, and E. Frey, "Confinement induces conformational transition of semiflexible polymer rings to figure eight form," *Soft Matter*, vol. 6, no. 15, pp. 3467–3471, 2010.

[135] K. Ostermeir, K. Alim, and E. Frey, "Buckling of stiff polymer rings in weak spherical confinement," *Physical Review E*, vol. 81, no. 6, p. 061802, 2010.

[136] M. Fritsche and D. W. Heermann, "Confinement driven spatial organization of semiflexible ring polymers: implications for biopolymer packaging," *Soft Matter*, vol. 7, no. 15, pp. 6906–6913, 2011.

[137] P.-O. Mouthuy, M. Coulombier, T. Pardoen, J.-P. Raskin, and A. M. Jonas, "Overcurvature describes the buckling and folding of rings

from curved origami to foldable tents," *Nature communications*, vol. 3, p. 1290, 2012.

[138] M. Fošnarič, A. Iglič, D. M. Kroll, and S. May, "Monte carlo simulations of a polymer confined within a fluid vesicle," *Soft Matter*, vol. 9, no. 15, pp. 3976–3984, 2013.

[139] D. Marenduzzo and E. Orlandini, "Dynamics of fibers growing inside soft vesicles," *EPL (Europhysics Letters)*, vol. 80, no. 4, p. 48004, 2007.

[140] M. N. Rosenbluth and A. W. Rosenbluth, "Monte carlo calculation of the average extension of molecular chains," *The Journal of Chemical Physics*, vol. 23, no. 2, pp. 356–359, 1955.

[141] D. Frenkel, G. C. A. M. Mooij, and B. Smit, "Novel scheme to study structural and thermal properties of continuously deformable molecules," *Journal of Physics: Condensed Matter*, vol. 4, no. 12, p. 3053, 1992.

[142] M. Dijkstra, D. Frenkel, and H. Lekkerkerker, "Confinement free energy of semiflexible polymers," *Physica A*, vol. 193, pp. 374–393, Jan. 1st 1993.

[143] M. Moritz, M. B. Braunfeld, J. C. Fung, J. W. Sedat, B. M. Alberts, and D. A. Agard, "Three-dimensional structural characterization of centrosomes from early drosophila embryos.," *The Journal of cell biology*, vol. 130, no. 5, pp. 1149–1159, 1995.

[144] D. Chrétien, B. Buendia, S. D. Fuller, and E. Karsenti, "Reconstruction of the centrosome cycle from cryoelectron micrographs," *Journal of structural biology*, vol. 120, no. 2, pp. 117–133, 1997.

[145] T. Wittmann, A. Hyman, and A. Desai, "The spindle: a dynamic assembly of microtubules and motors," *Nature cell biology*, vol. 3, no. 1, pp. E28–E34, 2001.

[146] L. Laan, N. Pavin, J. Husson, G. Romet-Lemonne, M. van Duijn, M. P. López, R. D. Vale, F. Jülicher, S. L. Reck-Peterson, and M. Dogterom, "Cortical dynein controls microtubule dynamics to

generate pulling forces that position microtubule asters," *Cell*, vol. 148, no. 3, pp. 502–514, 2012.

[147] L. Laan, S. Roth, and M. Dogterom, "End-on microtubule-dynein interactions and pulling-based positioning of microtubule organizing centers," *Cell Cycle*, vol. 11, no. 20, pp. 3750–3757, 2012.

[148] M. Dogterom and B. Yurke, "Measurement of the force-velocity relation for growing microtubules," *Science*, vol. 278, no. 5339, pp. 856–860, 1997.

[149] E. L. Grishchuk, M. I. Molodtsov, F. I. Ataullakhanov, and J. R. McIntosh, "Force production by disassembling microtubules," *Nature*, vol. 438, no. 7066, pp. 384–388, 2005.

[150] V. A. Lombillo, R. J. Stewart, and J. R. McIntosh, "Minus-end-directed motion of kinesin–coated microspheres driven by microtubule depolymerization," *Nature*, vol. 373, no. 6510, pp. 161–164, 1995.

[151] R. Ma, L. Laan, M. Dogterom, N. Pavin, and F. Jülicher, "General theory for the mechanics of confined microtubule asters," *New Journal of Physics*, vol. 16, no. 1, p. 013018, 2014.

[152] B. M. Mulder, "The excluded volume of hard sphero-zonotopes," *Molecular Physics*, vol. 103, no. 10, pp. 1411–1424, 2005.

[153] P. Bolhuis, A. Louis, J. Hansen, and E. Meijer, "Accurate effective pair potentials for polymer solutions," *The Journal of Chemical Physics*, vol. 114, no. 9, pp. 4296–4311, 2001.

[154] A. Ponti, M. Machacek, S. Gupton, C. Waterman-Storer, and G. Danuser, "Two distinct actin networks drive the protrusion of migrating cells," *Science*, vol. 305, no. 5691, pp. 1782–1786, 2004.

[155] O. V. Kuksenok, R. W. Ruhwandl, S. V. Shiyanovskii, and E. M. Terentjev, "Director structure around a colloid particle suspended in a nematic liquid crystal," *Phys. Rev. E*, vol. 54, pp. 5198–5203, Nov 1996.

[156] F. Nedelec and D. Foethke, "Collective langevin dynamics of flexible cytoskeletal fibers," *New Journal of Physics*, vol. 9, no. 11, p. 427, 2007.

Summary

The shape of animal cells is in controlled by a network of filamentous polymers called the cytoskeleton. The two main components of the cytoskeleton are actin filaments and microtubules. These polymers continuously reorganize in order to performed their diverse cellular functions. For example, in processes such as cell migration actin filaments grow against the membrane, creating flat protrusions called lamellipodia. The lamellipodia enable the cells to move over surfaces. Microtubules are a key player in the cell division mechanism. There, the proper separation of the genetic material between the two daughter cells is controlled by two microtubule asters. The positioning of these two asters also determines the location where the cells will physically separate. Both migration and division are crucial processes for the cell, however the mechanisms underlying these processes are still poorly understood. The organization of the cytoskeleton in cells, and thus their functioning as cell shapers, is an interplay between mutual interaction, confinement and protein mediated interactions. Since cells are exquisitely complex systems, experimentally, the bottom-up approach proves useful in understanding the contribution of each of these interactions on the cytoskeleton organization. This approach is based on the idea of reconstructing a minimal system and adding more complexity to it as our understanding of this system increases.

Starting by a bottom-up approach, as it is done in experimental systems, we study various aspects of confinement and mutual interactions on cytoskeleton organization. The simplest system in which these two interactions are expected to compete is when dense enough rigid cytoskeletal polymers are confined. Experimentally, this question is addressed by confining these polymers in microchambers which are small compared to the persistence length of the enclosed polymers. In Chapter 2, using Monte Carlo simulations, we investigate the organization of rigid polymers confined in shallow square containers, this geometry being simplified model

of a lamellipodium. We find that, in the regime where the confinement effect, which causes wall alignment of the polymers, competes with the self-aligning tendency of the polymers, the organization is characterized by a nematic droplet aligned along a diagonal and wall aligned polymers. The pattern is stabilized by linear defect structures.

By the same methods, in Chapter 3, we study rigid polymers in curved wall confinement, finding that the bipolar structure appearing in the disk geometry is drastically modified by the opening of a hole in the middle of the container. Unexpectedly, in this annular geometry, the organization is characterized by highly aligned domains separated by radial defect walls. The patterns observed are the result of the finite size of the particles.

When the rigid polymers are small compared to the confining volume, their orientation is expected to vary over lengths which are much larger than the length of the polymer. In this regime the system is well described by continuum theories. Since currently employed continuum models either exclude the emergence of singularities by the way they are constructed (Oseen-Frank model) or are valid only in for a limited density range around the transition from an unordered to an ordered system (Landau-De Gennes model), in Chapter 4, we construct a mean-field model combining the virtues of these two models. We apply this model to a system of rigid small polymers enclosed in rectangular shallow container (geometry similar to the one in Chapter 2), finding that patterns which are minimizing the energy of the system are characterized by continuum variation of the orientation. However, our model also yields patterns containing point defects which have slightly higher energy.

So far we have considered only rigid cytoskeletal polymers, however at the length scale of the cell the polymers are better described by an elastic rod. In Chapter 5 we study the configurations adopted by a cytoskeletal polymers when enclosed by a rigid ellipsoidal membrane. We find that, compared to the spherical confinement, the change in shape of the confining membrane leads to non-trivial organization of the enclosed polymers. Among the patters observed are single bundles, planar asters, circular and elliptical rings. In reconstructed systems such as emulsion droplets the cytoskeletal polymers push against the membrane, deforming it but, since the membrane is under tension, it also constrains them to bend. Determining the polymeric configurations as a function of the confining surface is the first step towards understanding this mechanical interplay between the

cytoskeleton and the the membrane.

For proper cell division, a precise positioning of the two microtubule asters involved is required. The positioning of the two asters is based on pushing and pulling forces generated by the microtubule-membrane interaction. Experimental evidence shows that, in reconstructed systems, a spatial separation between the two asters in always present. Therefore, in Chapter 6, we investigate the steric repulsion between two asters finding that it indeed leads to a spatial separation.

The models that we developed in this thesis are a starting point for understanding the cytoskeletal organization and its role in the cell. In the last Chapter of this thesis we give some directions that the present work opens.

Samenvatting

De vorm en de werking van dierlijke cellen wordt in belangrijke mate bepaald door een netwerk van lange polymeren van eiwiteenheden, genaamd het cytoskelet. De twee belangrijkste componenten van het cytoskelet zijn actinefilamenten en microtubuli. Deze polymeren reorganiseren zich voortdurend om hun veelzijdige functies in de cel uit te kunnen voeren. In processen zoals celmigratie, groeien actinefilamenten tegen het celmembraan aan, en creëren daardoor platte uitsteeksels, die lamellipodia worden genoemd. De lamellipodia zorgen ervoor dat cellen over oppervlakken kunnen bewegen. Microtubuli spelen een sleutelrol in het celdelingsmechanisme. Tijdens dit proces wordt de scheiding van het genetisch materiaal tussen twee dochtercellen uitgevoerd door twee zogenaamde asters van microtubuli. De plaatsing van deze asters bepaalt vervolgens ook de locatie waar de dochtercellen van elkaar gescheiden worden door afsnoering. Hoewel zowel migratie als deling cruciale processen zijn voor de cel, zijn de mechanismen die ten grondslag liggen aan deze processen niet volledig bekend. De organisatie van het cytoskelet in cellen, en dus ook hun functie als "vormgevers" van de cel, is een samenspel tussen hun onderlinge interacties, de ruimtelijke opsluiting die ze ondervinden en wisselwerkingen met andere eiwitten. Omdat cellen enorm complexe systemen, blijkt een zogenaamde "bottom-up" experimentele werkwijze zeer nuttig te zijn om de specifieke inbreng van elk van deze wisselwerkingen op de organisatie van het cytoskelet te ontleden. Deze aanpak is gebaseerd op het reconstrueren van een minimaal systeem, om vervolgens stapsgewijs steeds meer complexiteit toe te voegen, zodat gaandeweg ons begrip van het systeem toeneemt.

In dit proefschrift starten we ook met een van bottom-up werkwijze, en bestuderen de verschillende aspecten van ruimtelijke opsluiting en wisselwerkingen op de organisatie van het cytoskelet. We gaan er van uit dat we de competitie tussen deze interacties al in het meest simpele systeem,

bestaande uit stijve cytoskeletpolymeren samengepakt in een beperkte ruimte, kunnen bestuderen . Empirisch wordt deze vraag geadresseerd door polymeren in virtuele microkamers op te sluiten, die klein zijn vergeleken met de persistentielengte van de opgesloten polymeren. In hoofdstuk 2 onderzoeken we door middel van Monte Carlo simulaties de organisatie van rigide polymeren die opgesloten zijn in ondiepe, vierkante containers, een geometrie die te zien is als een versimpeld model van een lamellipodium. We ontdekten dat wanneer het opsluitingseffect, dat uitlijning van de polymeren aan de muur veroorzaakt, in competitie is met de neiging van de polymeren om zich parallel aan elkaar te organiseren, er nieuwe ruimtelijke patronen ontstaan. De ruimtelijke organisatie wordt gekarakteriseerd door een nematische druppel, gericht langs een van de diagonalen van het vierkant terwijl verder de polymeren opgelijnd zijn aan de wanden. Om dit patroon te stabiliseren vormen zich lineaire defectstructuren.

In hoofdstuk 3 bestuderen we met dezelfde methoden rigide polymeren in een container met gekromde wanden, en zien dat de bipolaire structuur, die verschijnt in een schijfgeometrie, drastisch verandert door het openen van een gat in het midden van de container. In deze ringvormige geometrie, is de organisatie onverwachts gekarakteriseerd door sterk uitgelijnde domeinen, die van elkaar gescheiden worden door radiële defectmuren. De zo geobserveerde patronen zijn het directe resultaat van de eindige grootte van de deeltjes.

Wanneer de inflexibele polymeren klein zijn in vergelijking met de afmetingen van het volume waarin ze zijn opgesloten, verwachten we dat hun voorkeursorintatie slechts varieert over lengteschalen die veel groter zijn dan de lengte van het polymeer. In dit regime wordt het systeem goed beschreven door bestaande continuümtheorieën. Aangezien de continuümmodellen die tegenwoordig worden gebruikt, ofwel het ontstaan van singulariteiten uitsluiten door de manier waarop ze zijn geconstrueerd (bijv. het Oseen-Frank model), ofwel alleen een sterk gelimiteerde gebied van dichtheden bestrijken rond de overgang van een ongeordend naar een geordend systeem (het Landau-de Gennes model), construeren wij in hoofdstuk 4 een gemiddeld-veld model, dat de voordelen van deze twee type modellen combineert. We passen dit model toe op een systeem van rigide, kleine polymeren die opgesloten zijn in een rechthoekige, ondiepe container (de geometrie is vergelijkbaar met de geometrie beschreven in hoofdstuk 2), en we vinden dat de patronen, die de vrije energie van het systeem mini-

maliseren, gekarakteriseerd worden door een continue verandering van de orintatie. Evenwel levert ons model ook patronen op met puntdefecten die een lichtelijk hogere energie hebben.

Tot nu toe hebben we alleen stijve polymeren van het cytoskelet in beschouwing genomen. Echter, op de lengteschaal van de cel, kunnen de polymeren beter worden beschreven door als vervormbare elastische staven. In hoofdstuk 5 bestuderen we configuraties die worden aangenomen door de nu buigbare cytoskeletspolymeren, wanneer deze worden opgesloten in een onbuigzaam, ellipsoidaal membraan. We zien dat, in vergelijking met de cirkelvormige opsluiting, de verandering in de vorm van het membraan leidt tot een niet triviale organisatie van de opgesloten polymeren. De geobserveerde patronen bestaan uit enkele bundels, planaire asters, cirkelvormige en ellipsvormige ringen. In gereconstrueerde systemen, zoals emulsiedruppels, duwen de polymeren van het cytoskelet tegen het membraan, en vervormen het, maar aangezien het membraan onder spanning staat, dwingt het ook op zijn beurt de polymeren tot buigen. Het vaststellen van de polymeerconfiguraties als een functie van de vorm van het opsluitende oppervlak, is een eerste stap tot het begrijpen van de mechanische wisselwerking tussen het cytoskelet en het membraan.

Om een juiste celdeling te bewerkstelligen, is een precieze plaatsing van de twee betrokken microtubulusasters nodig. De precieze plaatsing van de twee asters is het resultaat van zowel duw- als trekkrachten die geproduceerd worden door de microtubulus-membraanwisselwerking. Empirisch bewijs laat zien dat in gereconstrueerde systemen er altijd een ruimtelijke scheiding optreedt tussen de twee asters. Daarom bestuderen we in hoofdstuk 6 de sterische afstoting tussen twee asters, en laten zien dat deze inderdaad leidt to een eindige afstand tussen de asters, die mede bepaald wordt door de lengte en dichtheid van microtubuli in de asters.

De modellen die we hebben ontwikkeld in dit proefschrift zijn een beginpunt voor het begrijpen van de organisatie van het cytoskelet en haar rol in de cel. In het laatste hoofdstuk van dit proefschrift beschrijven we enkele deuren naar toekomstig onderzoek die dit huidige werk heeft geopend.

Acknowledgments

My PhD in AMOLF has been both a fascinating learning experience and a very pleasant time. Therefore, I would like to thank all who shared their knowledge with me and helped me grow up scientifically. I also want to thank the people that, even if they did not directly contribute to my work, made my life enjoyable.

First and foremost I would like to thank to my supervisor. Bela, I am grateful to you for giving me the chance to work in your group and giving me all the freedom to choose the projects that I wanted to pursue. Throughout my PhD you offered me constant support and advice, keeping the perfect balance between close supervision and letting me work independently. Our weekly work discussions have been truly inspiring: every time I would bring up a problem you would have the perfect suggestion to solve it or at least an idea where to start looking for an answer. I never left your office without a solution. Your guidance went beyond just solving scientific problems: you taught me how to write papers, how to present my work, how to guide students. You supported me in many other problems such as data loss or housing issues. I am extremely grateful for everything.

During my PhD I had the chance to collaborate with many experimentalists whom I would like to thank. Gijsje, I learned a lot from you and I am grateful for giving me the chance to model experiments in your group. Your help, ranging from extremely fast corrections of papers to career advice, is much appreciated. Jose, we have collaborated on many projects and your enthusiasm always fascinated me. Thank you for all the ideas and hard work you put into all our projects. Sophie, your beautiful results on the droplets made me embark on an adventure which spans the last two years of my PhD. I enjoy our collaboration and I have learned a lot from it. Thank you! Nuria, I am glad we work together and I thank you for all the long clean room hours you put into our project. Marileen, I am grateful for all the ideas and suggestions. Feng, I am happy that our confinement

meeting lead to a joint project. Besides the collaborations within AMOLF, the confined viruses project offered me the opportunity to work with people outside our institute which was a learning step for me. Thank you Pavilk, Dirk and Oliver!

Throughout my time in AMOLF, the members of the "Bela" group have offered me support and made our early coffee brakes and our lunches enjoyable. Eva, you have been the best office mate ever! You guided me through FOM courses, iTSP and AMOLF forms. Thank you for always cheering me up. Niels, your extensive knowledge about everything from goldfish to Dutch politics made coffee breaks brighter. Pieter, you were my first master student and the learning experience went both ways– thank you. I enjoyed working with you and I am happy you got such beautiful results. Valerie, thank you for choosing to work with me, your organization is amazing! I am also grateful for improving my Dutch summary. Debasish, Bandan, Takis, Leander, Arthur and Pier, it was fun working in the same group.

I want to thank the people in the "other" theory group as well. Pieter-Rein, thank you for the discussions and the suggestions during the Theory meetings. Ana, you were the first one to offer me help on Monte Carlo simulations and particle visualization and I am grateful to you for this. Niels, you always had good suggestions for my projects that went beyond the Theory meetings, thank you! Tomeck, I am much obliged for all the cluster support. Andrew, Wiet, Chris, Filipe, Joris, Martijn, and Laurens, thank you for all the useful comments you made on my projects.

My PhD experience expanded beyond AMOLF. The three months I spend in Columbia University were extraordinary from a scientific perspective and, furthermore, living in New York was great. Angelo, thank you for hosting me in your group. I have learned so much during my stay. Joseph, Steward, and Clarion you made my New York stay enjoyable. Thank you for all the help with my project.

Many people from AMOLF made my life easier and happier for which I am grateful. Milena, I want to thank you for all your moral support and advice. Without you I would have most likely never went to the US. Feng, you helped me with so many things! Maga and Sophie thank you for being my paranymphs. Jeanette, thank you for all the nice times and for translating my Dutch summary. I keep found memories of ice skating on the frozen canals (with Nuria and Jose), balcanic parties (organized by Tomeck

and Annegret), salsa dancing (with Sophie and Jeanette), game nights (with Martijn, Noreen, Joris, Adithya, Stephen), and many other events such as dinners, barbecues and Polder Friday evenings (Fatemeh, Katia, Marina, Agata, Nicola, Jacopo, Simone, Lutz, Sarah, George, Marjon, Pierre, Karin and many others). Thank you! My work would have been my harder without the technical support from the ICT department in AMOLF. Carl, Lars, Wiebe, and Jan thank you for your help. I also want to thank Markus van Dijk from SurfSARA for setting up the Cytopol Cloud project.

Katerina, I kindly thank you for welcoming me in your home and for the perspective you gave me on inter-cultural problems.

I want to thank my parents who have supported and encouraged me throughout my studies. With your example you inspired me to go for a career in science.

Matthias, thank you for the constant moral support and encouragement especially throughout the writing of this thesis. I look forward to take next step in our lives together.

List of publications

The work in this thesis is part of the following publications:

"Colloidal liquid crystals in rectangular confinement: theory and experiment", Alexander H. Lewis, Ioana Garlea, Jose Alvarado, Oliver J. Dammone, Peter D. Howell, Apala Majumdar, Bela M. Mulder, M. P. Lettinga, Gijsje H. Koenderink, and Dirk G. A. L. Aarts, *Soft Matter* ***10****, pp. 7865-7873, (2014).* (Chapter 4)

"Defect structures mediate the isotropic-nematic transition in strongly confined liquid crystals", Ioana C. Gârlea, and Bela M. Mulder, *Accepted in Soft Matter, DOI: 10.1039/C4SM02087A, (2015).* (Chapter 2)

"The Landau-de Gennes approach revisited: a minimal self-consistent microscopic theory for spatially inhomogeneous nematic liquid crystals ", Ioana C. Gârlea, and Bela M. Mulder, *Manuscript in preparation.* (Chapter 4)

"Strong confinement induces defect-mediated domain structures in colloidal liquid crystals", Ioana C. Gârlea, Pieter Mulder, Jose Alvarado, Oliver J. Dammone, Dirk G. A. L. Aarts, M. P. Lettinga, Gijsje H. Koenderink, and Bela M. Mulder, *Manuscript in preparation.* (Chapter 3)

"Reconstitution of mitotic spindle features in vitro", Sophie Roth, Ioana C. Gârlea, Bela M. Mulder, and Marileen Dogterom, *Manuscript in preparation.* (Chapter 6)

"Self organization of Microtubules in 3D emulsion droplets", Sophie Roth, Ioana C. Gârlea, Núria Taberner, Bela M. Mulder, and Marileen Dogterom, *Manuscript in preparation.* (Chapter 5)

"Organization of F-actin bundles in spherical confinement ", Ioana C. Gârlea*, Feng-Ching Tsai*, Gijsje H. Koenderink, and Bela M. Mulder, *Manuscript in preparation.* (Chapter 5)

* authors contributed equally

About the author

Ioana Gârlea was born on August 1, 1986 in Bucharest, Romania. She finished high school at "Saint Sava" National College in 2005. The same year she started a Bachelor in Mathematics at the Faculty of Mathematics and Computer Science at the University of Bucharest, and a Bachelor in Physics at the Faculty of Physics, also at the University of Bucharest. Following the graduation of both studies, in the summer of 2008, she did an internship at the Laboratory of Corpuscular Physics in Clermont-Ferrand, France. In September 2008 she begun a Master in Theoretical Physics at Utrecht University, graduating in August 2010 with a thesis on dynamics of charged particles in an electrolytic cell with an oil-water interface supervised by Prof. Dr. René van Roij. From September 2010 on she has been working in the FOM Institute AMOLF, Amsterdam in the group of Prof. Dr. Bela M. Mulder. She first worked on confined liquid crystals gradually moving to more biological relevant problem such as the organization of cytoskeletal polymers in confinement. In 2013, upon receiving a EMBO Short Term Fellowship, she spent three months in the group of Dr. Angelo Cacciuto in the Department of Chemistry at Columbia University, New York working on the mechanical interplay between membrane deformation and bending of the enclosed cytoskeletal polymers.

Education Statement of the Graduate School

Experimental Plant Sciences

The Graduate School EXPERIMENTAL PLANT SCIENCES

Issued to: Ioana Cristina Garlea
Date: 16 January 2015
Group: Theory of Biomolecular Matter, FOM Institute AMOLF, Amsterdam
University: Wageningen University & Research Centre

1) Start-up phase	*date*
► **First presentation of your project**	
Actin filaments, microtubules and their interaction- Review	Oct 28, 2010
► **Writing or rewriting a project proposal**	
The mechanical interplay between cytsokelatal filaments and the enclosing cell membrane as a driver for spatial organization of cells. EMBO Short term Fellowship for Columbia University. Awarded ASTF 397-2013	Sep 2013
► **Writing a review or book chapter**	
► **MSc courses**	
► **Laboratory use of isotopes**	
Subtotal Start-up Phase	*5.5 credits**

2) Scientific Exposure	*date*
► **EPS PhD Student Days**	
EPS PhD student day, University of Amsterdam	Nov 30, 2012
► **EPS Theme Symposia**	
► **NWO Lunteren days and other National Platforms**	
Annual Dutch meeting on Molecular and Cellular Biophysics, Veldhoven	Oct 04-05, 2010
Physics @ FOM, Veldhoven	Jan 18-19, 2011
10th Dutch Soft Matter Meeting, Utrecht	May 26, 2011
Annual Dutch meeting on Molecular and Cellular Biophysics, Veldhoven	Oct 03-04, 2011
11th Dutch Soft Matter Meeting, Eindhoven	Nov 07, 2011
12th Dutch Soft Matter Meeting, Amsterdam	Apr 27, 2012
Annual Dutch meeting on Molecular and Cellular Biophysics, Veldhoven	Oct 01-02, 2012
13th Dutch Soft Matter Meeting, Wageningen	Nov 08, 2012
Physics @ FOM, Veldhoven	Jan 22-23, 2013
Physics @ FOM, Veldhoven	Jan 21-22, 2014
► **Seminars (series), workshops and symposia**	
Prof. Dr. Anne Mie Emons Farewell Symposium	Apr 21, 2011
Prof. Dr. Henk Lekerkerke Farewell Symopsium	Jun 10, 2011
Workshop on Computational Molecular Biophysics, San Diego, CA	Jun 19-21, 2011
KNAW meeting on Biophysics	Nov 30, 2010
KNAW meeting on Biophysics	Feb 01, 2011
KNAW meeting on Biophysics	Mar 29, 2011
KNAW meeting on Biophysics	Sep 13, 2011
KNAW meeting on Biophysics	Nov 30, 2011
KNAW meeting on Biophysics	Jan 30, 2012
KNAW meeting on Biophysics	Mar 26, 2012
KNAW meeting on Biophysics	Nov 29, 2012
KNAW meeting on Biophysics	Jan 28, 2014
KNAW meeting on Biophysics	Mar 25, 2014
KNAW meeting on Biophysics	May 13, 2014
AMOLF Biomeeting (10/year)	2010-2014
AMOLF colloquium (20/year)	2010-2014
► **Seminar plus**	
► **International symposia and congresses**	
Circle Meeting, Saarbrucken, Germany	Apr 13-15, 2011
7th International Conference on Biological Physics, San Diego, CA	Jun 22-24, 2011

	Circle Meeting, Paris, France	Apr 13-15, 2012
	Circle Meeting, Heidelberg, Germany	Apr 03-05, 2013
	Circle Meeting, Dreseden, Germany	Apr 22-24, 2014
	Physics and Biological Sytems, Gif-sur-Yvette, France	Jun 24-27, 2014
►	**Presentations**	
	Poster: Circle Meeting, Saarbrucken, Germany	Apr 14, 2012
	Poster: ICBP, San Diego	Jun 23, 2012
	Oral: SPAT meeting, Amsterdam	Mar 11, 2011
	Poster: Annual Dutch meeting on Molecular and Cellular Biophysics, Veldhoven	Oct 04, 2011
	Poster: Winerschool, Ascona, Switzerland	Jan 18, 2012
	Oral: Circle Meeting, Paris, France	May 04, 2012
	Oral: SPAT meeting, Utrecht	May 29, 2012
	Oral: Klein Colloquium at AMOLF, Amsterdam	Jun 11, 2012
	Oral: VU-AMOLF Summerschool,'t Vlintenholt	Jun 23, 2012
	Poster: Annual Dutch meeting on Molecular and Cellular Biophysics, Veldhoven	Oct 01, 2012
	Oral: Circle Meeting, Heidelberg, Germany	Apr 04, 2013
	Oral: VU-AMOLF Summerschool, 't Vlintenholt	Jun 23, 2013
	Oral: SPAT meeting, Wageningen	May30, 2013
	Oral: VU-AMOLF-UvA biophysics meeting, Amsterdam	Dec 04, 2013
	Oral: Physics@FOM, Veldhoven	21 Jan 2014
	Oral: Klein Colloquium at AMOLF, Amsterdam	Feb 03, 2014
	Oral: Circle Meeting, Dreseden, Germany	Apr 24, 2014
	Poster: Physics and Biological Sytems, Gif-sur-Yvette, France	Jun 24-27, 2014
	Oral: Klein Colloquium at AMOLF, Amsterdam	Oct 27, 2014
►	**IAB interview**	
►	**Excursions**	
	Subtotal Scientific Exposure	*45.4 credits**

3) In-Depth Studies		*date*
►	**EPS courses or other PhD courses**	
	Winterschool on Biophysics, Ascona, Switzerland	Jan 15-20, 2012
	VU-AMOLF summerschool 2012, 't Vlintenholt, The Netherlands	Jun 22-24, 2012
	Master Class at Physics@FOM 2013, Veldhoven	Jan 21, 2013
	VU-AMOLF summerschool 2013, 't Vlintenholt, The Netherlands	Jun 21-23, 2013
►	**Journal club**	
	Cytoskeleton Journal Club	2011-2014
►	**Individual research training**	
	Department of Chemistry, Columbia University, New York, US	Sep 01-Nov 30, 2013
	Subtotal In-Depth Studies	*9.6 credits**

4) Personal development		*date*
►	**Skill training courses**	
	Taking charge of your PhD Project (FOM)	May 31, Jun 14, 2010
	Dutch Level 1	Jan 24-Apr 18, 2011
	Dutch Level 2	May 09-Jul 11, 2011
	How to get funded (FOM)	Nov 14, 2014
	The art of presenting in science (FOM)	Mar 16, 30, Apr 30, 2012
	Write it right (FOM)	Apr 25-26, 2012
	FOM Valorisiation Workshop	Oct 16, 2012
	Business Orientaion week (Nyenrode)	Apr 06-11, 2014
	Dutch Level 3	Sep 12-Dec 14, 2011
	Career planning (FOM)	May 14, 31, June 06, 14, 26 2013
►	**Organisation of PhD students day, course or conference**	
►	**Membership of Board, Committee or PhD council**	
	Personeelsvereniging of AMOLF	Oct 2010-Oct 2012
	Subtotal Personal Development	*12.8 credits**

TOTAL NUMBER OF CREDIT POINTS*	**73.3**
Herewith the Graduate School declares that the PhD candidate has complied with the educational requirements set by the Educational Committee of EPS which comprises	
** A credit represents a normative study load of 28 hours of study.*	

The work described in this thesis was performed at the FOM Institute AMOLF, Science Park 104, 1098 XG Amsterdam, The Netherlands.

This work is part of the research programme of the Foundation for Fundamental Research on Matter (FOM), which is financially supported by the Netherlands Organisation for Scientific Research (NWO).

The work in Chapter 5 of this thesis was partially conducted in the Department of Chemistry in Columbia University, New York, US. The 90 days stay there was financed by EMBO short term fellowship ASTF 397 – 2013.

Part of the work in Chapter 5 was carried out on the Dutch national e-infrastructure with the support of SURF Foundation.

Financial support from Wageningen University for printing this thesis is gratefully acknowledged.